MAX-PLANCK-GESELLSCHAFT

Max Planck Graduate Center
mit der Johannes Gutenberg-Universität

JG|U
JOHANNES GUTENBERG
UNIVERSITÄT MAINZ

Climate and environmental reconstruction of the last 16,000 years in central-eastern Brazil using a speleothem multi-proxy approach

Dissertation

for attaining the academic degree of
„Doctor rerum naturalium“ (Dr. rer. nat.)

of the Departments
08 – Physics, Mathematics, and Computer Science,
09 – Chemistry, Pharmaceutics and Geosciences,
10 – Biology, and University Medicine
of the Johannes Gutenberg University Mainz

by

Marcela Eduarda Della Libera de Godoy

born 24.05.1994
in São Paulo

Johannes Gutenberg University Mainz with the Max Planck Graduate Center
prepared at the Institute of Geosciences
Mainz, October 2025

Faculty director: Prof. Dr. Eva Rentschler

1st supervisor: Prof. Dr. Denis Scholz
2nd supervisor: Dr. Hubert Vonhof

Date of oral examination: 19.12.2025

Sworn declaration

I hereby declare that I wrote the dissertation submitted without any unauthorized external assistance and used only sources acknowledged in the work. All textual passages which are appropriated verbatim or paraphrased from published and unpublished texts as well as all information obtained from oral sources are duly indicated and listed in accordance with bibliographical rules. In carrying out this research, I complied with the rules of standard scientific practice as formulated in the statutes of Johannes Gutenberg University Mainz to insure standard scientific practice.

………………………

Marcela Eduarda Della Libera de Godoy

Mainz, October 2025

Zusammenfassung

Paläoklimatische Archive wie Speläotheme liefern wichtige Erkenntnisse über vergangene Klimaschwankungen. Speläotheme sind als kontinentales Archiv besonders wertvoll, da sie weltweit vorkommen, mittels der ^{230}Th-U-Datierungsmethode präzise datiert werden können und durch die Ausfällung von Kalziumkarbonat aus sickerndem Tropfwasser in Höhlen entstehen, wobei sie Signale aus Boden, Grundgestein und Niederschlag integrieren. Im Allgemeinen sind die Isotopenverhältnisse von Sauerstoff (δ^{18}O) und Kohlenstoff (δ^{13}C) die am häufigsten verwendeten Proxies in Studien auf Basis von Speläothemen und dienen als Indikatoren für vergangene hydroklimatische und ökologische Veränderungen. In jüngerer Zeit haben Studien mit Multi-Proxy-Ansatz zugenommen, da sie ein umfassenderes Verständnis der komplexen Prozesse ermöglichen, die die Speläothemenbildung und die Interpretation von Klimasignalen beeinflussen.

In Südamerika haben Speläothemenstudien unser Verständnis des südamerikanischen Sommermonsuns (SASM) erheblich verbessert, dem dominierenden Klimasystem des Kontinents, das Niederschläge über dem tropischen Südamerika verursacht. Der SASM hat ein NW-SE-Konvektionsband, das sich über den Kontinent erstreckt, die Südatlantische Konvergenzzone (SACZ). Diese Arbeit wendet einen Multi-Proxy-Ansatz an, um die hydrologische, ökologische und temperaturbezogene Entwicklung der letzten 16.000 Jahre im zentralöstlichen Brasilien anhand eines Stalagmiten aus der São Mateus-Höhle im Bundesstaat Goiás zu rekonstruieren. Die Höhle liegt in einer Übergangsklimazone zwischen feuchten tropischen und semiariden Regionen, wodurch sie sehr empfindlich auf Veränderungen im SASM und in der SACZ reagiert.

Die Ergebnisse zeigten, dass Zentralostbrasilien in hohem Maße sowohl von tropischen als auch von hochlatitudinalen Einflüssen geprägt ist, wie beispielsweise Veränderungen der Sonneneinstrahlung, der Dynamik zwischen Ozean und Atmosphäre sowie interhemisphärischen Temperaturgradienten in verschiedenen Zeiträumen. Während der Deglazialperiode kam es zu raschen Temperatur- und hydrologischen Veränderungen, die mit abrupten Klimaveränderungen in der nördlichen Hemisphäre einhergingen. Während des Holozäns lassen die früheren Perioden auf sich verändernde Klima- und Umweltbedingungen schließen, die wahrscheinlich auf die geringe Sonneneinstrahlung zurückzuführen sind. Das mittlere und späte Holozän weisen stabilere Bedingungen auf, die auf die zunehmende Sonneneinstrahlung reagieren, die in diesen Perioden der dominierende Einflussfaktor ist. Schließlich zeigen die Multi-Proxy-Ergebnisse ausgeprägte hydrologische, ökologische und Temperaturveränderungen während der Deglaziation und des Holozäns. Die Aufzeichnungen von São Mateus liefern neue Erkenntnisse darüber, wie sich SACZ und SASM in den letzten 16.000 Jahren entwickelt haben.

Abstract

Paleoclimate archives, such as speleothems, provide critical understanding of past climate variability. Speleothems are particularly valuable as a continental archive since they occur world-wide, can be precisely dated via the ^{230}Th-U dating method and form by the precipitation of calcium carbonate from percolating drip water within caves, integrating signals from soil, bedrock, and rainfall. In general, oxygen ($\delta^{18}O$) and carbon ($\delta^{13}C$) isotope ratios have been the most used proxies in speleothem-based studies, serving as indicators of past hydroclimate and environmental changes. More recently, multi-proxy approach studies have been growing, since they provide more comprehensive understanding of the complex processes that influence speleothem formation and climate signal interpretation.

In South America, speleothem studies have greatly advanced our understanding of the South American Summer Monsoon (SASM), the continent's dominant climate system that leads precipitation over tropical South America. The SASM has a NW-SE convection band that extends over the continent, the South Atlantic Convergence Zone (SACZ). This thesis applies a multi-proxy approach to reconstruct the hydrological, environmental and temperature evolution of the last 16,000 years from central-eastern Brazil based on a stalagmite collected in São Mateus Cave, Goiás State. The cave lies in a transitional climate zone between humid tropical and semi-arid regions, making it highly sensitive to changes in the SASM and SACZ.

The results revealed that central-east Brazil is largely influenced by both tropical and high-latitude forcings, such as changes in solar radiation, ocean–atmosphere dynamics, and interhemispheric temperature gradients in several time-scales. During the deglacial period, rapid temperature and hydrological changes occurred concomitant with abrupt climate shifts in the Northen Hemisphere. During the Holocene, the earlier period evidences shifting climate and environmental conditions, likely due to the low insolation. The middle and late Holocene present more stable conditions responding to the increasing insolation, which is the dominant forcing at these periods. Finally, the multi-proxy results show pronounced hydrological, environmental and temperature changes during the during the deglaciation and the Holocene. The São Mateus record provides new evidence of how SACZ and SASM developed over the last 16,000 years.

Table of Contents

List of Figures

Chapter 1 - Introduction

Chapter 2 – Theoretical Framework

Chapter 3 – Manuscript I

Chapter 3.10 – Supplementary Figures – Manuscript I

Chapter 4 – Manuscript II

Chapter 4.9 – Supplementary Figures – Manuscript II

Chapter 5 – Manuscript III

Chapter 5.8 – Supplementary Figures – Manuscript III

List of Tables

Chapter 3 – Manuscript I

Chapter 4 – Manuscript II

Glossary

AMOC	Atlantic meridional overturning circulation
BA	Bølling–Allerød
BC	Brazilian Current
EAO	Equatorial Atlantic Ocean
EH	Early Holcoene
GDGT	Glycerol dialkyl glycerol tetraether
HS1	Heinrich Stadial 1
ITCZ	Intertropical Convergence Zone
LH	Late Holocene
MH	Middle Holocene
NBC	North Brazilian Current
NH	Northen Hemisphere
PCP	Prior Calcite Precipitation
SST	Sea Surface Temeprature
SAO	South Atlantic Ocean
SACZ	South Atlantic Convergence Zone
SASM	South American Summer Monsoon
sSEC	southern South Equatorial Current
TEX86	Tetraether index of 86 carbon atoms
YD	Younger Dryas

Chapter 1 – Introduction

Climate change is a central issue in today's society, and understanding the mechanisms of climate systems is essential for predicting future scenarios. However, instrumental records are very limited in time and are hence not able to capture long-term climate oscillations and how they impact the environment and human societies. Therefore, paleoclimate archives play a crucial role in extending our knowledge beyond recent centuries. Investigating how these mechanisms operated in the recent geological past is crucial, since the same drivers may continue to shape the future climate. In this context, cave deposits known as speleothems have been well-established as reliable, long continental archives, mostly because of their potential to record several proxies of past environmental and climate changes and the occurrence of karst systems worldwide (Fairchild and Baker, 2011).

Speleothems are secondary carbonate deposits formed in caves by the precipitation of calcium carbonate from dripping water, which is a result of the interaction between the meteoric water with the soil and rock above the cave as it percolates and reaches the cave atmosphere (Fairchild and Baker, 2011). The stalagmites, in particular, have a great potential as paleoclimate archives, mostly because they form by the successive precipitation of calcite layers that drop from the cave ceiling, resulting in a simple stratigraphy of concave layers from older (bottom) to younger (top). Their layered structure along with the exceptionally precise ^{230}Th-U dating method reaching up to ca. 600,000 years in the past (Scholz and Hoffmann, 2008) allow the acquisition of a well-resolved chronology to build high-resolution paleoclimatic and paleoenvironmental records, what brings an advantage relative to other archives such as tree rings, lake sediments and ice-cores (Fairchild and Treble, 2009)).

Most studies using stalagmites work with a combination of oxygen (δ^{18}O) and carbon (δ^{13}C) isotope ratios, as they are the most common proxies used for paleoclimatic reconstructions. Yet, multi-proxy studies have been recently more explored, since the combination of different, independent proxies provide a more robust understanding of past hydroclimate and environmental features. For instance, other proxies that are used in these studies are trace elements mass fractions (e.g.,(Fairchild and Treble, 2009; Tremaine and Froelich, 2013) strontium isotope ratios (^{87}Sr/^{86}Sr - e.g. Weber *et al.*, 2018) fluid inclusions (e.g. (Van Breukelen *et al.*, 2008), and even organic biomarkers (e.g. (Baker *et al.*, 2019).

Even though several studies have been done about the South American climate using the traditional $\delta^{18}O$ and $\delta^{13}C$ proxies over the past two decades (e.g. (Wang *et al.*, 2007; Cruz *et al.*, 2009; Stríkis *et al.*, 2011; Novello *et al.*, 2016, 2018), relative fewer studies have used a multi-proxy approach (Cruz *et al.*, 2007; Bernal *et al.*, 2016; Wortham *et al.*, 2017; Novello *et al.*, 2019; Ward *et al.*, 2019; Utida *et al.*, 2020). In particular, there is a lack of multi-proxy studies that integrate geochemical, isotopic, and environmental indicators to differentiate between local versus regional climate signals in transitional zones such as central-eastern Brazil. This evidences the need for expanding multi-proxy research in South America to improve our understanding of the complex interactions between climate drivers and their influence on regional climate variability.

The main climate system in the South America is the South American Summer Monsoon (SASM), which plays a major role in controlling rainfall across large portions of the continent and several large demographic centers rely on its moisture supply (Marengo *et al.*, 2012; Vuille *et al.*, 2012; Carvalho and Silva Dias, 2020).The monsoon is established over the Amazon Basin, where a strong monsoonal convective activity takes place within a core region over the south-western portion of the basin (Marengo *et al.*, 2012; Vuille *et al.*, 2012; Carvalho and Dias, 2020). Along with the SASM, the South Atlantic Convergence Zone (SACZ) is a key monsoonal feature characterized by a precipitation elongated band extending from the monsoon region south-eastward across the continent to the subtropical Atlantic Ocean, providing significant amount of moisture for central and southeast Brazil(Liebmann and Marengo, 2001; Carvalho *et al.*,2004; Vuille *et al.*, 2012). Because the SASM and SACZ are sensitive to both tropical and extratropical forcings, speleothem records offer a good opportunity to reconstruct its past variability and to assess how it has responded to orbital, solar, and ocean–atmosphere interactions (Cruz *et al.*, 2009; Stríkis *et al.*, 2011; Ramirez *et al.*, 2023). Therefore, developing multi-proxy records is essential for refining the interpretation of speleothem records in terms of hydroclimate variability and for improving our understanding of how the SASM and SACZ systems have interacted over time.

This thesis applies a multi-proxy approach for the paleoclimatic and paleoenvironmental reconstruction of the last 16k years of a stalagmite collected in São Mateus cave located in central-east Brazil, northeast of Goiás state (Fig. 1). The studied cave system is located in a state park named Parque Estadual da Terra Ronca (PETER), within the limestone rocks of Bambuí Group (Dardenne, 1978). This region lies at the boundary between two climate systems, humid tropical and semi-arid, where variations in the position and intensity of the SACZ can lead to pronounced hydroclimatic contrasts. This region is located at the boundary between two climate systems, humid tropical and semi-arid, with changes in SACZ displacement controlling the long-term hydroclimate. The humid tropical region located at the west/south of São Mateus is directly under the SACZ influence, while the semi-arid region is under influence of northeastern Brazil climatic settings (Fig. 1). This contrast between these regions reflects a climatic dipole that extends into the past in multiple time-scales (Cruz *et al.*, 2009; Cheng *et al.*, 2013; Della Libera *et al.*, 2022). In this context, this study combines multiple proxies in order to reconstruct a comprehensive picture of past hydroclimate variability over this sensitive region, with important implications for future hydroclimatic scenarios under ongoing climate change.

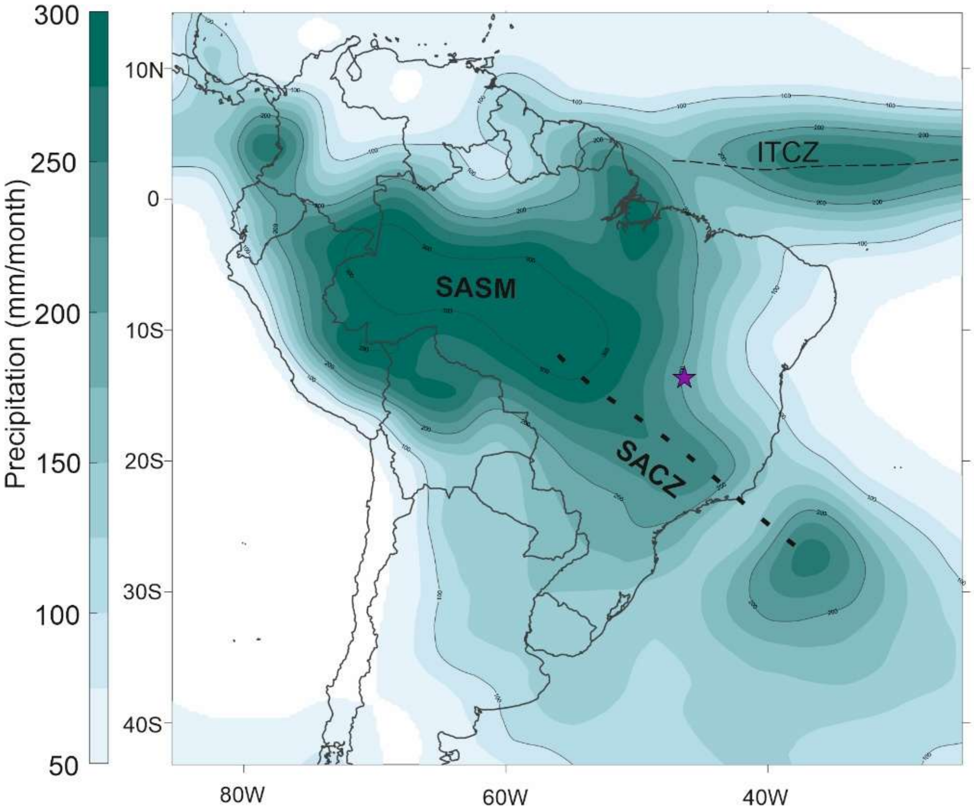

Figure 2 – Map of South America with austral summer precipitation during peak monsoon season (DJF) from Global Precipitation Measurement Mission (GPM, 2001-2020) (Huffman *et al.*, 2019). Main summer climate features over the continent indicated as SASM (South American Summer monsoon) and SACZ (South Atlantic Convergence Zone), with its mean location represented by the dashed line. The purple star represents São Mateus cave. The climatological DFJ location of ITCZ is represented by the dashed line.

1.1 References

Baker, A., Blyth, A.J., Jex, C.N., Mcdonald, J.A., Woltering, M., Khan, S.J., 2019. Glycerol dialkyl glycerol tetraethers (GDGT) distributions from soil to cave: Refining the speleothem paleothermometer. Organic Geochemistry 136. https://doi.org/10.1016/j.orggeochem.2019.06.011

Bernal, J.P., Cruz, F.W., Stríkis, N.M., Wang, X., Deininger, M., Catunda, M.C.A., Ortega-Obregón, C., Cheng, H., Edwards, R.L., Auler, A.S., 2016. High-resolution Holocene South American monsoon history recorded by a speleothem from Botuverá Cave, Brazil. Earth and Planetary Science Letters 450, 186–196. https://doi.org/10.1016/j.epsl.2016.06.008

Carvalho, L.M.V., Dias, M.A.F.S., 2020. Mesoscale and High-Impact Weather in the South American Monsoon. The Multiscale Global Monsoon System 151–160. https://doi.org/10.1142/9789811216602_0012

Carvalho, L.M.V., Jones, C., Liebmann, B., 2004. The South Atlantic convergence zone: Intensity, form, persistence, and relationships with intraseasonal to interannual activity and extreme rainfall. Journal of Climate 17, 88–108. https://doi.org/10.1175/1520-0442(2004)017%253C0088:TSACZI%253E2.0.CO;2

Cheng, H., Sinha, A., Cruz, F.W., Wang, X., Edwards, R.L., D'Horta, F.M., Ribas, C.C., Vuille, M., Stott, L.D., Auler, A.S., 2013. Climate change patterns in Amazonia and biodiversity. Nature Communications 4, 1411–1411. https://doi.org/10.1038/ncomms2415

Cruz, F.W., Burns, S.J., Jercinovic, M., Karmann, I., Sharp, W.D., Vuille, M., 2007. Evidence of rainfall variations in Southern Brazil from trace element ratios (Mg/Ca and Sr/Ca) in a Late Pleistocene stalagmite. Geochimica et Cosmochimica Acta 71, 2250–2263. https://doi.org/10.1016/j.gca.2007.02.005

Cruz, F.W., Vuille, M., Burns, S.J., Wang, X., Cheng, H., Werner, M., Lawrence Edwards, R., Karmann, I., Auler, A.S., Nguyen, H., 2009. Orbitally driven east-west antiphasing of South American precipitation. Nature Geoscience 2, 210–214. https://doi.org/10.1038/ngeo444

Della Libera, M.E., Novello, V.F., Cruz, F.W., Orrison, R., Vuille, M., Maezumi, S.Y., de Souza, J., Cauhy, J., Campos, J.L.P.S., Ampuero, A., Utida, G., Stríkis, N.M., Stumpf, C.F., Azevedo, V., Zhang, H., Edwards, R.L., Cheng, H., 2022. Paleoclimatic and paleoenvironmental changes in Amazonian lowlands over the last three millennia. Quaternary Science Reviews 279, 107383–107383. https://doi.org/10.1016/J.QUASCIREV.2022.107383

Fairchild, I.J., Baker, A., 2011. From Process to Past Environments, Speleothem Science.

Fairchild, I.J., Treble, P.C., 2009. Trace elements in speleothems as recorders of environmental change. Quaternary Science Reviews 28, 449–468. https://doi.org/10.1016/j.quascirev.2008.11.007

Liebmann, B., Jones, C., de Carvalho, L.M.V., 2001. Interannual variability of daily extreme precipitation events in the state of Saõ Paulo, Brazil. Journal of Climate 14, 208–218. https://doi.org/10.1175/1520-0442(2001)014%253C0208:IVODEP%253E2.0.CO;2

Marengo, J.A., Liebmann, B., Grimm, A.M., Misra, V., Silva Dias, P.L., Cavalcanti, I.F.A., Carvalho, L.M.V., Berbery, E.H., Ambrizzi, T., Vera, C.S., Saulo, A.C., Nogues-Paegle, J., Zipser, E., Seth, A., Alves, L.M., 2012. Recent developments on the South American monsoon system. International Journal of Climatology 32, 1–21. https://doi.org/10.1002/joc.2254

Novello, V.F., Cruz, F.W., McGlue, M.M., Wong, C.I., Ward, B.M., Vuille, M., Santos, R.A., Jaqueto, P., Pessenda, L.C.R., Atorre, T., Ribeiro, L.M.A.L., Karmann, I., Barreto, E.S., Cheng, H., Edwards, R.L., Paula, M.S., Scholz, D., 2019. Vegetation and environmental changes in tropical South America from the last glacial to the Holocene documented by multiple cave sediment proxies. Earth and Planetary Science Letters 524, 115717–115717. https://doi.org/10.1016/j.epsl.2019.115717

Novello, V.F., Cruz, F.W., Moquet, J.S., Vuille, M., de Paula, M.S., Nunes, D., Edwards, R.L., Cheng, H., Karmann, I., Utida, G., Stríkis, N.M., Campos, J.L.P.S., 2018. Two Millennia of South Atlantic Convergence Zone Variability Reconstructed From Isotopic Proxies. Geophysical Research Letters 45, 5045–5051. https://doi.org/10.1029/2017GL076838

Novello, V.F., Vuille, M., Cruz, F.W., Stríkis, N.M., De Paula, M.S., Edwards, R.L., Cheng, H., Karmann, I., Jaqueto, P.F., Trindade, R.I.F., Hartmann, G.A., Moquet, J.S., 2016. Centennial-scale solar forcing of the South American Monsoon System recorded in stalagmites. Scientific Reports 6, 1–8. https://doi.org/10.1038/srep24762

Ramirez, V.M., Cruz, F.W., Vuille, M., Novello, V.F., Stríkis, N.M., Cheng, H., Zhang, H.W., Bernal, J.P., Du, W.J., Ampuero, A., Deininger, M., Chiessi, C.M., Tejedor, E., Campos, J.L., Ait Brahim, Y., Edwards, R.L., 2023. Summer insolation controlled movements of Intertropical Convergence Zone during last glacial cycle in northern South America. Communications Earth and Environment 4. https://doi.org/10.1038/s43247-023-01124-6

Scholz, D., Hoffmann, D.L., 2011. StalAge - An algorithm designed for construction of speleothem age models. Quaternary Geochronology 6, 369–382. https://doi.org/10.1016/j.quageo.2011.02.002

Stríkis, N.M., Cruz, F.W., Cheng, H., Karmann, I., Edwards, R.L., Vuille, M., Wang, X., de Paula, M.S., Novello, V.F., Auler, A.S., 2011. Abrupt variations in South American monsoon rainfall during the Holocene based on a speleothem record from central-eastern Brazil. Geology 39, 1075–1078. https://doi.org/10.1130/G32098.1

Tremaine, D.M., Froelich, P.N., 2013. Speleothem trace element signatures: A hydrologic geochemical study of modern cave dripwaters and farmed calcite. Geochimica et Cosmochimica Acta. https://doi.org/10.1016/j.gca.2013.07.026

Utida, G., Cruz, F.W., Santos, R.V., Sawakuchi, A.O., Wang, H., Pessenda, L.C.R., Novello, V.F., Vuille, M., Strauss, A.M., Borella, A.C., Stríkis, N.M., Guedes, C.C.F., Dias De Andrade, F.R., Zhang, H., Cheng, H., Edwards, R.L., 2020. Climate changes in Northeastern Brazil from deglacial to Meghalayan periods and related environmental impacts. Quaternary Science Reviews 250. https://doi.org/10.1016/j.quascirev.2020.106655

van Breukelen, M.R., Vonhof, H.B., Hellstrom, J.C., Wester, W.C.G., Kroon, D., 2008. Fossil dripwater in stalagmites reveals Holocene temperature and rainfall variation in Amazonia. Earth and Planetary Science Letters 275, 54–60. https://doi.org/10.1016/j.epsl.2008.07.060

Vuille, M., Burns, S.J., Taylor, B.L., Cruz, F.W., Bird, B.W., Abbott, M.B., Kanner, L.C., Cheng, H., Novello, V.F., 2012. A review of the South American monsoon history as recorded in stable isotopic proxies over the past two millennia. Climate of the Past 8, 1309–1321. https://doi.org/10.5194/cp-8-1309-2012

Wang, X., Auler, A.S., Edwards, R.L., Cheng, H., Ito, E., Wang, Y., Kong, X., Solheid, M., 2007. Millennial-scale precipitation changes in southern Brazil over the past 90,000 years. Geophysical Research Letters 34. https://doi.org/10.1029/2007GL031149

Ward, B.M., Wong, C.I., Novello, V.F., McGee, D., Santos, R.V., Silva, L.C.R., Cruz, F.W., Wang, X., Edwards, R.L., Cheng, H., 2019. Reconstruction of Holocene coupling between the South America Monsoon System and local moisture variability from speleothem δ 18 O and 87 Sr/ 86 Sr records. Quaternary Science Reviews 210, 51–63. https://doi.org/10.1016/j.quascirev.2019.02.019

Weber, M., Lugli, F., Jochum, K.P., Cipriani, A., Scholz, D., 2018. Calcium Carbonate and Phosphate Reference Materials for Monitoring Bulk and Microanalytical Determination of Sr Isotopes. Geostandards and Geoanalytical Research 42, 77–89. https://doi.org/10.1111/ggr.12191

Wortham, B.E., Wong, C.I., Silva, L.C.R., McGee, D., Montañez, I.P., Troy Rasbury, E., Cooper, K.M., Sharp, W.D., Glessner, J.J.G., Santos, R.V., 2017. Assessing response of local moisture conditions in central Brazil to variability in regional monsoon intensity using speleothem 87Sr/86Sr values. Earth and Planetary Science Letters 463, 310–322. https://doi.org/10.1016/j.epsl.2017.01.034

Chapter 2 – Theoretical Framework

2.1 Speleothem formation

Speleothems are secondary calcium carbonate ($CaCO_3$) mineral deposits that form within caves of carbonate host rocks, such as limestones ($CaCO_3$) and dolomites ($CaMg(CO_3)_2$), and occur in various forms, such as stalagmites, stalactites and flowstones. Stalagmites, which build up from the cave floor towards the ceiling, are the most commonly studied speleothem and have been extensively used as a paleoclimate archive, mainly because of its potential to record environmental and climate proxies in a rather straightforward stratigraphy combined with the precise ^{230}Th-U dating method. Their formations are associated with a sequence of chemical processes that occur in the carbonate host rock, which act as aquifers, and transport the rainfall water into the cave system enabling the speleothem growth in this protected environment and allowing its growth for hundreds to thousands of years (Fairchild & Baker, 2012). Therefore, the geochemical composition of the speleothems will be controlled by multiple factors, including regional climatic conditions, processes within the overlying soil and vegetation, the hydrogeochemistry of the host rock, the dynamics of primary crystal growth during deposition, and subsequent secondary alterations after formation (Fairchild *et al.*, 2006).

Initially, the water from the ocean is evaporated and advected into the continent, where it might lead to cloud formations and eventually condensate into rainfall. The rainwater then percolates through the soil, where the partial pressure of CO_2 (P_{CO_2}) is higher relative to the water (unsaturated in CO_2) due to organic matter decomposition. This interaction leads to the dissolution of CO_2 and yields in the formation of carbonic acid (H_2CO_3). The carbonic acid is a weak acid, which will then gradually dissociate into other carbon chemical compounds at higher pH to bicarbonate (HCO_3^-) and carbonate (CO_3^{2-}), also known as dissolved inorganic carbon (DIC), according to the following chemical reactions (Fairchild and Baker, 2011):

$$\mathrm{H_2O + CO_2 \leftrightarrow H_2CO_3} \qquad \text{Eq. 1}$$

$$\mathrm{H_2CO_3 \leftrightarrow HCO_3{}^- + H^+} \qquad \text{Eq. 2}$$

$$\mathrm{HCO_3{}^- \leftrightarrow CO_3{}^{2-} + H^+} \qquad \text{Eq. 3}$$

The solution pH value will determine the proportions of DIC species, but at near-neutral pH values, the HCO_3^- is the dominant DIC (Fairchild & Baker, 2012). This solution then gradually becomes more acidic due to its interaction with CO_2 as it percolates through the soil, until it reaches the fissured and weathered limestone above the epikarst, and eventually the limestone bedrock. The resulting acid solution dissolves the carbonate rock according to the following reaction:

$$\mathrm{CaCO_3 + H_3O^+ \leftrightarrow Ca^{2+} + HCO_3^- + H_2O} \qquad \text{Eq. 4}$$

The final equilibrium reaction of the entire dissolution of the carbonate can be described as:

$$\mathrm{Ca^{2+} + 2HCO_3^- \rightarrow H_2O + CO_2 + CaCO_3} \qquad \text{Eq. 5}$$

Therefore, as the solution percolates through the limestone bedrock, it becomes saturated in Ca^{2+} as Eq.5 is constantly happening. When the seepage water reaches the cave atmosphere, it encounters an environment with usually at a much lower (P_{CO_2}) than the solution depending on the ventilation of the cave. This will induce the degassing process of CO_2 (Eq.5) from the solution to the cave atmosphere (Dreybrodt, 2008), potentially already forming a stalactite, since this reaction favors the precipitation of $CaCO_3$ by shifting the equilibrium toward the products, as shown in Eq.5. When the water then drips from the cave ceiling onto the top a stalagmite, it forms a thin layer of water and the excess CO_2 degasses from the solution, precipitating the carbonate forming the stalagmite (Fairchild *et al.*, 2006; Hansen, Dreybrodt and Scholz, 2013).

The degassing of CO_2 from the solution can occur during other stages of the water path, already precipitating carbonate prior to the solution's arrival in the cave, a process known as prior calcite precipitation (PCP). It can happen still within the bedrock before it reached the cave environment or a longer residence time of the water drop on the cave ceiling/stalactite will lead to precipitation (Dreybrodt, 2008a). Favorable conditions for PCP along the seepage water flowpath are usually associated with relative drier conditions due to reduced karstic recharge, the prolonged interaction time between the solution and the carbonate host rock and the higher chance of degassing into unfilled cavities along within the aquifer (Fairchild *et al.*, 2006). During this process, the Ca^{2+} is preferentially removed from the solution and precipitated along the flowpath, reducing its supersaturation in the remaining solution, while other trace elements remain relatively enriched compared to calcium, such as magnesium and strontium. Consequently, drip water affected by PCP often shows progressively higher trace-element ratios, e.g. Mg/Ca and Sr/Ca ratios, which become recorded in the speleothem (Fairchild *et al.*, 2006).

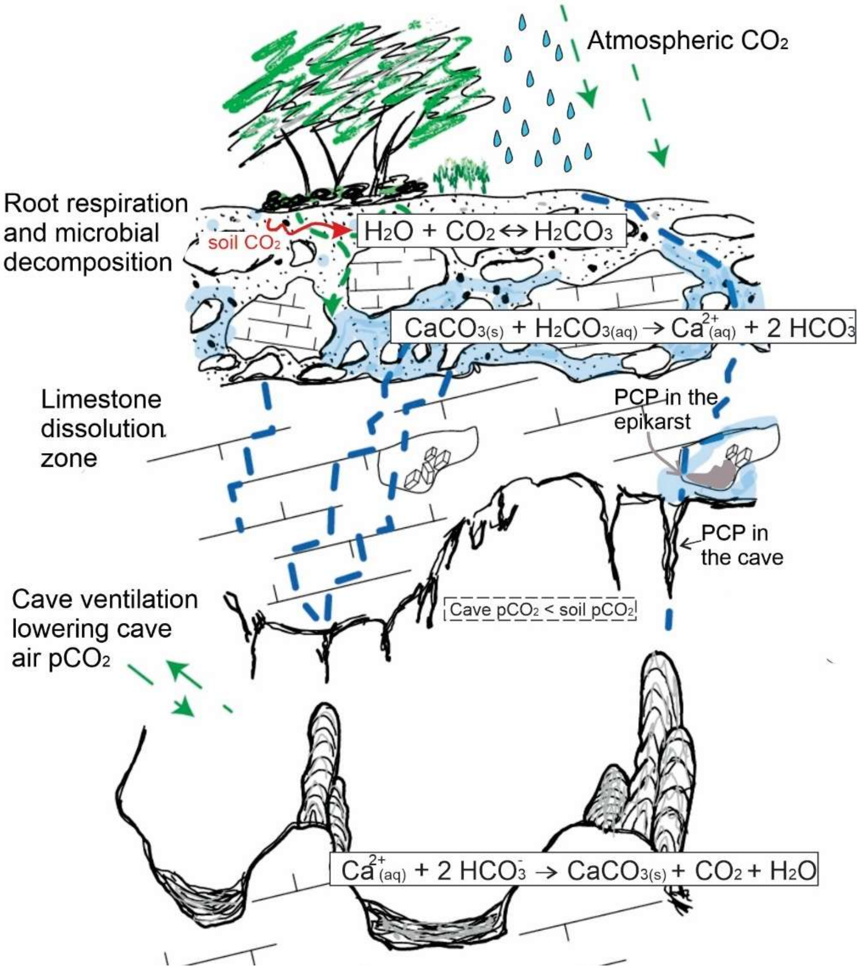

Figure 3.1 – Diagram illustrating dissolution and precipitation regimes in the karst system. Represents the interaction of the meteoric water with soil, capturing the CO_2 from decomposing organic matter and root respiration and forming the carbonic acid (Eq.1). As a consequence, the calcium carbonate (CaCO3) of the host rock is dissolved (Eq. 4) and Ca^{2+}(aq)are transported via drip water inside the cave system. Lastly, the precipitation of $CaCO_3$ inside the cave caused by degassing of CO_2 in the cave atmosphere. Modified from Patterson *et al.* (2024).

2.2 Speleothem ^{230}Th-U dating method

The U-series method for dating both marine (corals) and terrestrial (speleothems) carbonates is a well-known technique that allows for high-precision dating up to 600.000 years, providing robust chronologies crucial for paleoclimate reconstructions (Scholz & Hoffmann, 2008). This technique is based on the radioactive disequilibrium within the radionuclides decay chains ^{238}U, ^{235}U and ^{232}Th (Fig. 2.2), particularly the ^{238}U-^{234}U-^{230}Th decay chain. In natural materials (e.g. carbonate host-rocks), they are found in a secular equilibrium between parent and daughter nuclides in the ^{238}U and ^{235}U decay chains, established over the course of several millions of years, which have much longer half-lives compared to the intermediate daughter ones (Richards & Dorale, 2003). However, this equilibrium can be disturbed by geological or geochemical processes, such as during the dissolution and subsequent re-precipitation of secondary deposits (speleothems). This is key for the U-series dating to work, since the timing of the U-series re-equilibration in the secondary deposits can be quantified from decay constants of the radioactive isotopes (Richards & Dorale, 2003).

This principle works because U and Th present different geochemical behaviors in when in contact with water. Uranium mainly exists as uranyl ion $[UO_2]^{2+}$ in the continental crust and is highly soluble in water, strongly associated with organic matter acids (fulvic and humic), and easily incorporated into the calcite or aragonite lattice. In contrast, the thorium is highly insoluble and particle-reactive (e.g. detrital particles), making them much less mobile in comparison with the U. Therefore, at every speleothem layer that is formed, it contains in principle uranium but no thorium. This natural geochemical fractionation causes a disequilibrium between parent (^{238}U) and daughter (^{230}Th) isotopes that gradually reduces over time as ^{230}Th accumulates from uranium decay (Fig. 3). When equilibrium in reached, it is possible to measure the activity ratios of ^{230}Th and ^{238}U that allows the calculation of the speleothem deposition time (Bourdon *et al.*, 2003; Scholz & Hoffmann, 2008). In summary, the U-series dating method is based on three main assumptions for it to work: 1) the precipitate behaved as a closed system, i.e., no post-depositional addition or loss of the parent or daughter isotope (diagenesis); 2) absence of ^{230}Th nuclides at the time of formation, i.e., (^{230}Th/^{238}U) = 0; 3) absence of detrital ^{230}Th, ^{234}U and ^{238}U.

In general, the first assumption is frequently true for most speleothems given the very stable environment of a cave. Still, several studies have already pointed out samples that indicate open-system behaviors and have been affected by diagenesis (Scholz *et al.*, 2014; Bajo *et al.*, 2016). This occurs when the speleothem is in contact with corrosive drip water, which actively dissolves the speleothem, reshaping fabrics and redistributing U within the carbonate lattice, either adding or removing it (Scholz *et al.*, 2014). Since the uranyl ion $[UO_2]^{2+}$ is highly soluble in corrosive water, new U from the carbonate host-rock may be added into the speleothem lattice as it precipitates in the stalagmite's pores. On the other hand, when the corrosive water percolates through the stalagmite, it dissolves the calcite and carries along the U incorporated in the lattice, mobilizing it within the speleothem or leaching it out of the speleothem. In contrast with the U, the Th is practically insoluble, so it tends to be fixed in place. Therefore, post-depositional U loss increases (^{230}Th/^{238}U) activity ratios, leading to older ages than expected, while U gain produces artificially younger ages (Scholz *et al.*, 2014). The second assumption is usually verified by measuring the concentration of ^{232}Th. This isotope serves as a strong indicator of detrital ^{230}Th contamination, since the ^{232}Th can only be transported via particles and it has no radiogenic production in the U-Th decay chains. Therefore, if ^{232}Th is high, it indicates that a significant amount of initial ^{230}Th was also brought along and has to be corrected for. Yet, there is no universal (^{230}Th/^{232}Th) activity ratio for detrital material, but some methods are used for correction, for instance based on the assumption of a characteristic initial (^{230}Th/^{232}Th) activity ratio of the detrital component, to obtain reliable ages (Hans Wedepohl, 1995; Richards and Dorale, 2003; Scholz *et al.*, 2014). Finally, the third assumption is an overall condition for the U-series disequilibrium method that the decay chain has remained undisturbed since the time of deposition.

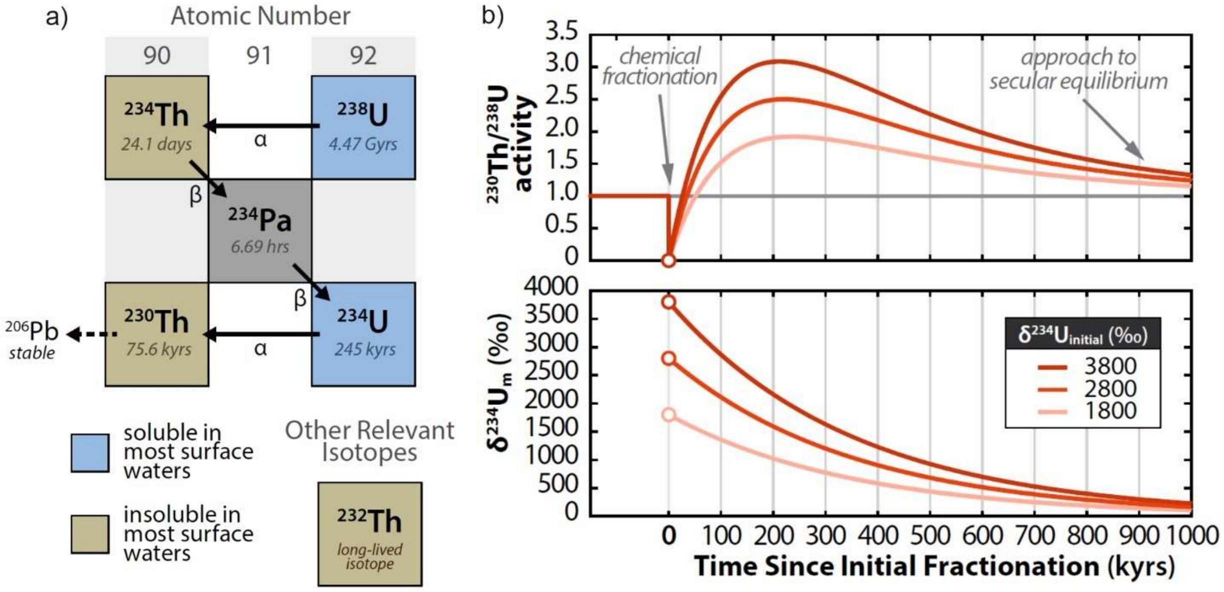

Figure 2.2 - The basic principles of U-Th dating. a) Schematic of the portion of the ^{238}U decay chain that is relevant for U-Th dating. The half-lives and type of particle emitted during radioactive decay (an α or β particle) of each isotope are shown. Ultimately, the decay chain ends with the stable ^{206}Pb. b) Isotope evolution diagrams showing the change in ^{230}Th/^{238}U activity and measured δ^{234}U ($\delta^{234}U_m$) — the two ratios used for the calculation of U-Th dates—after initial fractionation. The three thick red-shaded lines represent different pathways towards secular equilibrium based on the value of δ^{234}Uinitial. Modified after (Chen et al., 2020).

Considering these criteria are met, the time since the incorporation of U in the speleothem is directly related to the amount of daughter products. Therefore, the ^{230}Th-U age can be calculated by the activity ratios of (^{234}U/^{238}U) and (^{230}Th/^{238}U) according to the following equations:

$$\left(\frac{^{234}U}{^{238}U}\right)(t) = \left(\left(\frac{^{234}U}{^{238}U}\right)(t) - 1\right)e^{-\lambda_{234}t} + 1, \qquad \text{Eq. 5}$$

$$\left(\frac{^{230}Th}{^{238}U}\right)(t) = \left(1 - e^{-\lambda_{230}t}\right) + \left(\left(\frac{^{234}U}{^{238}U}\right)(t) - 1\right)\frac{\lambda_{230}}{\lambda_{230} - \lambda_{234}}\left(1 - e^{-(\lambda_{230} - \lambda_{230})t}\right), \qquad \text{Eq. 6}$$

where $\left(\frac{^{234}U}{^{238}U}\right)_{initial}$ is the initial (234U/238U) activity ratio, and λ_{234} and λ_{230} are the decay constants for ^{234}U and ^{230}Th.

The state-of-the-art analytical method for determining ^{230}Th-U ages is the multi-collector inductively coupled mass spectrometry (MC-ICP-MS). This method allows for a much higher analytical precision and smaller sample size compared to previous thermal ionization mass spectrometry (TIMS) method that was developed in the 1990s. The MC-ICP-MS analysis requires the chemical separation of the U and Th from each sub-sample collected from the speleothem, which are usually in the order of 0.15g. The purified solutions are nebulized and injected with an Ar carrier gas into the plasma, where the mixture is ionized. After ionization, the ion beam passes through a series of electric and magnetic fields and the ions are separated by their mass-to-charge ratios and parallel multiple collectors (i.e., multicollector) are used to measure the ions. As a result, the MC-ICP-MS technique allows for an ionization and transfer efficiency of ~1-2% (Scholz and Hoffmann, 2008; Cheng, Lawrence Edwards, *et al.*, 2013).

After obtaining a series of individual ages through the methods described above throughout the investigated speleothem sample, it is necessary to build and age-depth model to combine it with the high-resolution proxies and be able to discuss the time-related interpretations of the proxy time-series. Even though the ^{230}Th-U ages require a relatively small sample size to be measured and recent studies have been using a series of them throughout a speleothem, we still need to account for the age of the speleothem growth between the measured ^{230}Th-U ages. Some simple approaches to determine the age-depth relationships are linear regression or spline functions, for instance (Richards and Dorale, 2003). However, due to potential changes in the geochronological order of the ^{230}Th-U ages, i.e., age inversions, where dated layers do not follow the expected order of older ages with increasing distance from the top, it requires that a more accurate determination of which ages is responsible for this inversion need to be rejected. To account for that, several algorithms and models have been developed and are available in the literature to calculate the age-models (e.g., (Drysdale *et al.*, 2004; Ramsey, 2008; Scholz and Hoffmann, 2011; Breitenbach *et al.*, 2012).

Amongst them, the StalAge algorithm (Scholz and Hoffmann, 2011), the one used for the calculation of all age-depth models in this thesis, uses Monte Carlo simulations to fit straight lines through at least three data points. This method avoids the simple point-to-point interpolation by rejecting major outliers, adjusting uncertainties for minor ones, and ultimately preventing age inversions while producing more robust models (Scholz and Hoffmann, 2011).

2.3 Oxygen and Carbon Stable Isotopes

The two most common proxy records employed for paleoclimatic studies based on stalagmites are the oxygen ($\delta^{18}O$) and the carbon isotopes ($\delta^{13}C$). Both proxies reveal different aspects of the climatic and environmental conditions above the cave at the time of the speleothem formation. The $\delta^{18}O$ presents a relatively direct link to precipitation, since the oxygen incorporated into the carbonate comes from the rainwater infiltrating the cave, whereas $\delta^{13}C$ will be a result of the soil and vegetation above the cave, processes in the aquifer, as well as the input of biogenic CO_2 from organic matter decomposition. The sampling for these proxies is usually done in a MicroMill device, which allows a high-resolution sampling of the stalagmite, usually in the µm scale, and can yield a sub-annual resolution record depending on the stalagmite.

Even though the interpretation of $\delta^{18}O$ might seem straightforward, the speleothem $\delta^{18}O$ is the final product of a complex combination of interactions of the water during the hydrological cycle. The phase changes of water in the different stages of the hydrologic cycle are accompanied by oxygen isotope fractionation, a process where one isotope is favored over the other in the flux between reservoirs, thus favoring the isotope according to their mass, as the following equation (Clark and Fritz, 2013):

$$\alpha = {}^{\mathrm{Ra}}/_{\mathrm{Rb}} \qquad \text{Eq. 6}$$

$$\text{E. g.} \qquad \alpha^{18}\mathrm{O}_{(\mathrm{water-vapor})} = {}^{({}^{18}\mathrm{O}/{}^{16}\mathrm{O})_{\mathrm{water}}}/_{({}^{18}\mathrm{O}/{}^{16}\mathrm{O})_{\mathrm{vapor}}}$$

where α is the fractionation factor and R is the isotopic ratio of less/more abundant of the element.

However, to evaluate the relative variations between the isotope ratios, the notation δ is used as pointed out in Eq. 7, showing the relation between the isotope ratio of the sample and the isotope ratio of an international reference standard, establishing the isotopic ratio of the sample relative to that of the standard according to the equation (Lachniet, 2009):

$$\delta^{18}\mathrm{O}_{\mathrm{sample}} = \frac{\left(\frac{^{18}\mathrm{O}}{^{16}\mathrm{O}}\right)\mathrm{Sampl} \quad \left(\frac{^{18}\mathrm{O}}{^{16}\mathrm{O}}\right)\mathrm{Standard}}{\left(\frac{^{18}\mathrm{O}}{^{16}\mathrm{O}}\right)\mathrm{Starndard}} \times 1000 \qquad \text{Eq. 7}$$

The δ values are expressed as the difference in parts per thousand or permil (‰) from the reference value to facilitate the use of outcomes from this equation, which are rather small. For calcium carbonate, the standard value used as reference is the Vienna Peed Dee Belemnite (VPDB – (Craig, 1957), and in the case of water, the Vienna Standard Mean Ocean Water (VSMOW – Craig, 1961) is the internationally adopted standard. Both standards are established as 0‰ in a way that the variations in the ^{18}O/^{16}O ratio obtained in carbonate or water samples are always relative to differences from the standard. Hence, the δ^{18}O values from a sample are "enriched" with ^{18}O when the values are positive (higher ^{18}O/^{16}O sample ratio relative to the standard), or "depleted" of ^{18}O (lower ^{18}O/^{16}O sample ratio relative to the standard) (Lachniet, 2009).

Therefore, the climatic signal obtained from speleothem δ^{18}O will have a component that is related to the final outcome of these processes affecting the water along its pathway from the moisture source to rainfall above the cave. The water is initially evaporated from the ocean surface, i.e., the moisture source, which sets the initial δ^{18}O value depending on different factors such as salinity, evaporation and precipitation balance, sea ice melt, freshwater input, and large-scale oceanic and atmospheric circulation patterns (Fig. 2). The vapor is then advected over the continent, where it eventually condenses and falls as rainwater. The fractionation processes that occur in phase changes of water during this pathway will contribute to the δ^{18}O signature of the rainfall. In condensation processes, for example, the lighter water isotopologues ($H_2{}^{16}O$) preferentially remain in the vapor phase, while heavier ones ($H_2{}^{18}O$) are incorporated into de the liquid phase (rain). As a result, rainwater is typically enriched in ^{18}O (higher δ^{18}O) compared to the remaining cloud vapor (Lachniet, 2009; Clark & Fritz, 1997). The progressive condensation of the air mass along its pathway decreases the δ^{18}O value of the vapor and, consequently, of the rainfall, in a process known as Rayleigh distillation, which is also highly temperature dependent (Lachniet, 2009). This means that when the air mass migrates longitudinally from the ocean into the continent it will go through the continental effect, i.e., the further the moisture source, the stronger the Rayleigh effect and more depleted the $\delta^{18}O$ values get. Yet, when the air mass moves latitudinally, the temperature effect increases the Rayleigh distillation towards the poles, as the cooling of the air mass increases the $\delta^{18}O$ fractionation (Lachniet, 2009).

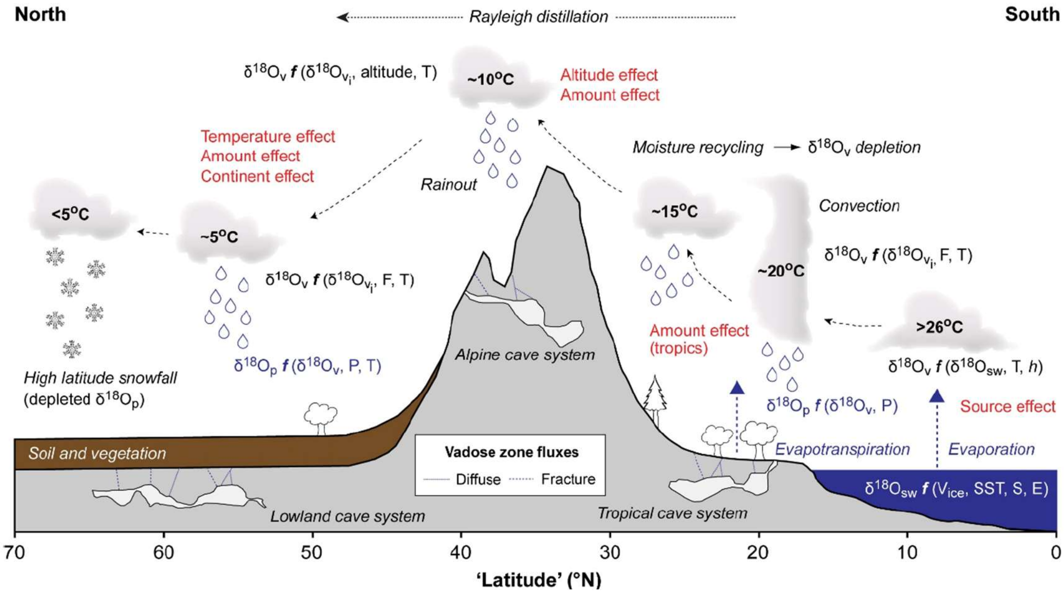

Figure 2.3 -Diagram illustrating the primary processes related to $\delta^{18}O$ variations relevant to speleothem paleo climatology. The dominant controls are based on variations in temperature and relative humidity, which influence the $\delta^{18}O$ values through the various processes and phase changes in the ocean, atmosphere, hydrosphere, soil and epikarst zones, and finally in speleothem CaCO3. In the figure, 'f' indicates it is a function of listed variables (illustration from Baker (2014) adapted from Lachniet (2009a)).

In summary, the final meteoric water $\delta^{18}O$ value that falls above the cave depends on several factors, such as distance from the moisture source, source effect, altitude, local temperature, and local and upstream amount of rainfall (Lachniet, 2009). Additionally, the water path from the soil to the cave and the cave environment also affect the final $\delta^{18}O$ signature that is imprinted in the precipitated speleothem. As the rainwater infiltrates the soil, into the epikarst and aquifer above the cave, additional processes can change its isotopic composition, such as evaporation both in the soil and in air-filled cavities in the aquifer, which enriches the water $\delta^{18}O$ value, mixing with older stored water, and varying flow paths through fissures and fractures (Long and Putnam, 2004; Lachniet, 2009). Therefore, the $\delta^{18}O$ value of drip water reaching the cave reflects the cumulative effects of soil, epikarst, and aquifer processes on top of the initial rainfall $\delta^{18}O$ signal, what can attenuate the variability of the drip water $\delta^{18}O$ in comparison with the rainfall $\delta^{18}O$ (Perrin, Jeannin and Zwahlen, 2003; Mattey *et al.*, 2008).

By reaching the cave, further enrichment of the drip water $\delta^{18}O$ value might occur due to evaporation in caves that are well-ventilated, have low relative humidity or due to long residence times on a stalactite or stalagmite tip (Lachniet, 2009). Finally, the conditions under which the carbonate precipitates, i.e., in equilibrium or kinetic fractionation, also leaves an imprint on the $\delta^{18}O$ of the speleothem. Under equilibrium conditions, a full isotopic exchange between the water, dissolved and precipitated carbonate is established, and the $\delta^{18}O$ of the precipitate reflects the drip water at the cave ambient temperature. In contrast, kinetic fractionation happens when rapid or incomplete reaction occur, such as in fast CO_2 degassing, evaporation, or low humidity that disrupt the equilibrium between phases, leading to isotopic values that are biased toward higher $\delta^{18}O$ (Hendy, 1971; Dreybrodt, 2008a; Dreybrodt and Scholz, 2010; Hansen *et al.*, 2019). As a result, the stalagmite $\delta^{18}O$ values record the outcome of the complex interaction between processes occurring in the atmosphere and the soil, karst, and cave environments. While this complexity can make climate interpretations challenging (e.g., (Scholz *et al.*, 2012; Weber, Scholz, *et al.*, 2018), (McDermott, 2004a; Fairchild *et al.*, 2006; Moseley *et al.*, 2014; Cheng *et al.*, 2016; Wassenburg *et al.*, 2016)when carefully considered these records provide valuable understandings into past hydroclimate variability, moisture sources, and atmospheric circulation patterns (McDermott, 2004b; Fairchild *et al.*, 2006; Moseley *et al.*, 2014; Cheng *et al.*, 2016; Wassenburg *et al.*, 2016).

Regarding the $\delta^{13}C$, the final values in a stalagmite are affected by additional processes that lead to the fractionation of the carbon stable isotopes, such as amount and type of vegetation above the cave according to their photosynthetic pathways (C3, C4 or CAM plants), soil P_{CO_2}, PCP, residence time of the water in the soil and carbon dissolution in an open/closed system (Mühlinghaus, Scholz and Mangini, 2009). Initially, the source of carbon that will mostly influence the speleothem isotopic value is the CO_2 from both plant root respiration and decomposition of organic matter by biological activity in the soil that is primarily incorporated into rainfall infiltration water, known as dissolved inorganic carbon (DIC) (Dreybrodt, 2008b; Novello *et al.*, 2021). Since different groups of plants (C3, C4 or CAM plants) use different processes to produce glucose after the hydration and dissociation of the captured atmospheric CO_2, this results in different $\delta^{13}C$ values in the soil CO_2. Hence, the type of dominant plants above the cave can imprint different isotopic signals to the speleothems $\delta^{13}C$ due to their distinct kinetic fractionation process during photosynthesis. Plants typically from savanna and grasslands, such as grass and shrubs (C4 photosynthetic pathway), present a $\delta^{13}C$ range between -15 to -10‰; woody type of plants, typical of dense forests (C3 photosynthetic pathway), show a $\delta^{13}C$ ranging from -30 to -24‰; CAM (crassulacean acid metabolism) plants, such as succulents and arid environments adapted plants, usually present $\delta^{13}C$ values that are similar to the C4-type, but can on occasion use the C3-type processes, thus overlaping the carbon isotopic signature of both C_4 and C_3 plants (Hendy, 1971; Dreybrodt, 2008b; Silva *et al.*, 2008; Pessenda *et al.*, 2010; Fohlmeister *et al.*, 2020; Novello *et al.*, 2021).

The interaction of the water with the soil CO_2 forms an acid solution that dissolves the cave host-rock, as in Eq. 1-4, with most soil DIC present as bicarbonate ion (HCO_3^-) (Mühlinghaus, Scholz and Mangini, 2009). The percolating solution typically dissolves the calcium carbonate under conditions that, in natural environments, are usually in an intermediate state between an open and closed system. In an open system, the solution is in equilibrium with the CO_2 reservoir from the soil, thus being the major contributor for the speleothem $\delta^{13}C$. On the other hand, in a closed system, the solution is isolated from the soil CO_2 reservoir and the carbon initially dissolved in the solution is consumed during the carbonate dissolution, leaving the isotopic imprint of the host-rock (McDermott, 2004b; Dreybrodt, 2008b; Fairchild and Baker, 2011). Additionally, PCP in the karst aquifer can strongly modify the $\delta^{13}C$ signal. The degree in which PCP occurs can vary due to the difference in P_{CO_2} between the solution and the air it is in contact with (aquifer fractures or cave), and to the residence time of the water exposed to the air. The time of residence of the solution in the aquifer can be influenced by hydrological availability. For instance, wetter conditions decrease the time of residence due to a higher recharge in the aquifer, lowering the time in which the solution is in contact with the air in the aquifer and even filling completely the pockets of air, which decreases the degassing and consequently decrease PCP rates. In contrast, drier conditions lead to high PCP rates (longer residence time and longer contact with the cave atmosphere) since the lighter CO_2 isotopologue (^{12}C) is removed, what is reflected in the stable isotope record from the stalagmite as an increase in $\delta^{13}C$ values.

In spite of the complexity of a climatic or environmental interpretation given the several processes involved in the modulation of speleothems $\delta^{13}C$ values, they remain highly informative, especially for detecting changes in vegetation density, composition, and activity above the cave (Cruz *et al.*, 2006; Novello *et al.*, 2019, 2021; Utida *et al.*, 2020). Furthermore, a multiproxy approach can also add valuable contribution to the interpretation of the $\delta^{13}C$ in speleothems. For instance, Utida *et al.* (2020) combined hydrological and vegetation proxies to demonstrate that variations in speleothem $\delta^{13}C$ were closely linked to shifts in vegetation cover, highlighting the importance of integrated datasets.

2.4 Strontium isotope in speleothems

The use of strontium isotopes ($^{87}Sr/^{86}Sr$) in speleothems as a proxy for paleoclimate reconstruction has been gaining notoriety in South America in the last few years (e.g. Wortham *et al.*, 2017; Ward *et al.*, 2029; Utida *et al.*, 2020). One of the early studies about the use of Sr isotopes in speleothems, (Banner *et al.*, 1996), already pointed out the potential of this proxy to improve the understanding between the climate variability and ground-water chemistry. In contrast with the oxygen and carbon isotopes, one of the greatest advantages of using $^{87}Sr/^{86}Sr$ is that it does not fractionate significantly during evaporation, degassing, temperature fluctuations and carbonate precipitation. Hence, the resulting $^{87}Sr/^{86}Sr$ ratio incorporated within speleothems primarily reflects the isotopic composition of the drip water from which they precipitate. Since the percolating water usually has a long interaction time with the host-rock, it is the major source of Sr in the speleothem. However, as initially presented by Banner *et al.* (1996) and further by other studies (e.g. (Goede *et al.*, 1998; Frumkin and Stein, 2004), different external inputs with considerable distinct $^{87}Sr/^{86}Sr$ ratios affect the drip water Sr signature. Long-range mineral aerosol dust (e.g., Saharan or Asian dust), sea spray salts, and volcanic ashes (Banner *et al.*, 1996), for instance, all present distinct Sr isotope signatures that interact with the infiltrating water when they are deposited on the soils above the cave. Consequently, the drip water $^{87}Sr/^{86}Sr$ ratios reflect the relative inputs from different sources that are isotopically distinct and interact with the drip water prior to its precipitation on the speleothem.

Additionally, Sr isotopes have been used as a proxy for rainfall and residence time in the aquifer (Weber *et al.,* 2018a; Wortham *et al.,* 2017: Ward *et al.*, 2019). Because the rainwater initially interacts with the soil before reaching the limestone, it initially acquires the soil $^{87}Sr/^{86}Sr$ signature. Hence, in areas where the soil and the limestone host-rock present very distinct $^{87}Sr/^{86}Sr$ signatures, the final speleothem Sr signature falls in a range between these two end-members. The soil often carries a significantly higher Sr isotopic signature compared to the limestone bedrock. Given the ^{87}Sr is the radiogenic daughter of ^{87}Rb, rocks and minerals with high Rb/Sr ratios (e.g., silicate rocks) will produce elevated $^{87}Sr/^{86}Sr$ ratios over geological time, and weathering of these minerals result in high radiogenic signature into the soil given the high amounts of ^{87}Sr. In contrast, the limestones usually present a much lower Sr isotopic signature. In the end, the $^{87}Sr/^{86}Sr$ ratio in speleothems often reflects the balance between soil-derived Sr (more radiogenic, high $^{87}Sr/^{86}Sr$) and bedrock-derived Sr (less radiogenic, lower $^{87}Sr/^{86}Sr$).

When rainwater infiltrates through the soil and epikarst, it dissolves Sr from soil minerals and organic-rich horizons before reaching the cave, leaving elevated $^{87}Sr/^{86}Sr$ ratios into the infiltrating water. However, as water infiltrates in the vadose zone above the cave, the $^{87}Sr/^{86}Sr$ signature of that water can evolve towards the bedrock signature via water-rock interaction depending on its residence time. This means that a longer residence time of the percolating water into the bedrock brings the water Sr isotope signal closer to the bedrock, while shorter interactions times preserve the original signal obtained from the soil. Given this scenario, several studies use Sr isotopes as a proxy for local hydrology, since drier conditions favor a longer residence time of the water in the limestone aquifer above the cave, which brings the drip water and, consequently, the speleothem $^{87}Sr/^{86}Sr$ closer to the bedrock values (lower). In contrast, in wetter periods, the water flows more rapidly between the soil and the cave environment, reducing the interaction time between the solution and the bedrock and having a stronger imprint of the soil $^{87}Sr/^{86}Sr$ ratios (higher) (Banner *et al.,* 1996; Wortham *et al.*, 2017).

Nonetheless, as previously mentioned, other studies also identified the influence of the other external sources of Sr in the speleothem, which also play an important role in understanding paleoclimate conditions. For instance, Goede *et al.* (1998), Frumkin and Stein (2004), and (Cruz *et al.*, 2021) all present evidence that their $^{87}Sr/^{86}Sr$ records show changes in input of aeolian dust deposits. Cruz *et al.* (2021) show how rapidly increasing dust fluxes in Northen Spain throughout the Late Holocene coincides with the desertification of large areas in northwestern Africa (Saharan desert) during this period, which is linked with to reduced Atlantic meridional overturning circulation (AMOC) strength and reduced summer monsoon. In contrast, lower $^{87}Sr/^{86}Sr$ ratios reflect decreased dust contribution due to wetter conditions in the Sahara, enhanced vegetation cover, and strengthened monsoon circulation, which shuts down dust mobilization (Cruz *et al.*, 2021). Another example is the contribution of sea-spray to the cave area. (Fisher *et al.*, 2010) used speleothem $^{87}Sr/^{86}Sr$ variations to determine when sea level was higher (shoreline closer), as sea-spray input would have been greater and tends to shift Sr isotopic values towards more “marine” signatures (higher $^{87}Sr/^{86}Sr$) and to lower influence of bedrock signatures, and the opposite scenario for lower sea levels (farther shoreline). This worked as an independent proxy, in combination with other tools, to reconstruct past shorelines in South Africa.

Overall, the using speleothem Sr isotope records can be a very strong tool for paleoclimate and paleoenvironmental reconstructions, but the main challenge in interpreting it is about understanding the potential Sr sources in a given area and estimate their respective contribution. On one hand, carbonate host-rock signatures can often be estimated based on their depositional ages (Burke *et al.*, 1982) and modern sea spray values are well constrained (McArthur *et al.*, 2012). On the other, external inputs such as dust are highly heterogeneous and their impact also depends on climatic factors such as rainfall and temperature, which influence the extent of weathering and mixing with bedrock-derived Sr (Capo, Stewart and Chadwick, 1998; Stewart, Capo and Chadwick, 1998). Consequently, reconstructing the isotopic composition and relative contribution of each potential source is essential for using Sr isotopes in speleothem-based paleoclimate studies.

2.4.1 Strontium isotope analysis

The most common method for obtaining $^{87}Sr/^{86}Sr$ ratios in speleothems is the solution-mode by the collection of bulk powder samples from the stalagmite throughout its growth axis and the further chemical separation of the Sr by a chromatographic column. The final solution is then analyzed by a MC-ICP-MS, as described in session 2.2, or by a TIMS system. Initially, Sr isotope analysis was restricted to TIMS, which requires long measurements times, but yield high precision analysis (Platzner, 1985). Yet, further developments in the MC-ICP-MS systems allowed for reduced analytical times with similar precision (Wieser and Schwieters, 2005). Therefore, depending on the facilitates available, both systems are still currently used for the Sr isotope analysis in speleothems (e.g., Utida *et al.,* 2020; Wortham *et al.,* 2017; Ward *et al.,* 2019).

Nonetheless, developments in the methodology allowed for the combination of the MC-ICP-MS system with a laser ablation system, bringing several advantages. For one, it eliminates the chemical separation step prior to analysis, reducing preparation time. Secondly, the spatial resolution increased significantly due to the laser precision instead of the bulk sample collection from the stalagmite. Also, the analytical time considerably reduced for less than five minutes per sample, with barely no changes in measurement precision. In contrast, given the low amounts of Sr content in most speleothems, the ablation of the speleothem by the LA-MC-ICP-MS analysis might not capture enough sample to an accurate analysis, limiting this analysis to some speleothems. Yet, several advances in mass spectrometry, laser ablation, and the development of suitable reference materials have lowered detection limits, enabling Sr isotope analysis in a wider range of samples (Wieser and Schwieters, 2005; Jochum *et al.*, 2014; Weber, Lugli, *et al.*, 2018). Still, to ensure reliable and robust $^{87}Sr/^{86}Sr$ ratios, the accuracy of the analysis can be secured through bracketing with appropriate reference materials during measurements(Irrgeher and Prohaska, 2016; Weber *et al.*, 2017; Weber, Lugli, *et al.*, 2018), as well as by monitoring the naturally constant $^{84}Sr/^{86}Sr$ ratio (Müller and Anczkiewicz, 2016). A more detailed description of the methods can be found in Weber *et al.* (2020) and Weber *et al.* (2017).

In spite of the advances in the LA-MC-ICP-MS analysis, only two studies use the combination of laser ablation and conventional solution mass spectrometry data (e.g., Weber *et al.*, 2017; Wortham *et al.,* 2017), even though the validation of the LA-MC-ICP-MS analysis has been verified by different studies and similar results were obtained with the solution-based analysis (e.g., (Vroon *et al.*, 2008; McArthur *et al.*, 2012). This thesis uses both methods, as observed in Chapter 3.

2.5 TEX86 – Organic Temperature Proxy

One of the central debates nowadays regarding climate change is the observed increasing temperatures since the 1950 and the further increase predicted by climate models (Forster *et al.,* 2025). Nonetheless, temperature is the least addressed variable in paleoclimate and paleoenvironmental reconstructions on continental records, such as in speleothems. Some techniques are used to recover temperature records from stalagmites, such as isotopic or noble gas analysis of fluid inclusions (Van Breukelen *et al.*, 2008; Scheidegger *et al.*, 2010; Meckler *et al.*, 2015), and clumped isotope thermometry of the calcite (Affek *et al.*, 2008; Kluge *et al.*, 2014). Both techniques, however, are subjected to the isotopic disequilibrium that occurs in speleothems (see section 2.3), which sometimes lead to temperature uncertainties and erroneously higher or lower temperatures(Kluge *et al.*, 2013; Meckler *et al.*, 2015; Hansen *et al.*, 2019; Meckler, Vonhof and Martínez-García, 2021). Therefore, the development of an organic temperature proxy offers a paleotemperature record independent from the isotopes. Studies focused on marine sediments (e.g. (Schouten *et al.*, 2002; Chiessi *et al.*, 2015a) have already largely explored the use of organic biomarkers, such as the glycerol dialkyl glycerol tetraether lipids (GDGTs), to reconstruct sea surface temperature (e.g. Schouten *et al.*, 2002; Bahr *et al.*, 2023). The GDGTs are membrane lipids derived from either archaea or bacterial groups that occur in two major categories: isoprenoid GDGTs (iGDGTs) derived from archaea, especially Crenarchaeota/Thaumarchaeota, which synthesize crenarchaeol and other GDGTs containing cyclopentane or cyclohexane rings, and branched GDGTs (brGDGTs) produced by certain soil bacteria that whose MBT (methylation index of branched tetraethers) and CBT (cyclisation ratio of branched tetraethers) indices vary systematically with terrestrial temperature and soil pH, respectively (Fig. 5 - Schouten *et al.*, 2002; Weijers *et al.*, 2007; Yang *et al.*, 2011, p. 20; Blyth and Schouten, 2013). The basic mechanism to why these membrane lipids work as a paleotemperature proxy is due to a physiological adaptation, where the microbes alter the number of cyclopentane rings in iGDGTs or the degree of methylation in brGDGTs in response to ambient temperature (Schouten *et al.*, 2002; Blyth & Schouten, 2013). Higher growth temperatures increase cyclopentane ring counts, raising membrane thermal stability, while warmer soils lower the methylation index of brGDGTs (Schouten *et al.*, 2002; Blyth & Schouten, 2013).

In speleothems, the archaeal iGDGTs prevail, whereas the brGDGTs are more common in the overlaying soil. Therefore, the use of an index that translates the GDGT distributions into temperature estimates is the TEX86 index, based on the relative abundance of iGDGTs with different ring numbers preserved in the speleothem, as in the following equation (Schouten *et al.,* 2002):

$$\mathrm{TEX}_{86} = \frac{(\mathrm{GDGT\ 2 + GDGT\ 3 + Cren\ isomer})}{(\mathrm{GDGT\ 1 + GDGT\ 2 + GDGT\ 3 - Cren\ isomer})} \qquad \text{Eq. 8}$$

Still, the brGDGTs are also analyzed in speleothems, as they provide complementary information to the archaeal-derived iGDGT signal and can help resolving source, contamination and calibration issues (Blyth & Schouten, 2013). Therefore, both MBT and CBT are calculated according to the equations (Weijers *et al.*, 2007):

$$\mathrm{MBT} = \frac{[\mathrm{I+Ib+Ic}]}{[\mathrm{I+Ib+}\quad] + [\mathrm{II+IIb+IIc}] + [\mathrm{III+IIIb+III}\quad]} \qquad \text{Eq. 9}$$

$$\mathrm{CBT} = \frac{[\mathrm{Ib}]+[\mathrm{IIb}]}{[\mathrm{I}]+[\mathrm{II}]} \qquad \text{Eq. 10}$$

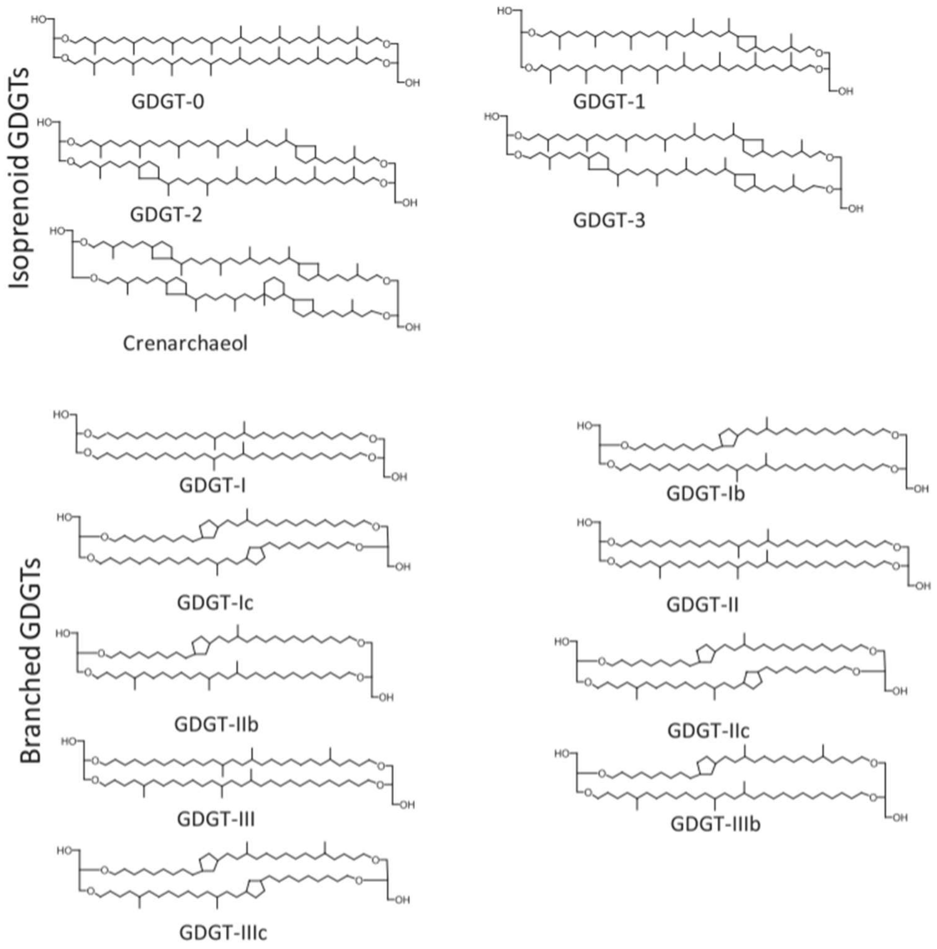

Figure 2.4 - Structures for the isoprenoid GDGTs (iGDGTs) and branched GDGTs (brGDGTs). Adapted from Baker *et al.* (2019).

For instance, to investigate whether the sample has soil contamination, the BIT (Branched and Isoprenoid Tetraether) index can be calculated to determine the dominance of iGDGT vs. brGDGT in the sample, thereby accessing whether the GDGT signal in a stalagmite is inherited from soil (higher BIT) input or produced in-situ (lower BIT) (Blyth & Schouten, 2013; Baker et al, 2019). In general, the BIT in speleothems is low, indicating a strong *in situ* cave/aquatic-derived rather than a soil-derived signal, supporting the idea that these organisms do not simply come from the soil into the cave, but are indeed distinct cave communities (Blyth & Schouten, 2013). The BIT index can be calculated according to the following equation (Hopmans *et al.*, 2004):

$$\mathrm{BIT} = \frac{(\mathrm{III}+\mathrm{II}+\mathrm{I})}{(\mathrm{Crenarchaeol}+\mathrm{III}+\mathrm{II}+\mathrm{I})} \qquad \text{Eq. 11}$$

Finally, the most recent cave air temperature estimates based on the TEX86 are calculated based on the proposed equation from Baker *et al.* (2019):

$$\text{Cave air T} = -7.34 + (34.64 \times \text{TEX}_{86}) \qquad \text{Eq. 12}$$

A calibration study developed by Blyth & Schouten (2013) demonstrates that the speleothem TEX86 proxy correlates strongly with surface mean annual temperature ($r^2 = 0.78$, ± 2.3 °C) and with cave mean temperature ($r^2 = 0.70$, ± 1.9 °C). Even though several studies have demonstrated that the TEX86 index can be used to reconstruct past cave temperatures, not many recent studies have applied this paleotemperature proxy in speleothem climate reconstructions (e.g. Huguet *et al.*, 2018; Wassenburg *et al.*, 2021; Levy *et al.*, 2023). Overall, TEX_{86} provides quantitative temperature estimates in both marine and cave archives with typical uncertainties of ±1–2 °C, but accurate interpretation requires site-specific calibration, assessment of source organisms, and consideration of environmental biases.

2.6 References

Affek, H.P., Bar-Matthews, M., Ayalon, A., Matthews, A., Eiler, J.M., 2008. Glacial/interglacial temperature variations in Soreq cave speleothems as recorded by 'clumped isotope' thermometry. Geochimica et Cosmochimica Acta 72, 5351–5360. https://doi.org/10.1016/j.gca.2008.06.031

Bahr, A., Jaeschke, A., Hou, A., Meier, K., Chiessi, C.M., Albuquerque, A.L.S., Rethemeyer, J., Friedrich, O., 2023. A Comparison Study of Mg/Ca-, Alkenone-, and TEX86-Derived Temperatures for the Brazilian Margin. Paleoceanography and Paleoclimatology 38. https://doi.org/10.1029/2023PA004618

Bajo, P., Hellstrom, J., Frisia, S., Drysdale, R., Black, J., Woodhead, J., Borsato, A., Zanchetta, G., Wallace, M.W., Regattieri, E., Haese, R., 2016. "Cryptic" diagenesis and its implications for speleothem geochronologies. Quaternary Science Reviews 148, 17–28. https://doi.org/10.1016/j.quascirev.2016.06.020

Baker, A., Blyth, A.J., Jex, C.N., Mcdonald, J.A., Woltering, M., Khan, S.J., 2019. Glycerol dialkyl glycerol tetraethers (GDGT) distributions from soil to cave: Refining the speleothem paleothermometer. Organic Geochemistry 136. https://doi.org/10.1016/j.orggeochem.2019.06.011

Banner, J.L., Musgrove, M., Asmerom, Y., Lawrence Edwards, R., Hoff, J.A., 1996. High-resolution temporal record of Holocene ground-water chemistry: Tracing links between climate and hydrology. https://doi.org/10.1130/0091-7613(1996)024%253C1049:HRTROH%253E2.3.CO;2

Blyth, A.J., Schouten, S., 2013. Calibrating the glycerol dialkyl glycerol tetraether temperature signal in speleothems. Geochimica et Cosmochimica Acta 109, 312–328. https://doi.org/10.1016/j.gca.2013.02.009

Breitenbach, S.F.M., Rehfeld, K., Goswami, B., Baldini, J.U.L., Ridley, H.E., Kennett, D.J., Prufer, K.M., Aquino, V.V., Asmerom, Y., Polyak, V.J., Cheng, H., Kurths, J., Marwan, N., 2012. COnstructing Proxy Records from Age models (COPRA). Climate of the Past 8, 1765–1779. https://doi.org/10.5194/cp-8-1765-2012

Burke, W.H., Denison, R.E., Hetherington, E.A., Koepnick, R.B., Nelson, H.F., Otto, J.B., 1982. Variation of seawater 87Sr/86Sr throughout Phanerozoic time. Geology 10, 516–519. https://doi.org/10.1130/0091-7613(1982)10%253C516:VOSSTP%253E2.0.CO;2

Capo, R.C., Stewart, B.W., Chadwick, O.A., 1998. Strontium isotopes as tracers of ecosystem processes: theory and methods. Geoderma 82, 197–225. https://doi.org/10.1016/S0016-7061(97)00102-X

Carvalho, L.M.V., Dias, M.A.F.S., 2020. Mesoscale and High-Impact Weather in the South American Monsoon. The Multiscale Global Monsoon System 151–160. https://doi.org/10.1142/9789811216602_0012

Chen, C.Y., McGee, D., Woods, A., Pérez, L., Hatfield, R.G., Edwards, R.L., Cheng, H., Valero-Garcés, B.L., Lehmann, S.B., Stoner, J.S., Schwalb, A., Tal, I., Seltzer, G.O., Tapia, P.M., Abbott, M.B., Rodbell, D.T., 2020. U-Th dating of lake sediments: Lessons from the 700 ka sediment record of Lake Junín, Peru. Quaternary Science Reviews 244, 106422. https://doi.org/10.1016/j.quascirev.2020.106422

Cheng, H., Spötl, C., Breitenbach, S.F.M., Sinha, A., Wassenburg, J.A., Jochum, K.P., Scholz, D., Li, X., Yi, L., Peng, Y., Lv, Y., Zhang, P., Votintseva, A., Loginov, V., Ning, Y., Kathayat, G., Edwards, R.L., 2016. Climate variations of Central Asia on orbital to millennial timescales. Sci Rep 6, 36975. https://doi.org/10.1038/srep36975

Clark, I.D., Fritz, P., 2013. Environmental Isotopes in Hydrogeology, 0 ed. CRC Press. https://doi.org/10.1201/9781482242911

Craig, H., 1957. Isotopic standards for carbon and oxygen and correction factors for mass-spectrometric analysis of carbon dioxide. Geochimica et Cosmochimica Acta 12, 133–149. https://doi.org/10.1016/0016-7037(57)90024-8

Cruz, J.A., Mcdermott, F., Turrero, M.J., Lawrence Edwards, R., Martín-Chivelet, J., 2021. Strong links between Saharan dust fluxes, monsoon strength, and North Atlantic climate during the last 5000 years, Sci. Adv.

Dardenne, M.A., 1978. Síntese sobre a estratigrafia do Grupo Bambuí no Brasil Central. Anais do XXX Congr. Bras. de Geol. Recife, 597–610.

Dreybrodt, W., n.d. Evolution of the isotopic composition of carbon and oxygen in a calcite precipitating H 2 O-CO 2-CaCO 3 solution and the related isotopic composition of calcite in stalagmites. Geochimica et Cosmochimica Acta 72, 4712–4724. https://doi.org/10.1016/j.gca.2008.07.022

Dreybrodt, W., Scholz, D., 2010. Climatic dependence of stable carbon and oxygen isotope signals recorded in speleothems: From soil water to speleothem calcite. https://doi.org/10.1016/j.gca.2010.11.002

Drysdale, R.N., Zanchetta, G., Hellstrom, J.C., Fallick, A.E., Zhao, J.X., Isola, I., Bruschi, G., 2004. Palaeoclimatic implications of the growth history and stable isotope (δ18O and δ13C) geochemistry of a Middle to Late Pleistocene stalagmite from central-western Italy. Earth and Planetary Science Letters 227, 215–229. https://doi.org/10.1016/j.epsl.2004.09.010

Fairchild, I.J., Baker, A., 2011. From Process to Past Environments, Speleothem Science.

Fairchild, I.J., Smith, C.L., Baker, A., Fuller, L., Spötl, C., Mattey, D., McDermott, F., 2006. Modification and preservation of environmental signals in speleothems. Earth-Science Reviews 75, 105–153. https://doi.org/10.1016/j.earscirev.2005.08.003

Fisher, E.C., Bar-Matthews, M., Jerardino, A., Marean, C.W., 2010. Middle and Late Pleistocene paleoscape modeling along the southern coast of South Africa. Quaternary Science Reviews 29, 1382–1398. https://doi.org/10.1016/j.quascirev.2010.01.015

Fohlmeister, J., Riavo G. Voarintsoa, N., Lechleitner, F.A., Boyd, M., Brandtstätter, S., Jacobson, M.J., Oster, J., 2020. Main Controls on the Stable Carbon Isotope Composition of Speleothems. Geochimica et Cosmochimica Acta. https://doi.org/10.1016/j.gca.2020.03.042

Forster, P.M., Smith, C., Walsh, T., Lamb, W.F., Lamboll, R., Cassou, C., Hauser, M., Hausfather, Z., Lee, J.-Y., Palmer, M.D., von Schuckmann, K., Slangen, A.B.A., Szopa, S., Trewin, B., Yun, J., Gillett, N.P., Jenkins, S., Matthews, H.D., Raghavan, K., Ribes, A., Rogelj, J., Rosen, D., Zhang, X., Allen, M., Aleluia Reis, L., Andrew, R.M., Betts, R.A., Borger, A., Broersma, J.A., Burgess, S.N., Cheng, L., Friedlingstein, P., Domingues, C.M., Gambarini, M., Gasser, T., Gütschow, J., Ishii, M., Kadow, C., Kennedy, J., Killick, R.E., Krummel, P.B., Liné, A., Monselesan, D.P., Morice, C., Mühle, J., Naik, V., Peters, G.P., Pirani, A., Pongratz, J., Minx, J.C., Rigby, M., Rohde, R., Savita, A., Seneviratne, S.I., Thorne, P., Wells, C., Western, L.M., van der Werf, G.R., Wijffels, S.E., Masson-Delmotte, V., Zhai, P., 2025. Indicators of Global Climate Change 2024: annual update of key indicators of the state of the climate system and human influence. Earth System Science Data 17, 2641–2680. https://doi.org/10.5194/essd-17-2641-2025

Frumkin, A., Stein, M., 2004. The Sahara-East Mediterranean dust and climate connection revealed by strontium and uranium isotopes in a Jerusalem speleothem. Earth and Planetary Science Letters 217, 451–464. https://doi.org/10.1016/S0012-821X(03)00589-2

Goede, A., Mcculloch, M., Mcdermott, F., Hawkesworth, C., 1998. Aeolian contribution to strontium and strontium isotope variations in a Tasmanian speleothem, Chemical Geology.

Hansen, M., Dreybrodt, W., Scholz, D., 2013. Chemical evolution of dissolved inorganic carbon species flowing in thin water films and its implications for (rapid) degassing of CO2 during speleothem growth. Geochimica et Cosmochimica Acta 107, 242–251. https://doi.org/10.1016/j.gca.2013.01.006

Hansen, M., Scholz, D., Schöne, B.R., Spötl, C., 2019. Simulating speleothem growth in the laboratory: Determination of the stable isotope fractionation (δ13C and δ18O) between H2O, DIC and CaCO3. Chemical Geology 509, 20–44. https://doi.org/10.1016/j.chemgeo.2018.12.012

Hendy, C.H., 1971. The isotopic geochemistry of speleothems—I. The calculation of the effects of different modes of formation on the isotopic composition of speleothems and their applicability as palaeoclimatic indicators. Geochimica et Cosmochimica Acta 35, 801–824. https://doi.org/10.1016/0016-7037(71)90127-X

Hopmans, E.C., Weijers, J.W.H., Schefuß, E., Herfort, L., Sinninghe Damsté, J.S., Schouten, S., 2004. A novel proxy for terrestrial organic matter in sediments based on branched and isoprenoid tetraether lipids. Earth and Planetary Science Letters 224, 107–116. https://doi.org/10.1016/j.epsl.2004.05.012

Huguet, C., Routh, J., Fietz, S., Lone, M.A., Kalpana, M.S., Ghosh, P., Mangini, A., Kumar, V., Rangarajan, R., 2018. Temperature and Monsoon Tango in a Tropical Stalagmite: Last Glacial-Interglacial Climate Dynamics. Scientific Reports 8. https://doi.org/10.1038/s41598-018-23606-w

Irrgeher, J., Prohaska, T., 2016. Application of non-traditional stable isotopes in analytical ecogeochemistry assessed by MC ICP-MS - A critical review. Anal Bioanal Chem 408, 369–385. https://doi.org/10.1007/s00216-015-9025-3

Jochum, K.P., Stoll, B., Weis, U., Jacob, D.E., Mertz-Kraus, R., Andreae, M.O., 2014. Non-Matrix-Matched Calibration for the Multi-Element Analysis of Geological and Environmental Samples Using 200 nm Femtosecond LA-ICP-MS: A Comparison with Nanosecond Lasers. Geostandards and Geoanalytical Research 38, 265–292. https://doi.org/10.1111/j.1751-908X.2014.12028.x

Kluge, T., Affek, H.P., Marx, T., Aeschbach-Hertig, W., Riechelmann, D.F.C., Scholz, D., Riechelmann, S., Immenhauser, A., Richter, D.K., Fohlmeister, J., Wackerbarth, A., Mangini, A., Spötl, C., 2013. Reconstruction of drip-water δ^{18}O based on calcite oxygen and clumped isotopes of speleothems from Bunker Cave (Germany). Climate of the Past 9, 377–391. https://doi.org/10.5194/cp-9-377-2013

Kluge, T., Affek, H.P., Zhang, Y.G., Dublyansky, Y., Spötl, C., Immenhauser, A., Richter, D.K., 2014. Clumped isotope thermometry of cryogenic cave carbonates. Geochimica et Cosmochimica Acta 126, 541–554. https://doi.org/10.1016/j.gca.2013.11.011

Lachniet, M.S., 2009. Climatic and environmental controls on speleothem oxygen-isotope values. Quaternary Science Reviews 28, 412–432. https://doi.org/10.1016/j.quascirev.2008.10.021

Liebmann, B., Jones, C., de Carvalho, L.M.V., 2001. Interannual variability of daily extreme precipitation events in the state of Saõ Paulo, Brazil. Journal of Climate 14, 208–218. https://doi.org/10.1175/1520-0442(2001)014%253C0208:IVODEP%253E2.0.CO;2

Long, A.J., Putnam, L.D., 2004. Linear model describing three components of flow in karst aquifers using 18O data. Journal of Hydrology 296, 254–270. https://doi.org/10.1016/j.jhydrol.2004.03.023

Marengo, J.A., Liebmann, B., Grimm, A.M., Misra, V., Silva Dias, P.L., Cavalcanti, I.F.A., Carvalho, L.M.V., Berbery, E.H., Ambrizzi, T., Vera, C.S., Saulo, A.C., Nogues-Paegle, J., Zipser, E., Seth, A., Alves, L.M., 2012. Recent developments on the South American monsoon system. International Journal of Climatology 32, 1–21. https://doi.org/10.1002/joc.2254

Mattey, D., Lowry, D., Duffet, J., Fisher, R., Hodge, E., Frisia, S., 2008. A 53 year seasonally resolved oxygen and carbon isotope record from a modern Gibraltar speleothem: Reconstructed drip water and relationship to local precipitation. Earth and Planetary Science Letters 269, 80–95. https://doi.org/10.1016/j.epsl.2008.01.051

McArthur, J.M., Sikdar, P.K., Hoque, M.A., Ghosal, U., 2012. Waste-water impacts on groundwater: Cl/Br ratios and implications for arsenic pollution of groundwater in the Bengal Basin and Red River Basin, Vietnam. Science of The Total Environment 437, 390–402. https://doi.org/10.1016/j.scitotenv.2012.07.068

McDermott, F., 2004. Palaeo-climate reconstruction from stable isotope variations in speleothems: A review. Quaternary Science Reviews 23, 901–918. https://doi.org/10.1016/j.quascirev.2003.06.021

Meckler, A.N., Affolter, S., Dublyansky, Y.V., Krüger, Y., Vogel, N., Bernasconi, S.M., Frenz, M., Kipfer, R., Leuenberger, M., Spötl, C., Carolin, S., Cobb, K.M., Moerman, J., Adkins, J.F., Fleitmann, D., 2015. Glacial–interglacial temperature change in the tropical West Pacific: A comparison of stalagmite-based paleo-thermometers. Quaternary Science Reviews 127, 90–116. https://doi.org/10.1016/j.quascirev.2015.06.015

Meckler, A.N., Vonhof, H., Martínez-García, A., 2021. Temperature reconstructions using speleothems. Elements 17, 101–106. https://doi.org/10.2138/GSELEMENTS.17.2.101

Moseley, G.E., Spötl, C., Svensson, A., Cheng, H., Brandstätter, S., Edwards, R.L., 2014. Multi-speleothem record reveals tightly coupled climate between central Europe and Greenland during Marine Isotope Stage 3. Geology 42, 1043–1046. https://doi.org/10.1130/G36063.1

Mühlinghaus, C., Scholz, D., Mangini, A., 2009. Modelling fractionation of stable isotopes in stalagmites. Geochimica et Cosmochimica Acta 73, 7275–7289. https://doi.org/10.1016/j.gca.2009.09.010

Müller, W., Anczkiewicz, R., 2016. Accuracy of laser-ablation (LA)-MC-ICPMS Sr isotope analysis of (bio)apatite – a problem reassessed. Journal of Analytical Atomic Spectrometry 31, 259–269. https://doi.org/10.1039/C5JA00311C

Novello, V.F., Vuille, M., Cruz, F.W., Stríkis, N.M., De Paula, M.S., Edwards, R.L., Cheng, H., Karmann, I., Jaqueto, P.F., Trindade, R.I.F., Hartmann, G.A., Moquet, J.S., 2016. Centennial-scale solar forcing of the South American Monsoon System recorded in stalagmites. Scientific Reports 6, 1–8. https://doi.org/10.1038/srep24762

Novello, V.F., William da Cruz, F., Vuille, M., Pereira Silveira Campos, J.L., Stríkis, N.M., Apaéstegui, J., Moquet, J.S., Azevedo, V., Ampuero, A., Utida, G., Wang, X., Paula-Santos, G.M., Jaqueto, P., Ruiz Pessenda, L.C., Breecker, D.O., Karmann, I., 2021. Investigating δ13C values in stalagmites from tropical South America for the last two millennia. Quaternary Science Reviews 255. https://doi.org/10.1016/j.quascirev.2021.106822

Perrin, J., Jeannin, P.-Y., Zwahlen, F., 2003. Epikarst storage in a karst aquifer: a conceptual model based on isotopic data, Milandre test site, Switzerland. Journal of Hydrology 279, 106–124. https://doi.org/10.1016/S0022-1694(03)00171-9

Pessenda, L.C.R., Gouveia, S.E.M., Ribeiro, A. de S., De Oliveira, P.E., Aravena, R., 2010. Late Pleistocene and Holocene vegetation changes in northeastern Brazil determined from carbon isotopes and charcoal records in soils. Palaeogeography, Palaeoclimatology, Palaeoecology 297, 597–608. https://doi.org/10.1016/j.palaeo.2010.09.008

Platzner, I., 1985. Multiple ion collection in thermal ionization isotope ratio mass spectrometry of strontium. International Journal of Mass Spectrometry and Ion Processes 67, 129–136. https://doi.org/10.1016/0168-1176(85)80012-4

Ramsey, C.B., 2008. Deposition models for chronological records. Quaternary Science Reviews, INTegration of Ice-core, Marine and Terrestrial records (INTIMATE): Refining the record of the Last Glacial-Interglacial Transition 27, 42–60. https://doi.org/10.1016/j.quascirev.2007.01.019

Richards, D.A., Dorale, J.A., 2003. Uranium-series chronology and environmental applications of speleothems. Uranium-series Geochemistry 52, 407–460. https://doi.org/10.2113/0520407

Scheidegger, Y., Baur, H., Brennwald, M.S., Fleitmann, D., Wieler, R., Kipfer, R., 2010. Accurate analysis of noble gas concentrations in small water samples and its application to fluid inclusions in stalagmites. Chemical Geology 272, 31–39. https://doi.org/10.1016/j.chemgeo.2010.01.010

Scholz, D., Frisia, S., Borsato, A., Spötl, C., Fohlmeister, J., Mudelsee, M., Miorandi, R., Mangini, A., 2012. Holocene climate variability in north-eastern Italy: Potential influence of the NAO and solar activity recorded by speleothem data. Climate of the Past 8, 1367–1383. https://doi.org/10.5194/cp-8-1367-2012

Scholz, D., Hoffmann, D., 2008. (230)Th/U-dating of fossil corals and speleothems.

Scholz, D., Hoffmann, D.L., 2011. StalAge - An algorithm designed for construction of speleothem age models. Quaternary Geochronology 6, 369–382. https://doi.org/10.1016/j.quageo.2011.02.002

Scholz, D., Tolzmann, J., Hoffmann, D.L., Jochum, K.P., Spötl, C., Riechelmann, D.F.C., 2014. Diagenesis of speleothems and its effect on the accuracy of 230Th/U-ages. Chemical Geology 387, 74–86. https://doi.org/10.1016/j.chemgeo.2014.08.005

Schouten, S., Hopmans, E.C., Schefuß, E., Sinninghe Damsté, J.S., 2002. Distributional variations in marine crenarchaeotal membrane lipids: a new tool for reconstructing ancient sea water temperatures? Earth and Planetary Science Letters 204, 265–274. https://doi.org/10.1016/S0012-821X(02)00979-2

Silva, L.C.R., Sternberg, L., Haridasan, M., Hoffmann, W.A., Miralles-Wilhelm, F., Franco, A.C., 2008. Expansion of gallery forests into central Brazilian savannas. Global Change Biology 14, 2108–2118. https://doi.org/10.1111/j.1365-2486.2008.01637.x

Stewart, B.W., Capo, R.C., Chadwick, O.A., 1998. Quantitative strontium isotope models for weathering, pedogenesis and biogeochemical cycling. Geoderma 82, 173–195. https://doi.org/10.1016/S0016-7061(97)00101-8

Strikis, N.M., Cruz, F.W., Cheng, H., Karmann, I., Edwards, R.L., Vuille, M., Wang, X., De Paula, M.S., Novello, V.F., Auler, A.S., 2011. Abrupt variations in South American monsoon rainfall during the Holocene based on a speleothem record from central-eastern Brazil. Geology 39, 1075–1078. https://doi.org/10.1130/G32098.1

Tremaine, D.M., Froelich, P.N., 2013. Speleothem trace element signatures: A hydrologic geochemical study of modern cave dripwaters and farmed calcite. Geochimica et Cosmochimica Acta. https://doi.org/10.1016/j.gca.2013.07.026

van Breukelen, M.R., Vonhof, H.B., Hellstrom, J.C., Wester, W.C.G., Kroon, D., 2008. Fossil dripwater in stalagmites reveals Holocene temperature and rainfall variation in Amazonia. Earth and Planetary Science Letters 275, 54–60. https://doi.org/10.1016/j.epsl.2008.07.060

Vroon, P.Z., Van Der Wagt, B., Koornneef, J.M., Davies, G.R., 2008. Problems in obtaining precise and accurate Sr isotope analysis from geological materials using laser ablation MC-ICPMS. Anal Bioanal Chem 390, 465–476. https://doi.org/10.1007/s00216-007-1742-9

Ward, B.M., Wong, C.I., Novello, V.F., McGee, D., Santos, R.V., Silva, L.C.R., Cruz, F.W., Wang, X., Edwards, R.L., Cheng, H., 2019. Reconstruction of Holocene coupling between the South America Monsoon System and local moisture variability from speleothem δ 18 O and 87 Sr/ 86 Sr records. Quaternary Science Reviews 210, 51–63. https://doi.org/10.1016/j.quascirev.2019.02.019

Wassenburg, J.A., Scholz, D., Jochum, K.P., Cheng, H., Oster, J., Immenhauser, A., Richter, D.K., Häger, T., Jamieson, R.A., Baldini, J.U.L., Hoffmann, D., Breitenbach, S.F.M., 2016. Determination of aragonite trace element distribution coefficients from speleothem calcite–aragonite transitions. Geochimica et Cosmochimica Acta 190, 347–367. https://doi.org/10.1016/j.gca.2016.06.036

Wassenburg, J.A., Vonhof, H.B., Cheng, H., Martínez-García, A., Ebner, P.R., Li, X., Zhang, H., Sha, L., Tian, Y., Edwards, R.L., Fiebig, J., Haug, G.H., 2021. Penultimate deglaciation Asian monsoon response to North Atlantic circulation collapse. Nature Geoscience 14, 937–941. https://doi.org/10.1038/s41561-021-00851-9

Weber, M., Lugli, F., Jochum, K.P., Cipriani, A., Scholz, D., 2018. Calcium Carbonate and Phosphate Reference Materials for Monitoring Bulk and Microanalytical Determination of Sr Isotopes. Geostandards and Geoanalytical Research 42, 77–89. https://doi.org/10.1111/ggr.12191

Weber, M., Wassenburg, J.A., Jochum, K.P., Breitenbach, S.F.M., Oster, J., Scholz, D., 2017. Sr-isotope analysis of speleothems by LA-MC-ICP-MS: High temporal resolution and fast data acquisition. Chemical Geology 468, 63–74. https://doi.org/10.1016/j.chemgeo.2017.08.012

Weijers, J.W.H., Schouten, S., van den Donker, J.C., Hopmans, E.C., Sinninghe Damsté, J.S., 2007. Environmental controls on bacterial tetraether membrane lipid distribution in soils. Geochimica et Cosmochimica Acta 71, 703–713. https://doi.org/10.1016/j.gca.2006.10.003

Wieser, M.E., Schwieters, J.B., 2005. The development of multiple collector mass spectrometry for isotope ratio measurements. International Journal of Mass Spectrometry, Isotope Ratio Measurements SI 242, 97–115. https://doi.org/10.1016/j.ijms.2004.11.029

Wortham, B.E., Wong, C.I., Silva, L.C.R., McGee, D., Montañez, I.P., Troy Rasbury, E., Cooper, K.M., Sharp, W.D., Glessner, J.J.G., Santos, R.V., 2017. Assessing response of local moisture conditions in central Brazil to variability in regional monsoon intensity using speleothem 87Sr/86Sr values. Earth and Planetary Science Letters 463, 310–322. https://doi.org/10.1016/j.epsl.2017.01.034

Yang, H., Ding, W., Zhang, C.L., Wu, X., Ma, X., He, G., Huang, J., Xie, S., 2011. Occurrence of tetraether lipids in stalagmites: Implications for sources and GDGT-based proxies. Organic Geochemistry 42, 108–115. https://doi.org/10.1016/j.orggeochem.2010.11.006

Zhou, J., Lau, K.M., 2001. Principal modes of interannual and decadal variability of summer rainfall over South America. International Journal of Climatology 21, 1623–1644. https://doi.org/10.1002/joc.700

Chapter 3 – Manuscript 1

Speleothem-based reconstruction of Holocene changes in monsoonal patterns and environmental conditions in central Brazil

Marcela Eduarda Della Libera[a,b]*; Julio Cauhy [a,b]: Cintia Stumpf [c]; Roberto V. Santos[c]; Francisco W. Cruz[d]; Nicolas M. Strikis[d]; Luciana F. Prado[e]; Jean-Sebastian Moquet[f]; Michael Weber[a]; Rebecca Orrison[g]; Hai Cheng[h] ; R. Lawrence Edwards[i] ; Valdir F. Novello[c]; Hubert Vonhof [b]; Denis Scholz[a]

[a] Institut für Geowissenschaften, Johannes-Gutenberg-Universität Mainz, Germany
[b] Max Planck Institut für Chemie, Mainz, Germany
[c] Institute of Geosciences, University of Brasília, Brasília – DF, Brazil
[d] Instituto de Geociências, Universidade de São Paulo, São Paulo-SP, Brazil
[e] Faculdade de Oceanografia, Universidade do Estado do Rio de Janeiro, Rio de Janeiro, Brazil
[f] CNRS/INSU, Institut des Sciences de la Terre d'Orléans, Orléans, France
[g] Department of Atmospheric and Environmental Sciences, University at Albany, Albany, United States of America
[h] Institute of Global Environmental Change, Xi'an Jiaotong University, Shaanxi, China
[i] University of Minnesota, Department of Earth and Environmental Sciences, Minnesota, United States of America

*Corresponding author:
Marcela E. Della Libera
Email: dellalibera.me@gmail.com

Paper accepted in Global and Planetary Changes

3.1 Abstract

The east-west precipitation dipole that occurs in South America has been vastly investigated in previous studies using paleoclimate records from east and west of the continent, but the climate dynamics of central-eastern Brazil remains less understood. While $\delta^{18}O$ values have been widely used to study past rainfall variability over South America, their ability to resolve local hydrological changes in central Brazil during the Holocene has been proven to be difficult. Recent studies in the region have used $\delta^{13}C$ values and $^{87}Sr/^{86}Sr$ ratios from speleothems to assess local paleo-hydrology and environmental conditions. Here, we revisit this topic for the last 11000 years based on a novel multi-proxy record ($\delta^{18}O$, $\delta^{13}C$, and $^{87}Sr/^{86}Sr$) from a stalagmite collected in central Brazil at the northern side of the present day South Atlantic Convergence Zone (SACZ). The overall climate shifted from drier to wetter conditions throughout the Holocene, reflecting the increasing southern insolation and the monsoon-driven wetting trend based on the local and regional $\delta^{13}C$ and pollen records. Changes in atmospheric circulation patterns during the Holocene might have been responsible for the increase in $\delta^{18}O$ values through time. A north-eastern climate influence during the weaker monsoon phase from early-to-mid Holocene contrasts the late Holocene and present-day influence of SACZ over the area. Hence, a negative correlation between $\delta^{18}O$ and $\delta^{13}C$ indicates a decoupling of monsoon activity from local climate conditions. The Sr isotope signals in our site may be influenced by mixed lithology or increased dust input from nearby sandstone during drier periods, revealing the complexity of this proxy. The São Mateus record highlights the complex, non-stationary interplay between monsoon strength, SACZ dynamics, and atmospheric processes in shaping central Brazil's hydroclimate.

3.2 Introduction

The Brazilian savanna, or Cerrado, lies in Central Brazil and is the second-largest biome of South America. It is bordered by the Amazonian biome (rainforest) to the north and the Caatinga biome (Brazilian dry forest) to the east. The Cerrado is situated within the austral summer/spring (October-March) precipitation regime of the South Atlantic Convergence Zone (SACZ). The SACZ is a seasonal convective band that forms in a northwest-to-southeast orientation over the continent (i.e., central Brazil – Fig. 3.1), and is one of the main features of the South American Summer Monsoon (SASM). It is maintained by merging two transient moisture fluxes: one following the pattern of the monsoon onshore flow from the north and another originating from frontal systems from the South Atlantic Ocean as they move into the continent westward (Garreaud *et al.*, 2009; Marengo *et al.*, 2012; Zilli *et al.*, 2019). The overall position and intensity of the convective band changes depending on different climatic factors, such as atmospheric circulation, sea surface temperatures in the South Atlantic Ocean, low-level jets, and South Atlantic Subtropical high wind speeds(Garreaud *et al.*, 2009; Marengo *et al.*, 2012; Zilli *et al.*, 2019; Wong *et al.*, 2023).

Previous paleoclimate studies based on stalagmite oxygen isotope ($\delta^{18}O$) records within the SASM/SACZ regime (Fig. 3.1a) investigated changes in the activity of both systems and their association with distinct rainfall patterns (Cheng *et al.*, 2013; Wang *et al.*, 2017; Campos *et al.*, 2019; Wong *et al.*, 2023). They define a rainfall dipole pattern between Northeastern Brazil, which primarily receives moisture from the Intertropical Convergence Zone (ITCZ) at its southernmost position, and the monsoon domain. This dipole pattern was documented at orbital (Cruz *et al.*, 2009; Cheng *et al.*, 2013b; Deininger *et al.*, 2019) to centennial time scales (Novello *et al.*, 2018; Campos *et al.*, 2019; Della Libera *et al.*, 2022). The dipole is established when enhanced convergence in the West (Amazon) of the continent takes place (Fig.3.1b), causing regional air subsidence in the Northeast, which characterizes a subsystem of the atmospheric Walker circulation known as the Bolivian High-Northeast Low system (Rodwell and Hoskins, 2001; Lenters and Cook, 1997; Sulca *et al.*, 2016; Campos *et al.*, 2019). However, the climate dynamics in the center of the dipole, i.e., in central-east Brazil, have not been well defined and understood yet due to the lack of archives recording the climate transition between the dipole extremes over longer time-scales, such as during the Holocene.

Over the Holocene, the dipole pattern is characterized by opposite trends of the $\delta^{18}O$ records across tropical South America towards the late Holocene (LH). In western Amazonia, the tropical Andes, and southern Brazil, increasing moisture reflected by decreasing $\delta^{18}O$ values follows the increase in austral summer insolation (Bird *et al.*, 2011; Bernal *et al.*, 2016). The records from Northeastern Brazil and eastern Amazonia, on the other hand, document increasing aridity reflected by increasing $\delta^{18}O$ values as summer insolation rises (Cruz *et al.*, 2009; Wang *et al.*, 2017; Utida *et al.*, 2020). Despite the clear dipole pattern, in central-east Brazil, at the core of the dipole, climate is relatively stable from mid-to-late Holocene as reflected in regional $\delta^{18}O$ records (Stríkis *et al.*, 2011; Azevedo *et al.*, 2021; Wong *et al.*, 2021). It is associated with a stationary position of the central axis of the SACZ (Fig. 3.1) over this region for the last 6000 years (Wong *et al.*, 2021), implying a stationary influence of the SACZ in these central regions despite its apparent expansion-retraction behavior of the precipitation belt in the areas located further away from its NE-SW axis (Strikis *et al.* 2011; Novello *et al.* 2018; Campos *et al.* 2019; Azevedo *et al.* 2021).

A monitoring program performed for two years in São Bernardo cave (~10km from São Mateus cave) by Moquet *et al.* (2016) shows a significant negative correlation between local rainfall amount and $\delta^{18}O_{precip}$ at both monthly and weekly scales showing that on short time scales, $\delta^{18}O$ does predict rainfall amounts. However, paleo-records from central Brazil suggest that the long-term variability of $\delta^{18}O$ records do not record rainfall amounts so easily (Wortham *et al.*, 2017; Novello *et al.*, 2019; Ward *et al.*, 2019; Azevedo *et al.*, 2021). This likely relates to the existence of multiple large-scale atmospheric processes related to the monsoon, including mixing between different moisture sources and Rayleigh distillation processes. Such processes likely vary significantly on longer time scales, affecting $\delta^{18}O$ values of rainfall, and thus confound any rainfall amount effects recorded in modern rainfall $\delta^{18}O$ values(Ampuero *et al.*, 2020).

Therefore, recent multi-proxy studies investigate paleo-hydroclimate and paleoenvironmental changes in central Brazil using speleothem $\delta^{13}C$ and $^{87}Sr/^{86}Sr$ records to elucidate local hydrological conditions(Wortham *et al.*, 2017; Campos *et al.*, 2019; Ward *et al.*, 2019; Azevedo *et al.*, 2021). Overall, these studies suggest that local precipitation in the central parts of Brazil was indeed decoupled from continental monsoon patterns over long-time scales, either due to changes in moisture sources or Rayleigh distillation processes. For instance, Ward *et al.* (2019) indicate that changes in monsoon intensity at its core may not directly reflect local precipitation amounts downstream (i.e., in central Brazil) based on their $^{87}Sr/^{86}Sr$ and $\delta^{13}C$ records used as proxies for local hydrology. Additionally, Wortham *et al.* (2017) suggest that moisture contributions from the South Atlantic Ocean at sites closer to the coast than the core monsoon region dilute the monsoon signal derived from upstream dynamics. This is reflected by rising $^{87}Sr/^{86}Sr$ values, suggesting an increase in moisture, during overall stable monsoon $\delta^{18}O$ records in central Brazil (Wortham *et al.*, 2017). This decoupling has also been brought up in a recent review study by Gorenstein *et al.* (2022), which compiled 173 studies from South America based on different paleo-archives (speleothems, sediment cores and soil samples), from which a wide selection of proxies was analyzed (e.g., $\delta^{18}O$, $\delta^{13}C$, pollen, mineralogy, grain size, trace-elements). They point out that the paleoclimate records from central-eastern Brazil show the least consistent picture amongst each other and indicate a high variability of the SACZ central axis position during Middle Holocene (MH). This again suggests a decoupling of local moisture conditions in central-eastern Brazil from the overall intensity of the SASM.

Here we present a new speleothem multi-proxy record from central-eastern Brazil based on $\delta^{18}O$ and $\delta^{13}C$ values as well as $^{87}Sr/^{86}Sr$ ratios from São Mateus cave (Fig. 31a), covering the entire Holocene. This is the longest continuous Holocene record from the region so far. We reconstruct the spatiotemporal evolution of the dipole climate transition happening at our study site and discuss the changes in the local environment.

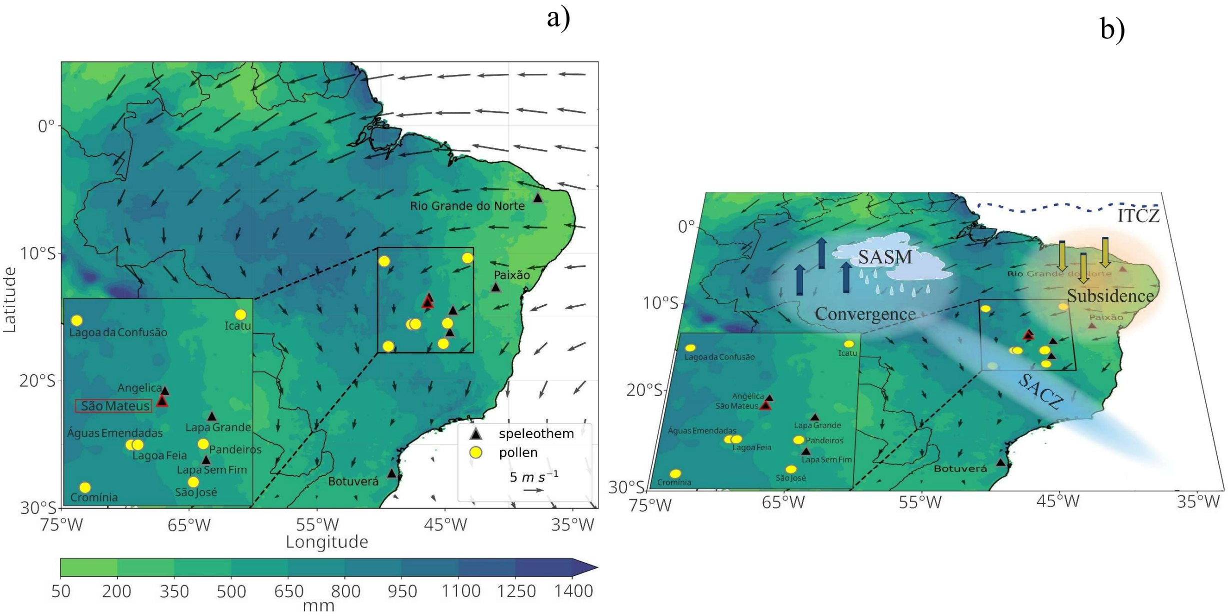

Figure 3.1 - a) Map of tropical South America. Wind and precipitation data represent the December, January, and February (DJF) South American Summer Monsoon features for the forty-year climatology covering the period between 1981 – 2020 CE. The years correspond to the December month of the DJF season, i.e., D(0), J(+1), F(+1). Low-level (850 hPa) horizontal wind data (u, v) were derived from the ERA5 reanalysis. Total seasonal precipitation data were derived from the CHIRPS-2.0 dataset, a gridded rainfall time series based on rain gauges (Hersbach *et al.*, 2023; Funk

et al., 2014). The triangle with the red borders represents the location of São Mateus cave. The other triangles represent the following cave sites: Rio Grande do Norte (Cruz *et al.*, 2009); Paixão cave (Stríkis *et al.*, 2015); Angelica cave (Wong *et al.*, 2021); Lapa Sem Fim cave (Azevedo *et al.*, 2021); Lapa Grande cave (Strikis *et al.*, 2011); Botuverá cave (Wang *et al.*, 2007). The yellow circles are pollen and lake sediment records mentioned in the text: Águas Emendadas (Barberi et al, 2000); Lagoa Feia (Cassino *et al.* 2020); Cromínia (Salgado-Lambouriau *et al.* 1997); São José (Cassino *et al.* 2018); Lagoa da Confusão (Behling 2002); Icatu (de Oliveira *et al.*, 1999); Pandeiros wetland (Sabino *et al.*, 2021). b) Same as a), but with a representation of the precipitation dipole between central and northeast South America. The climatological DJF location of the ITCZ is represented by the blue dashed line and the corresponding location of the SACZ by the black dashed line.

3.2 Site and sample description

São Mateus cave (13.67° S; 46.37° W, 623 m a.s.l. – Fig. 3.1a) is located at the State Park of Terra Ronca (PETER), Goiás state, Central Brazil. The cave is developed in Neoproterozoic karstified dolostone interbedded with limestones of the Sete Lagoas Formation, Bambuí Group (Dardenne, 1987; Auler and Farrant, 1996). In this area, large underground cave systems were formed by drainages flowing westwards from the topographically higher sandstones of the Urucuia Group (Campos and Dardenne, 1997), which forms the Serra Geral Plateau ca. 15 km to the east of the cave site (Supp. Fig. 3.1). The caves were formed by the weathering of the carbonate unit along the trajectory of these rivers (Dardenne, 1987; Auler & Farrant, 1996; Guyot, 1997), such as the São Mateus River. The São Mateus cave system intersects three sedimentary packages: one characterized by doloarenites and recrystallized dolomitic limestone, a second one by intercalations of laminated argillaceous limestones and siliciclastic rocks ranging from claystone to siltstones, and a third package dominated by laminated quartzose siliciclastic rocks, with interbeds of massive to laminated siltstones and very fine to fine sandstones, along with subordinate marly limestones (Supp. Fig. 3.2) (Governo do Estado de Goiás, 2016).

The present-day climate in PETER is characterized as tropical semi-humid, presenting a seasonal pattern of precipitation with wet summer and dry winter seasons. Based on the records of the meteorological station São Vicente (~14 km from São Mateus cave), the mean annual precipitation between 1974 and 2023 is 1,428 mm yr^{-1}. Most of the rainfall (80 %) occurs between October and April during the summer monsoon season and the SACZ active period, feeding the karst aquifer above São Mateus Cave.

The local vegetation is generally characterized as Cerrado (Brazilian savanna), which contains many sub-categories. Karstic areas within the Cerrado biome can present a type of vegetation assembly known as "Mata Seca Decidua" (dry deciduous forest) or "Mata Calcaria" (calcareous forest). Such vegetation can develop on a thin soil cover (~30 cm), changes dramatically between dry and wet seasons, and is highly affected by water availability. The arboreal coverage is 60-90 % during the wet season, and 15-35 % in the dry season. The surface also exhibits calcareous rock pavements with epikarst features, such as dissolution pools, which may accumulate organic matter and soil.

The current study is based on stalagmite SMT16 collected in São Mateus cave at the 700 Hall (Salão Setecentos), which is located ca. 150 m away from the cave entrance (Supp. Fig. 3.2), and ca. 30 m above the modern level of the São Mateus River. The 404 mm-long speleothem section used in this study is a cylindrical aragonite stalagmite formed by acicular crystals without signs of recrystallization (Fig. 3.2b).

3.3 Methods

3.3.1 Chronology and stable isotopes

A total of 18 ^{230}Th/U-ages were determined along the growth axis of SMT. For each sample, ~100 mg of carbonate powder was hand-drilled and collected for the separation of the U and Th fractions (Edwards, 1988). These fractions were then further analyzed using multi-collector inductively coupled plasma-mass spectrometry (MC-ICP-MS) at the Geochronology Laboratory at the University of Minnesota (USA) and at the Institute of Global Environmental Change, Xi'an Jiaotong University (China), following the methods described in Cheng *et al.* (2013a). The final chronology was established by calculating an age-depth model using StalAge (Scholz and Hoffmann, 2011).

For δ^{18}O and δ^{13}C analysis, a total of 1320 samples of powdered carbonate were collected along the stalagmite growth axis with a constant spacing of 0.3 mm between samples using a Sherline Mill device with a 0.1 mm drill bit. The analyses were performed at the Laboratory of Stable Isotopes at the Institute of Geoscience of the University of São Paulo (LES-USP) and at the Laboratory of Geodynamic, Geochronological and Environmental Studies of the University of Brasilia (LEGGA – UnB). At LES, a Thermo-Finnigan Delta Plus Advantage mass spectrometer coupled to a Gas Bench online sample preparation system was used, and at LEGGA, a Thermo MAT 253 attached to a Kiel IV Carbonate. Both oxygen and carbon isotope ratios are expressed in δ-notation, on the Vienna Pee Dee Belemnite (VPDB) scale with the per mil deviation from VPDB calculated using the following equation: $\delta^{18}O = [((^{18}O/^{16}O)_{sample} / (^{18}O/^{16}O)_{VPDB}) - 1] \times 10^3$ (example equation for the oxygen isotope values). Analytical uncertainties (1SD) based on the reproducibility of routinely measured in-house standards is 0.1 ‰ for both analyses.

3.3.2 Strontium isotope analysis

The $^{87}Sr/^{86}Sr$ isotope ratios were determined for the speleothem as well as carbonate host rock and soil samples, the latter two being potential end members for the Sr isotope ratios in the stalagmite. $^{87}Sr/^{86}Sr$ ratios of SMT16 were analyzed by both solution and laser ablation (LA) mass spectrometry (Supp. Table 3.1) at LEGGA-UnB and Johannes-Gutenberg University (JGU) Mainz, respectively. Globally recognized reference materials were used for calibration of the analysis. NIST SRM987 was used to normalize solution-based MC-ICP-MS data (Supp. Table 2). Laser ablation MC-ICP-MS data were calibrated against NanoSr as the main reference material, with JCt-1 and JCp-1 acting as quality controls (Supp. Table 1). The $^{87}Sr/^{86}Sr$ ratios obtained from all three reference materials fell within the range of published solution-based values (Weber *et al.*, 2018, 2020). The results from the two techniques (solution MC-ICP-MS and LA-MC-ICP-MS) are directly comparable due to the uniformity of the calibration procedures. Given the compatibility between these methods, the results of the LA-MC-ICP-MS method will be taken as the main record due to the higher resolution. Further details can be found in Supplementary Text 3.1.

3.3.3 Back-trajectory and clustering analysis

Back-trajectories initiating at the location of São Mateus cave (13.67° S; 46.37° W, 623 m a.s.l.) were computed between 2012-2019 using the Hybrid Single-Parcel Lagrangian Integrated Trajectory model 5 (Hysplit V5.3.0; Stein *et al.*, 2015; Rolph *et al.*, 2017). Back trajectories were calculated daily at a local time of 13 h. Since the most important moisture transport occurs in the lower troposphere, the starting height for the trajectories was set at 1500 m a.s.l. (~850 hPa) and 7 days were considered to track back air parcels. According to Ampuero *et al.* (2020), the 7-day back trajectories can trace the pathway of an air mass back to the point where it was last saturated. This timeline allows us to consider the relevant isotopic fractionation processes that occur during atmospheric moisture transport (Hurley *et al.*, 2012; Ampuero *et al.*, 2020). ERA 5 data were used to run the model (Hersbach *et al.*, 2020) with a spatial resolution of 0.75° × 0.75° and a time step of 6 hours starting at 0:00 UTC. The back-trajectories were chosen if they started on precipitating days and if their numerical error was within tolerance (Ampuero *et al.* 2020). Days with precipitation were defined as days with local precipitation higher than 1 mm computed with data from the Global Precipitation Measurement (GPM; Huffman *et al.*, 2023) at a spatial resolution of 0.25° × 0.25°, with 25 tiles. A total of 681 back-trajectories were selected.

3.4 Results

3.4.1 ^{230}Th/U-dating

All ^{230}Th/U-ages determined for stalagmite SMT (Supp. Table 3.3) have an average 2σ-uncertainty of 0.23 %, yielding a very well-constrained chronology (Supp. Fig. 3.3). Generally high ^{230}Th/^{232}Th isotope ratios throughout the sample document that detrital contamination does not have a significant influence on the final ages, except for two samples, SMT16-2 and SMT16-378. Additional details are presented in Supplementary Table 3. Based on the age model, SMT16 spans the entire Holocene between 11078 and 24 years BP (Supp. Fig. 3.3). In general, SMT16 shows a relatively stable growth rate with an average value of 32 µm/yr until the mid-Holocene, followed by an increase to 43 µm/yr during the late-Holocene (LH, i.e., after 4000 years BP, Supp. Fig.3.3).

3.4.2 δ^{18}O and δ^{13}C values

The stable isotope records (δ^{18}O and δ^{13}C – Fig. 3.2a) have an average temporal resolution of 8 years. The δ^{18}O record shows a steady trend to higher values towards the present with values from -5.4 to -2.1 ‰. The lowest values are observed in the oldest part of the record until ~8200 years BP with a mean value of -4 ‰ (Fig. 3.2a). After a negative excursion centered at 8225 years BP, the values increase marking the transition from the early Holocene (EH) to the middle Holocene (MH). The MH values range around the record mean of -3.3 ‰ until 4305 years BP. At the transition to the LH, the values further increase until the present, with a mean value of -2.9‰.

In contrast to the oxygen isotopes, the δ^{13}C record is marked by a trend to more negative values towards the present with a range between -7.9 to -2.2‰. The highest δ^{13}C values of the record are observed from 11078 to 7882 years BP. Subsequently, the δ^{13}C record shows a gradual decrease until ~2800 BP followed by a stationary trend until the present. There is an overall negative correlation between the δ^{13}C and δ^{18}O time series ($r = -0.5$, $p<0.01$) for the entire period (Supp. Fig. 3.4). However, a spearman's running correlation with a window size of 150 data points representing a temporal resolution of ~1233 years shows that these two proxies show a positive correlation (yet varying) from ~6800 BP until the present, evidencing a coupling for most of the Holocene (Supp. Fig 3.5). Yet, the negative correlation from ~9500-7250 BP indicates a decoupling at the beginning of the period. The cave host rock has a mean value of -2.9‰.

3.4.3 $^{87}Sr/^{86}Sr$ values

The $^{87}Sr/^{86}Sr$ record of SMT (Fig. 3.2a) is composed of 87 data points ranging from 0.71061 to 0.71186. The highest values are observed within the oldest portion of the stalagmite between 11000- and 7900-years BP, peaking at 8200 years BP. Subsequently, until ca. 5000 years BP, the ratios show a plateau with lower values. This is followed by a distinct decrease to generally lower values until the present, with a prominent positive excursion centered at 2213 years BP.

The cave host rock has a mean value of 0.70905, which is much less radiogenic (i.e., lower $^{87}Sr/^{86}Sr$ values) than both soil samples. The upper soil sample ($^{87}Sr/^{86}Sr$= 0.77545±0.00001) is more radiogenic than the bottom one ($^{87}Sr/^{86}Sr$ = 0.71703±0.00001). Thus, the Sr isotope ratio of the stalagmite lies between the soil and host rock values (Fig. 3.2).

To determine the correlation between $^{87}Sr/^{86}Sr$ and the higher-resolution $\delta^{18}O$ and $\delta^{13}C$ records, they were down-sampled to the same number of data points as the lower-resolution strontium isotope record (87 points). The values obtained from the $\delta^{18}O$ and $\delta^{13}C$ records were matched on the depth-scale with the corresponding data points of the $^{87}Sr/^{86}Sr$ record. We observe a positive correlation of 0.71 ($p<0.001$) with the $\delta^{13}C$ record and a negative correlation of -0.45 ($p<0.001$) with the $\delta^{18}O$ values (Supp. Fig. 3.4).

3.4.4 Back trajectories and clustering analysis

The back-trajectory analysis for the period between 2012-2019 at São Mateus cave mainly shows atmospheric transport pathways from the east (73 %) and the north-east (23 %). Both trajectories are associated with the months of higher rainfall contribution at São Mateus between October and March and contribute approximately equally throughout the year, but the eastern cluster has a much higher contribution to the total amount of trajectories during JFM (Supp. Fig. 3.6). Between May and September, there are little to no trajectories, especially from the eastern cluster.

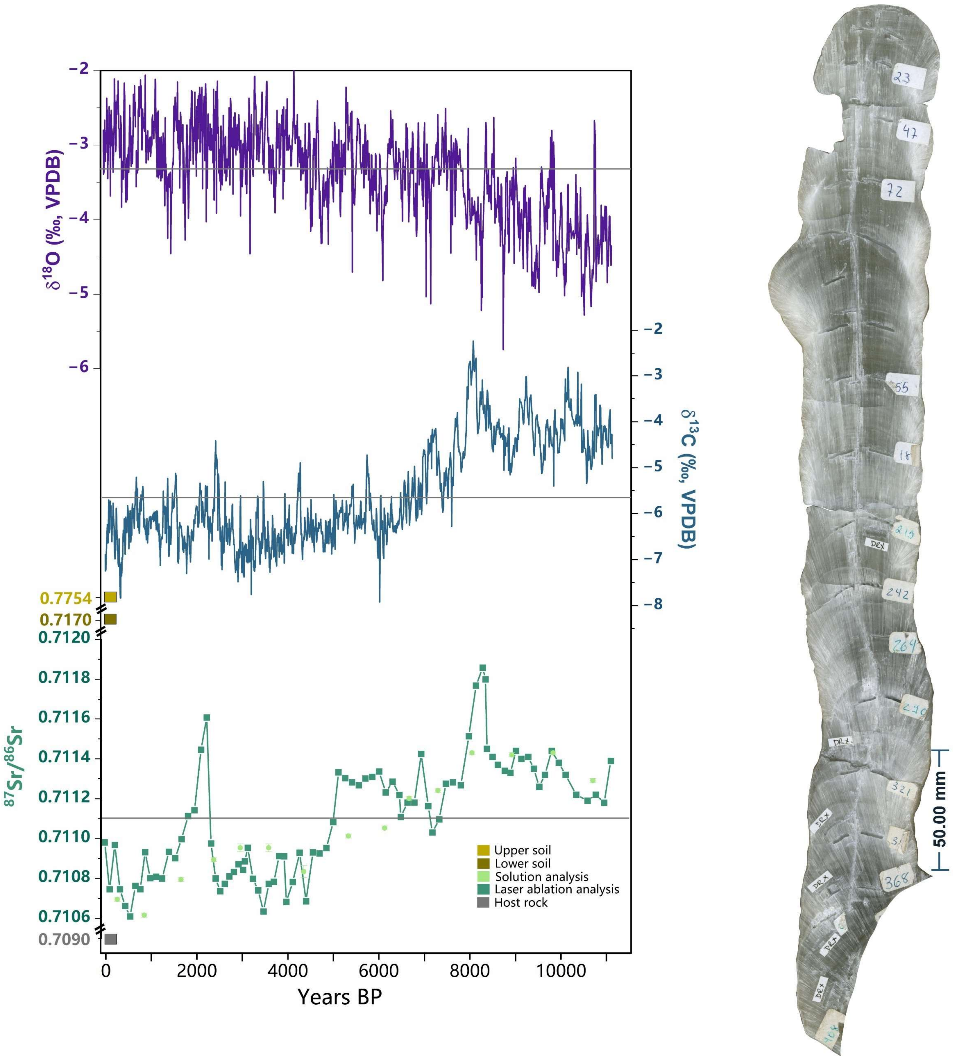

Figure 3.2 – a) SMT16 $\delta^{18}O$ (purple), $\delta^{13}C$ (blue), and $^{87}Sr/^{86}Sr$ records. Dark green squares represent laser ablation analyses; light green circles represent solution analyses. The yellow, brown, and gray squares show the $^{87}Sr/^{86}Sr$ isotope ratios of the upper and bottom soil samples and the host rock, respectively. The light gray line is the mean value of each proxy record. b) Stalagmite SMT16.

3.5General understanding of proxy signal controls

3.5.1 Carbon isotopes

Changes in speleothem $\delta^{13}C$ values are influenced by several factors, such as vegetation type (C_3 vs. C_4) and density above the cave, soil biogenic activity (CO_2 production) versus host-rock $\delta^{13}C$ contribution, if the dissolution of the carbonate host-rock is an open, closed or intermediate system, and prior carbonate precipitation (PCP), all related to local climate conditions (McDermott, 2004; Fohlmeister *et al.*, 2011; Novello *et al.*, 2021). In general, drier conditions result in higher

$\delta^{13}C$ values due to sparser, savanna-type C_4 vegetation (-9‰ to -17‰) and reduced soil CO_2 (Gouveia *et al.*, 2002; Pessenda *et al.*, 2010), longer water residence times (increased PCP, Fairchild and Baker, 2011; Fohlmeister *et al.*, 2020), and increased host-rock contribution ((Novello *et al.*, 2021and references therein). Conversely, wetter conditions result in lower $\delta^{13}C$ values via denser, forest-type C_3 vegetation (-32‰ to -20‰), increased soil CO_2, reduced PCP, and lower host-rock input. In an open system, the percolating water is constantly interacting with the soil air, an infinite reservoir CO_2, which leads the $\delta^{13}C$ to reflect the isotopic composition of the soil CO_2. In a close system, the percolating water is separated from the soil CO_2 and the initial amount of CO_2 in the solution is progressively consumed by the dissolution of the carbonate host-rock, which is reflected in the final $\delta^{13}C$ isotopic composition. In natural environments, it is uncommon that systems operate fully open or close, but rather that the interaction between the percolating water and the host-rock happens in an intermediate state between the two extremes (McDermott, 2004; Fohlmeister *et al.*, 2011; Novello *et al.*, 2021).

A study by Novello *et al.* (2021) using a compilation of 25 stalagmites from tropical South America that cover the last 2000 years shows that the sites within this broad region share similar characteristics in their $\delta^{13}C$ records: an average $\delta^{13}C$ value below -6‰ and most of them show a positive correlation between their $\delta^{13}C$ and $\delta^{18}O$ values (R^2 ranging from 0.20 to 0.56). This correlation indicates that local hydrology was closely associated with the monsoon at most of the sites (documented by the $\delta^{18}O$ values). The dominant $\delta^{13}C$ value of -6‰ was attributed to the prevailing C_3 vegetation above most karst systems. This is in agreement with the $\delta^{13}C$ values below -6‰ during the mid to late Holocene in SMT16 (6000 BP until the present) and the observed R^2 between the SMT16 $\delta^{13}C$ and $\delta^{18}O$ values ranging from 0.2 to 0.5 for the same (Supp. Fig. 3.5).

3.5.2 Strontium isotopes

Strontium isotope ratios ($^{87}Sr/^{86}Sr$) reflect changes in the relative contribution of different Sr sources with distinct $^{87}Sr/^{86}Sr$ values fed by the percolating water into the speleothem (Banner *et al.*, 1996; Weber *et al.*, 2018). Therefore, they are commonly used as a proxy for local hydrology due to the relative contribution of the two main Sr sources of the drip water: Sr leached from the carbonate host rock and from the soils overlying the host rock (Banner *et al.*, 1996; Weber *et al.*, 2018). The soil usually shows more radiogenic (higher) $^{87}Sr/^{86}Sr$ ratios compared to the less radiogenic (lower) values of the carbonate host rock, resulting in an intermediate value between the two end-members in the speleothem. It is often suggested that during wetter conditions, the infiltrating water drains faster through the carbonate host rock, resulting in less leaching, and thus a more radiogenic signal in the speleothem, closer to the $^{87}Sr/^{86}Sr$ ratio acquired from the overlying soil. Conversely, drier conditions lead to a longer residence time of the percolating water in the carbonate host rock, leading to more leaching and thus less radiogenic values in the speleothems (Banner *et al.*, 1996). So far, various studies in Brazil have interpreted the variation in speleothem $^{87}Sr/^{86}Sr$ values in that framework (Novello *et al.*, 2019; Utida *et al.*, 2020; Azevedo *et al.*, 2021). However, other mechanisms have been suggested for variation in speleothem $^{87}Sr/^{86}Sr$ values, such as shifts in the percolating water flow routes (different porosity and permeability, Banner *et al.* 1996; Wortham *et al.* 2017) and inputs of eolian dust to the overlying soils (Banner *et al.*, 1996; Goede *et al.*, 1998; Frumkin and Stein, 2004; Torfstein *et al.*, 2018). The latter studies, despite being from different geological contexts including desert and non-desert regions, associate drier conditions to higher dust mobilization and deposition yielding more radiogenic $^{87}Sr/^{86}Sr$ values. In such a scenario, greater aridity, reduced vegetation cover, and changes in wind lead to increased aeolian dust transport, while during wetter conditions, increased vegetation cover and moisture limits dust mobilization, yielding lower $^{87}Sr/^{86}Sr$ values, closer to the host rock (Banner *et al.*, 1996; Frumkin and Stein, 2004; Torfstein *et al.*, 2018).

3.5.3 Oxygen isotopes

Speleothem $\delta^{18}O$ records in tropical South America are associated with the isotopic signature of the rainfall, which is strongly related to the monsoon system. Within the SACZ region, the amount of local precipitation (i.e., the amount effect) is an important process affecting rainfall $\delta^{18}O$ values. More (less) local precipitation leads to lower (higher) $\delta^{18}O$ values, thus resulting in an anti-correlation with local rainfall amount (Vuille *et al.*, 2012; Moquet *et al.*, 2016; Della Libera *et al.*, 2022). This is a common process in areas within the SASM, such as in central Brazil. This is demonstrated by the monitoring program performed in the nearby cave of Sao Bernardo (Moquet *et al.*, 2016). The authors show that speleothem $\delta^{18}O$ values are anti-correlated with the average DJFM precipitation amount ($r = -0.66$) as well as the average annual precipitation amount ($r = -0.45$) for the past century. This monitoring also showed that the mean dripping water value (-4.2 ± 0.1 ‰ VSMOW, $n = 37$) during the monitoring period (1.5 years) did not change significantly, thus evidencing that there is in fact a minimum 1.5-year residence time of the water in the aquifer. Therefore, the drip water $\delta^{18}O$ represents the weighted annual mean of the rainfall $\delta^{18}O$ and, since most of the recharge occurs during the wet season, the drip water primarily reflects the rainfall $\delta^{18}O$ signature of the wet summer months.

Additionally, the current understanding of rainfall $\delta^{18}O$ values in the SASM regime is that these are dominated by Rayleigh distillation and influenced by convective processes associated with monsoon activity (Ampuero *et al.*, 2020; Orrison *et al.*, 2022). Heavier oxygen isotopes (^{18}O) are preferentially removed from the air mass along its trajectory through precipitation, resulting in a progressive depletion of the remaining air mass (i.e., in more negative $\delta^{18}O$ values, Ampuero *et al.*, 2020; Orrison *et al.*, 2022). Therefore, rainfall $\delta^{18}O$ values in the SASM domain are also affected by the degree of rainout upstream that along the air mass trajectory from the tropical Atlantic into the continent (Fig. 3.1). As the air mass moves further inland, it becomes progressively more depleted in ^{18}O (Vuille *et al.*, 2012; Ampuero *et al.*, 2020). This leads to an isotope effect in rainfall that is unrelated to the amount of rainfall on the study site (Ampuero *et al.*, 2020; Della Libera *et al.*, 2022; Orrison *et al.*, 2022). Therefore, a direct assessment of local hydrology exclusively using oxygen isotopes may be difficult due to multiple other processes potentially influencing the $\delta^{18}O$ values.

3.5.4 Potential effects of changes in seasonality

Strong seasonality is a major characteristic of the hydroclimate in the Cerrado and thus has a major impact on its vegetation. Thus, it is important to discuss the possible implications for our proxy records. Both the total amount of wet season rainfall and the distribution of precipitation (season length, number of rainy days, intensity and length of dry spells) will have an impact on vegetation, soil moisture and infiltration (Bustamante *et al.*, 2012; Klink *et al.*, 2020; Hofmann *et al.*, 2023). However, rainfall distribution has a stronger impact on tree–grass changes in the Cerrado, given that a pronounced dry season determines fuel accumulation and fire frequency, and that the resulting fire regime strongly shapes the tree–grass balance (Bustamante *et al.*, 2012; Klink *et al.*, 2020; Hofmann *et al.*, 2023). Therefore, even if the total amount of the wet season rainfall remains similar, the crucial factor might be the relative duration between wet and dry season. For instance, more clustered rainfall events in the wet season imply longer dry spells, which would result in a higher fire risk and favor grasses over trees (Bustamante *et al.*, 2012; Klink *et al.*, 2020; Hofmann *et al.*, 2023).

As ~80% of precipitation occurs during the wet season (monsoon), our SMT16 $\delta^{18}O$ record is strongly biased towards the wet season and thus represents changes in both wet season precipitation amounts and large-scale SASM/SACZ variability (see section 3.5c). Yet, the $\delta^{18}O$ signal is smoothed in the aquifer and reflects the weighted mean of the rainfall signal of several years (Moquet *et al.*, 2016). In contrast, $\delta^{13}C$ values and Sr isotopes will respond more directly to the local hydrology because both proxies are influenced by environmental factors, such as vegetation dynamics, soil moisture, and prior calcite precipitation, which are all more affected by the length of the dry season.

In summary, even if the observed trends between the different proxies are not similar, this divergence may provide important information on the seasonal distribution of rainfall. For instance, intervals showing more positive $\delta^{13}C$ values and evidence of C_4 vegetation expansion could be interpreted as phases of prolonged dry seasons, even when the $\delta^{18}O$ values indicate a relatively stable or strong wet season precipitation. Thus, the proxies dominated by local hydrology ($\delta^{13}C$ and Sr isotopes) are more responsive to the length of the dry season, which directly affects vegetation cover and fire regimes in the Cerrado.

3.6 Environmental changes in central-eastern Brazil during the Holocene

The general trend of the SMT16 $\delta^{13}C$ record, i.e., higher values at the beginning of the Holocene from 11000 to 7500 BP followed by a distinct decrease and stabilization at lower values towards the present, is also observed in nearby stalagmite records from Lapa Sem Fim (LSF, Azevedo *et al.*, 2021) and Lapa Grande (LG, Stríkis *et al.*, 2011) (Fig. 3.3c). The strong agreement between the SMT16 $\delta^{13}C$ record and these records indicates a widespread regional change in the environmental conditions and vegetation throughout the Holocene. This trend in $\delta^{13}C$ values may reflect a progressively wetter climate (i.e., more precipitation in the wet season and/or longer wet seasons) and an increase in vegetation density in the LH (lower $\delta^{13}C$ values) compared to a drier EH (higher $\delta^{13}C$ values).

The stratigraphically well-constrained pollen record of Lagoa Feia core (~250 km SW of São Mateus cave, Fig. 3.1 and 3.4d, Cassino *et al.*, 2020; Escobar-Torrez *et al.*, 2024) also points to generally drier climate during the EH until ~7200 BP in the region, indicating that this period was marked by a series of dry episodes interspersed with wetter ones (Cassino *et al.*, 2020). The authors also performed a PCA analysis to access regional patterns of vegetation variability in Central Cerrados based on the pollen records of Lagoa Feia (Cassino *et al.*, 2020), São José (Cassino *et al.* 2018) and Salitre (Ledru *et al.*, 1996) (Fig. 3.4c) that also evidences this drier period with wet events during the EH (Cassino *et al.*, 2020). Similar variations are visible in the SMT16 $\delta^{13}C$ record during the EH suggesting rapid environmental shifts (Fig. 3.4b). Other pollen studies from central Brazil confirm that conditions during the EH were generally dry, such as Águas Emendadas (Barberi *et al.*, 2000), Cromínia (Salgado-Labouriau *et al.*, 1997), São José (Cassino *et al.*, 2018), and Lagoa da Confusão (Behling, 2002) (Fig. 3.1), but most of these records have a low temporal constrain. Therefore, we take Lagoa Feia pollen data, along with the general understanding of the other pollen records, to support the hydroclimatic interpretation of the SMT16, LG, and LSF speleothem records, suggesting a reduction in the length and intensity of the rainfall seasons and generally more severe dry seasons during the EH during a period of weakened SASM (Bernal *et al.*, 2016: Cassino *et al.*, 2020).

The major transition observed in the SMT16 $\delta^{13}C$ record to more negative values occur in the MH after its largest excursion at ~8000 BP. The shifts in the LG (~7900 BP) and LSF (~7200 BP) $\delta^{13}C$ records show a broadly similar timing (Fig. 3.3), which might indicate a regional increase in vegetation density and C_3 plants. The Lagoa Feia pollen data corroborate this transition to increased humidity with the onset of aquatic plants, higher and more stable lake levels, and a higher occurrence of forest-type taxa (Cassino *et al.*, 2020). This change in vegetation during the MH was likely triggered by the initial increase in humidity in the SASM regions due to increasing austral summer insolation (10°S), therefore providing more uniform rainfall seasons and shorter dry ones (Cruz *et al.*, 2009; Bernal *et al.*, 2016; Smith and Mayle, 2018).

The further increase in summer insolation might have favored similar-to-wetter conditions during the LH. The lower $\delta^{13}C$ values (~ -5‰ or lower) in SMT16, LSF, LG, and Angelica cave (ANG, Wong *et al.*, 2021, Figs. 3.1 and 3.3) suggest an overall more stable precipitation regime and environment with denser vegetation, higher abundance of C_3-plants (Novello *et al.*, 2021), and less variable climate conditions compared to the MH and EH (Fig. 3.3). The pollen record of Lagoa Feia (Fig. 3.4d) shows a broad expansion of the woody Cerrado vegetation and a sharp rise in water level-associated taxa (Escobar-Torrez *et al.*, 2024). In addition, the Pandeiros wetland (Sabino *et al.*, 2021) also suggests a generally wetter LH, even though short-term dry events are present throughout the period. This overall coherence amongst different records highlights the transition to relatively wetter climate throughout the year (i.e., shorter dry seasons) and a landscape with more dense vegetation after the MH in central-eastern Brazil.

Based on this interpretation of the speleothem $\delta^{13}C$ record, we can now assess the Sr isotope data in some more detail. The striking positive correlation ($r=0.7$, $p<0.01$ – Fig. 3.2, Supp. Fig.4) between the SMT16 $\delta^{13}C$ and Sr isotope records suggests that wetter conditions generally resulted in lower speleothem $^{87}Sr/^{86}Sr$ ratios. This is clearly at odds with the classical interpretation of $^{87}Sr/^{86}Sr$ ratios in speleothems (Banner *et al.*, 1996, compare section 5) applied in previous studies from South America using both proxies (Novello *et al.*, 2019; Utida *et al.*, 2020) or the ones using $^{87}Sr/^{86}Sr$-$\delta^{18}O$ comparisons (Wortham et al, 2017; Ward *et al.*, 2019 – see Supp. Tex. 2). In that classical interpretation, drier conditions lead to more carbonate host-rock Sr contribution to cave drip water, and therefore to lower speleothem $^{87}Sr/^{86}Sr$ ratios. This explanation does not work for the SMT16 record, which shows a positive correlation between $\delta^{13}C$ and $^{87}Sr/^{86}Sr$, hence higher $^{87}Sr/^{86}Sr$ ratios at increased aridity.

In our study, the long-term in-phase relationship between $^{87}Sr/^{86}Sr$ and $\delta^{13}C$ values suggests that the above mechanisms are unable to explain the SMT16 signals, at least on this time-scale. Since the $\delta^{13}C$ record agrees well with records at other localities (LG, LSF) and has a relatively straightforward hydroclimatic interpretation, it appears that the $^{87}Sr/^{86}Sr$ signal at SMT16 differently responds to hydroclimate change than at other sites. One explanation for higher $^{87}Sr/^{86}Sr$ during drier periods is that variations in $^{87}Sr/^{86}Sr$ could be controlled by the flow-route and level of interaction of the infiltrating water with silt and clay layers, which are more radiogenic compared to the carbonate host rock (Banner *et al.*, 1996; Wortham *et al.*, 2017). However, this would require a process that leads to changes in vadose flow routes, in turn depending on rainfall variations, and enhances the interaction with silt and clay layers. A diffuse flow through low porosity/permeability silicate layers during drier conditions would increase the Sr radiogenic signal, whereas a fracture flow through carbonate layers during wetter conditions would decrease this signal (Musgrove and Banner, 2004; Wortham *et al.*, 2017). São Mateus cave is indeed situated in a geological setting where the limestone bedrock clearly intersects siliciclastic rocks (section 3.2, Supp. Fig. 3.2). This could explain the increased $^{87}Sr/^{86}Sr$ ratios in SMT16 during the EH and the subsequent gradual decrease in $^{87}Sr/^{86}Sr$ over the Holocene due to diminished interaction with these layers in the epikarst because of increasing local precipitation and different flow-routes. However, with the current data, this process is difficult to prove.

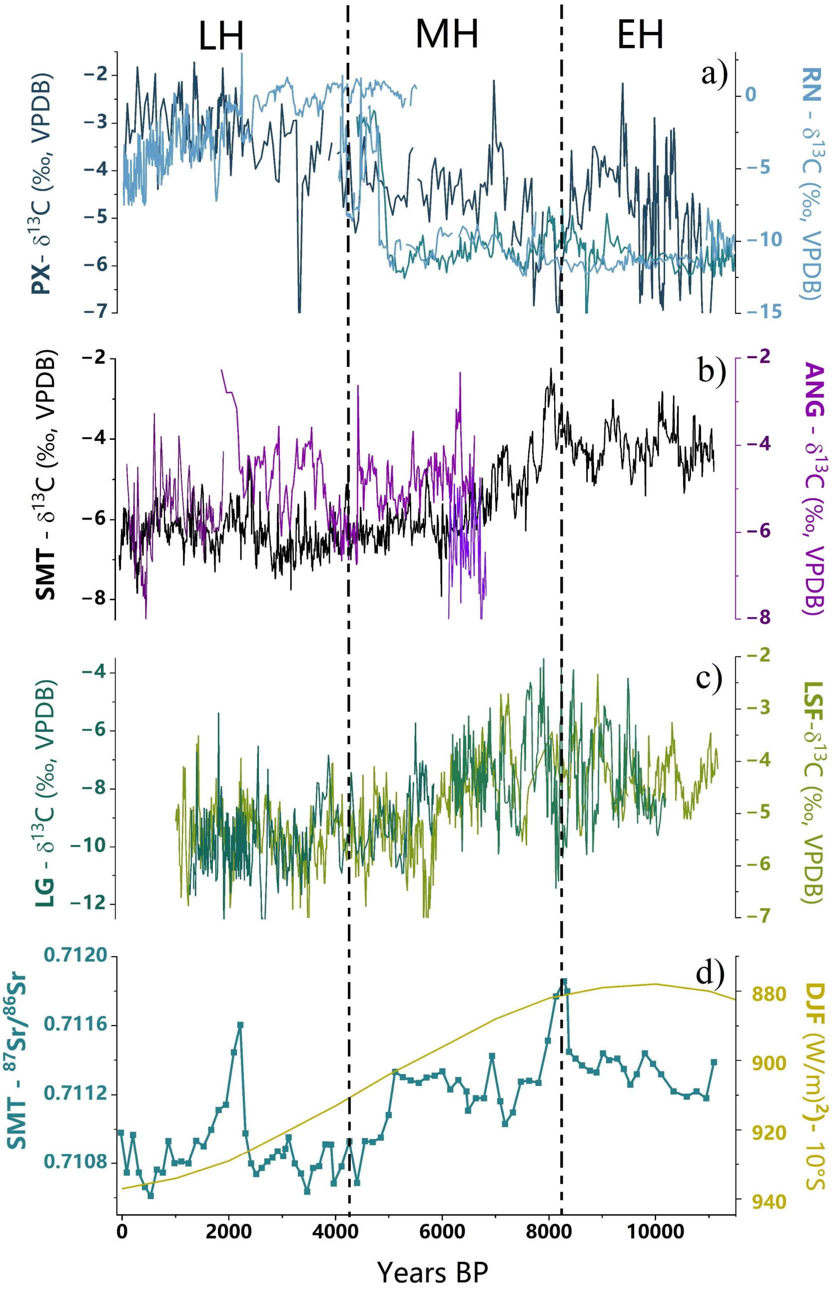

Figure 3.3 -Comparison of SMT16 $\delta^{13}C$ record (black) with records from central-eastern and Northeastern Brazil. a) Rio Grande do Norte cave (Cruz e al., 2009) and Paixão cave (Stríkis *et al.*, 2015) in northeastern Brazil region; b) Angelica cave (Wong e al., 2021) and São Mateus cave (this study) in central-eastern Brazil; c) Lapa Grande cave (Stríkis e al., 2011) and Lapa Sem Fim cave (Azevedo *et al.*, 2021) in central-eastern Brazil; d) SMT16 $^{87}Sr/^{86}Sr$ record with the DJF insolation for 10ºS (Berger and Loutre, 1991).

Another mechanism to increase Sr isotope values of speleothems in dry conditions is the deposition of windblown dust, as already explored in other studies (Banner *et al.* 1996; Goede *et al.* 1998; Frumkin and Stein, 2004). Eolian dust deposition on the soils above the cave can readily change speleothem $^{87}Sr/^{86}Sr$ ratios, as it provides weatherable material with potentially distinct $^{87}Sr/^{86}Sr$ ratios (Banner *et al.*, 1996; Frumkin and Stein, 2004; Torfstein *et al.*, 2018; Cruz *et al.*, 2021). The Urucuia Group sandstone unit, to the east of São Mateus cave, is a potential dust source with highly radiogenic Sr isotope ratios (0.7299 ± 0.0001; Roland, 2018). Even today, in a semi humid climate around São Mateus cave, dust storms are reported by locals, especially in the dry season. Therefore, in an overall drier regional setting at São Mateus cave during the EH with longer, more severe dry spells, much more frequent episodes of dust transportation may have occurred at our site. The generally drier environment and longer extent of the dry seasons might have enabled more intense weathering and greater dust mobilization from Urucuia´s friable rocks towards the west (Supp. Fig. 3.1). The more radiogenic $^{87}Sr/^{86}Sr$ from Urucuia sediments would then be an important allochthonous Sr source to the cave site and overprint the Sr signal of the water residence time in the epikarst when the highest $\delta^{13}C$ values in SMT16 indicate dry conditions (Fig. 3.3). During the MH and LH, with the increase of precipitation throughout the year, shorter dry seasons and more vegetation cover, the deposition of dust would be strongly reduced and contribute much less, if at all, to the $^{87}Sr/^{86}Sr$ speleothem signal (Frumkin and Stein, 2004). Therefore, given the proximity to Urucuia group rock exposures, this mechanism might have been an important factor in the observed major changes in Sr isotope ratios between the EH and the LH.

Finally, the similar pattern of the SMT16 $\delta^{13}C$ values and $^{87}Sr/^{86}Sr$ ratios with the vegetation variability curve from Cassino et al (2020) (Fig. 3.4) shows how these three proxies could have co-varied at that time: the dry/wet episodes cause concomitant lower/higher local moisture, sparser/denser vegetation and higher/lower contribution of the more radiogenic Sr source, either by the different flow routes or the increased dust deposition. Cassino *et al.* (2020) suggest that a sequence of centennial-scale moisture oscillations occurred during this period leading to a repeated increase and decrease in arboreal Cerrado and dry forest cover along with changes in lake levels. Stríkis *et al.* (2011) also points out that central-eastern Brazil was affected by the rapid meltdown of ice caps in the Northern Hemisphere that led to abrupt wet events in tropical South America until about 7000 BP. Since soil moisture is the main factor driving arboreal cover in Cerrado regions (de Assis *et al.*, 2011; Terra *et al.*, 2018), this is consistent with the oscillations observed in SMT16 $\delta^{13}C$ and the $^{87}Sr/^{86}Sr$ ratios.

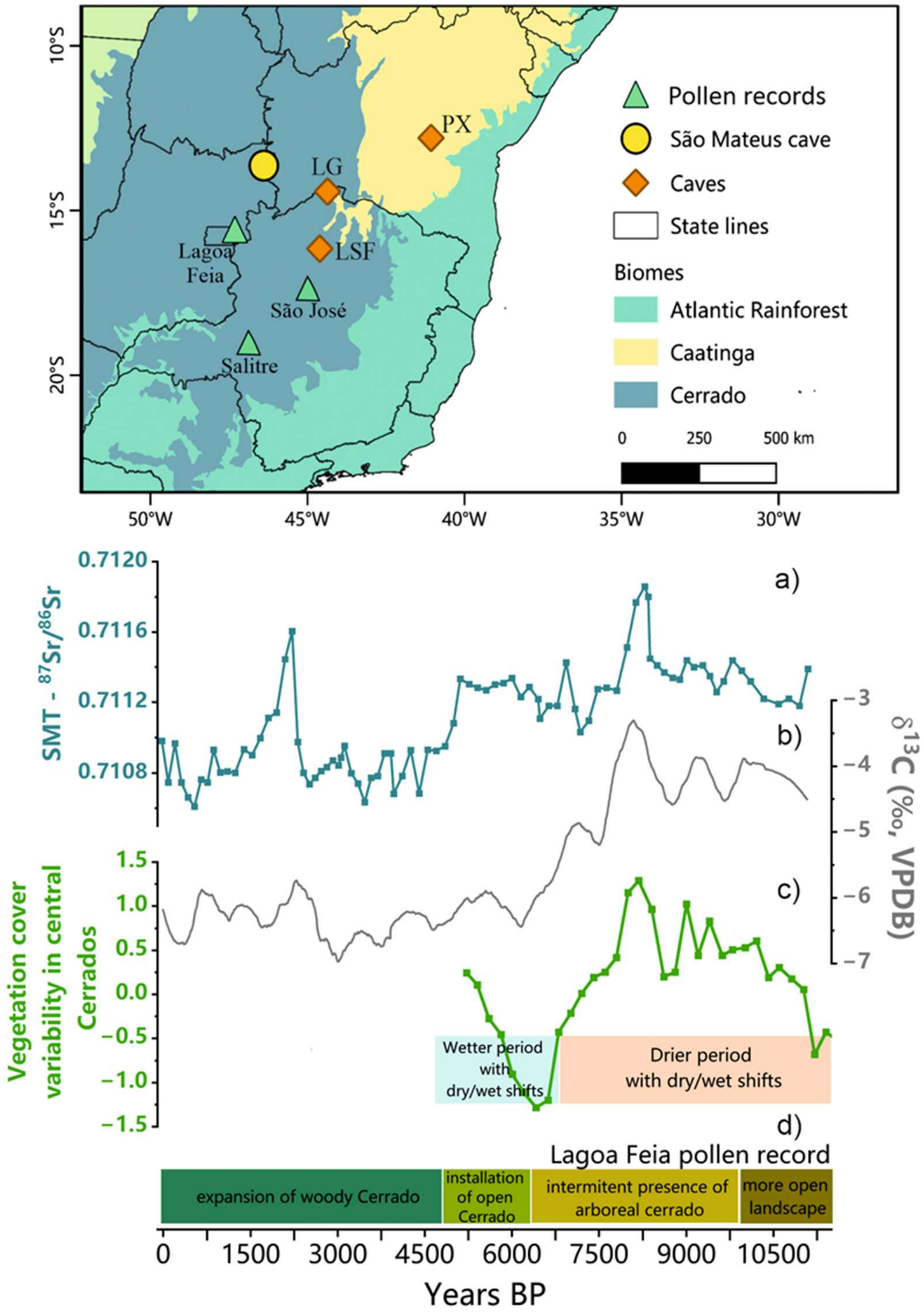

Figure 3.4 - (top) Map of central-eastern and northeastern Brazil records with the study sites discussed in the text: Paixão cave (Stríkis *et al.*, 2015); Lapa Sem Fim cave (Azevedo *et al.*, 2021); Lapa Grande cave (Strikis *et al.*, 2011); Lagoa Feia (Cassino *et al.* 2020); São José (Cassino *et al.* 2018); Salitre (Ledru *et al.* 1996). (bottom) Comparison between: a) SMT16 ^{87}Sr/^{86}Sr record (blue squares); b) smoothed SMT16 δ^{13}C record (gray); c) scores for vegetation cover variability curve performed by Cassino et al (2020) representing vegetation trends in central Cerrado (green) with the correspondent climate interpretation; d) interpretation of Lagoa Feia pollen record from Cassino *et al.* (2020) and Escobar-Terra *et al.* (2024).

3.7 Long-term evolution of central-eastern Brazil speleothem $\delta^{18}O$ values during the Holocene

Considering the long-term drier-to-wetter trend in local hydroclimate conditions during the Holocene in central-east Brazil, the remaining question is what drives the long-term increase in SMT16 $\delta^{18}O$ values. The $\delta^{18}O$ values of speleothems from the São Mateus cave region have been interpreted as a proxy for rainfall amount related to SACZ activity in central Brazil, where lower $\delta^{18}O$ values are associated to a stronger SACZ and consequently wetter conditions, and vice versa for higher $\delta^{18}O$ values (Moquet *et al.*, 2016; Novello *et al.*, 2018, also see section 3.5). Therefore, the long-term increase in the SMT16 $\delta^{18}O$ values throughout the Holocene would indicate a progressively lower contribution of the SACZ and consequently drier conditions. The processes controlling the $\delta^{13}C$ and $\delta^{18}O$ values in tropical regions affect both proxies in the same direction, typically resulting in a positive correlation (see section 3.5; Novello *et al.*, 2021). Yet, the long-term increase in the SMT16 $\delta^{18}O$ values throughout the Holocene is opposite to the scenario described above based on the $\delta^{13}C$ values.

The spearman running correlation between the SMT16 $\delta^{13}C$ and $\delta^{18}O$ records on shorter time-scale intervals reveals a non-stationary correlation through time with a negative correlation during the EH (average of -0.2) and a positive one after ~6500 years BP, mostly ranging between 0.2 and 0.4 (Supp. Fig. 3.5). This demonstrates that while a negative correlation characterizes the long record ($r = -0.5$), a positive correlation between oxygen and carbon isotopes is present on the millennial time-scale during the mid-MH to LH, agreeing with the correlations observed for tropical South America speleothem $\delta^{13}C$ and $\delta^{18}O$ records (Novello *et al.* 2021). This analysis also shows that the correlation between $\delta^{13}C$ and $\delta^{18}O$ is non-stationary throughout the Holocene. However, since the focus of this paper is on the long-term trends over the Holocene, millennial-scale variations are not discussed in detail here.

During this period, several studies from central Brazil observed a detachment between SACZ activity and local rainfall conditions (Wortham *et al.* 2017; Ward *et al.* 2019; Novello *et al.* 2019; Gorenstein *et al.* 2022). This suggests that the long-term trends in the $\delta^{18}O$ records from the region reflect the supra-regional effect of the SACZ – i.e., its changing intensity and spatial variability (Novello *et al.*, 2018; Wong *et al.*, 2021; Gorenstein *et al.*, 2022) – and/or a source effect (Wortham *et al.*, 2017; Bao *et al.*, 2023)rather than solely amount effect, even if this is the case now for interannual and decadal averages documented for present day conditions (Moquet *et al.* 2016).

Existing $\delta^{18}O$ records from central-east Brazil do not appear to be strongly influenced by the increase in insolation (Fig. 3.5a) (Wong *et al.* 2021). The Angelica cave (ANG, Wong *et al.*, 2021) record, near to our study site, that covers the last 6800 years, and the LSF and LG records located more southwards (Fig.3.1) do not present major trends in their $\delta^{18}O$ records (Fig. 3.5a), which was interpreted as a relatively constant SACZ activity throughout the Holocene. In fact, the SMT16 $\delta^{18}O$ values also do not show an insolation trend during this period after 6800 years BP. However, the SMT16 $\delta^{18}O$ record is longer than the adjacent $\delta^{18}O$ record of ANG, revealing that the trend towards higher $\delta^{18}O$ values begins in the EH and lasts until the end of the MH (Fig. 3.5a). Therefore, Wong *et al.* (2021) did not find a good relationship with the insolation trend because their record is much shorter than SMT16. Nonetheless, this increase in $\delta^{18}O$ values is not visible in the central-eastern records slightly south that also expand into the EH (LG and LSF, Fig. 3.3).

The evolution of the SASM/SACZ systems during the Holocene on a transect of speleothem records between northeast and southeast Brazil (Fig. 3.5a) shows a consistent opposite pattern in the trends of the $\delta^{18}O$ values between the Rio Grande do Norte record in NE Brazil (RN, Cruz *et al.* 2009) and the Botuverá record in SE Brazil (BTV – Wang *et al.*, 2007; Bernal *et al.*, 2016).The increase in austral summer insolation from early-to-late Holocene leads to the intensification of the SASM in western Amazonia (van Breukelen *et al.*, 2008; Bird *et al.*, 2011) that reaches south and southeast Brazil (BTV) and leads to a drying in northeastern Brazil (RN site) (Fig. 3.1), clearly evidencing the dipole pattern during the Holocene (Bernal *et al.* 2016; Utida *et al.* 2020; Cruz *et al.* 2009) (Fig.3.5a). The trend in the SMT16 $\delta^{18}O$ record is broadly concomitant with insolation and appears to resemble, even if to a lesser degree, the $\delta^{18}O$ trend of the records in NE Brazil, such as RN and particularly Paixão cave (PX, Stríkis *et al.*, 2015), located ~600 km to the east of São Mateus cave (Figs. 3.4 and 3.5a). This suggests that, even though the São Mateus cave area is at the northern margin of the SACZ, it is located between the dipole boundaries and can still be influenced by the climate patterns from northeast Brazil, capturing a unique signal that is not seen in the other central-eastern records.

This shows that the SMT16 $\delta^{18}O$ record in fact reflects the supra-regional effect of the SACZ and its spatial variation, but does not clarify the underlying issue of the local hydroclimate conditions. Back-trajectory analysis performed for São Mateus cave site shows the two distinct moisture sources that feed the SACZ. One from a more northeastward position following the pattern of monsoon onshore flow originating in the equatorial Atlantic Ocean (EAO), and a second one coming via westerly trade winds from the South Atlantic Ocean (SAO) (Fig. 3.5b). This demonstrates that, even for present-day conditions, there are two moisture trajectories bringing moisture to the area, suggesting that the $\delta^{18}O_{precip}$ signatures can also be affected by other factors in the region, such as a source effect (Bao *et al.*, 2023). Yet, it is observed that the local amount effect currently plays an important role (Moquet *et al.* 2016) and there is a dominant trajectory in place (Fig. 3.5b, Supp. Fig. 3.6). Although this effect is not investigated in the monitoring study performed by Moquet *et al.* (2016), it could be considered as an important mechanism, particularly for longer time scales (e.g., multi-millennial), where a different configuration of atmospheric circulation might have been in place, such as during the EH-MH period (e.g. Wolf *et al.*, 2023). The low insolation and resultant weaker SASM may have altered the atmospheric circulation patterns as we understand them today (Gorenstein *et al.*, 2022), affecting the direction and intensity of moisture trajectories compared to the ones currently observed.

The low SMT16 $\delta^{18}O$ values during the EH could reflect then a higher influence of the EAO moisture source over the area. As revealed by previous studies (Cruz *et al.* 2009; Utida *et al.* 2020), the humidity in the NE region has an anti-phase relationship with the SASM/SACZ regions during the Holocene, presenting wetter conditions during the EH-MH given that the ITCZ (EAO source) was more active over NE Brazil during this period, whereas SASM records present drier conditions. Since the coupling between local humidity and atmospheric variability is well-established at RN (Utida *et al.*, 2020; Cruz *et al.*, 2009), the RN $\delta^{18}O$ and $\delta^{13}C$ records suggest increased precipitation in the northeast region during the EH and the MH given the concomitant low $\delta^{18}O$ and $\delta^{13}C$ values (Figs. 3.5 and 3.3, respectively) with the presence of Cerrado vegetation and a longer rain season (Utida *et al.* 2020). Therefore, a more southern position of the ITCZ during the EH and the mid-MH must have strengthened the EAO moisture source, which already has a more depleted $\delta^{18}O_{precip}$ signal (Supp. Fig.3.7), and since São Mateus cave is located further south, it may have been further depleted when it reached the cave site due to the degree of rainout upstream (Bao *et al.*, 2023). As insolation gradually increased after the mid-Holocene, these patterns likely reorganized, leading to the progressive shift to the major contribution of the more enriched SAO moisture source (Supp. Fig. 3.7) and the establishment of the current SACZ system after ~6500 BP.

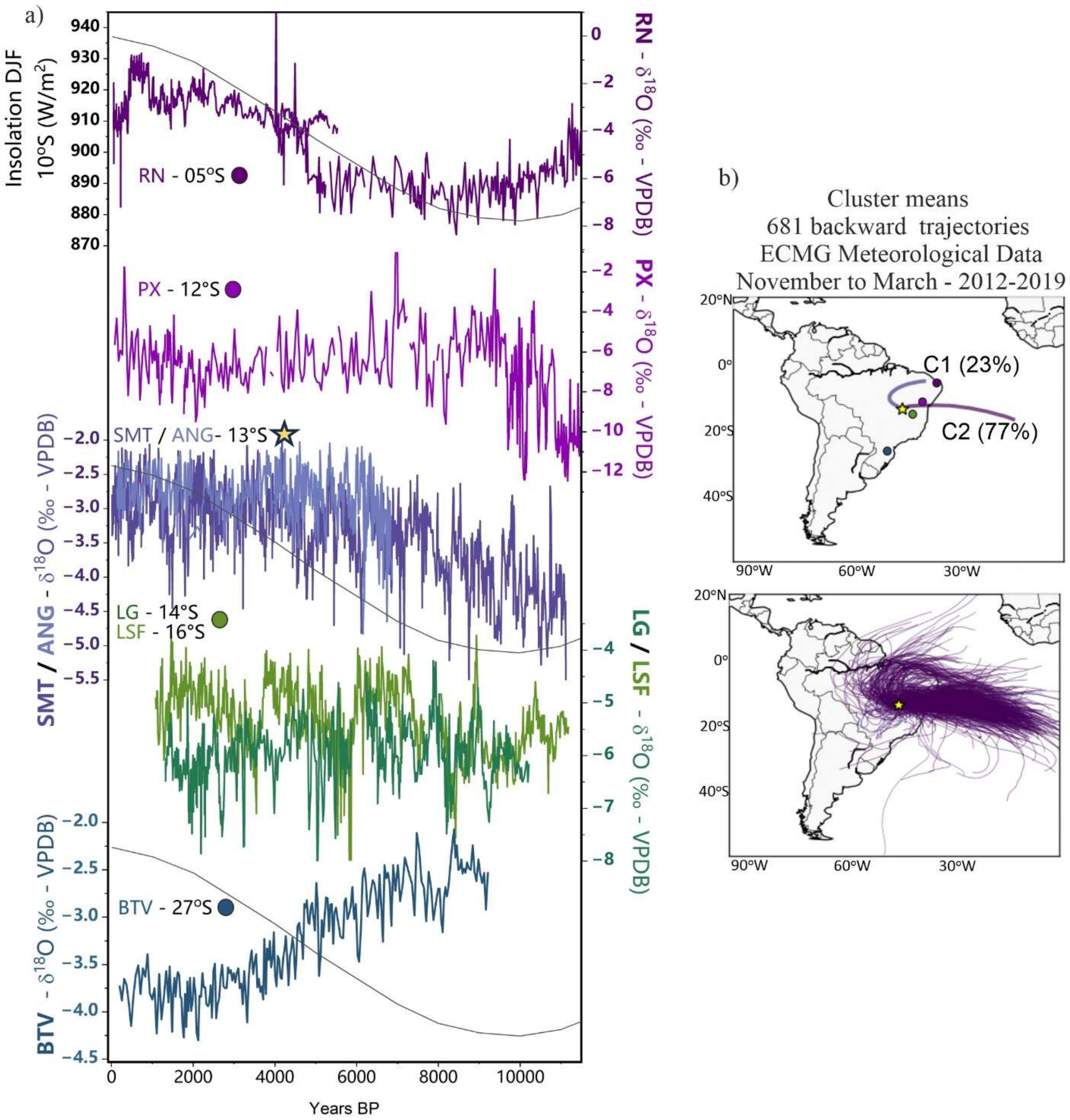

Figure 3.5 - a) NE-SE South America transect of δ¹⁸O records. Top to bottom: Rio Grande do Norte (Cruz *et al.*, 2009); Paixão cave (Stríkis *et al.*, 2015); São Mateus cave (this study); Lapa Sem Fim cave (Azevedo *et al.*, 2021); Lapa Grande (Strikis *et al.*, 2011); Botuverá cave (Wang *et al.*, 2007). Insolation curve for 10ºS shown in black, with increasing values to the top. b) Clusters of 7-day back-trajectories (top) Mean back-trajectories for each cluster with their frequency (C1, C2); regarding the origin, the trajectories can be sorted in North-East (C1) and East (C2). Dots represent each cave site mentioned above. (bottom) All back-trajectories corresponding to top panel.

Moreover, as observed in the PX $\delta^{18}O$ and $\delta^{13}C$ records, the EH also shows extremely low values (Fig. 3.5a), and the pollen record from Icatu River (De Oliveira *et al.*, 1999 – Fig. 3.1) is the only one around SMT that evidences gallery and tropical humid forest and a wet period during EH until ~6700 BP. Thus, the low SMT16 $\delta^{18}O$ values do not necessarily reflect the actual rainfall amount at the cave site for the early and mid-MH, but instead the intermittent influence of the EAO source. This demonstrates how, on the one hand, the SMT16 $\delta^{13}C$ record follows the overall drier-to-wetter hydroclimate trend observed in other SASM sites throughout the Holocene, along with the other central records LSF and LG (Figs. 3.3 and 3.4), where the SASM activity gets stronger with increasing insolation (Bernal *et al.*, 2016). On the other, the SMT16 $\delta^{18}O$ record seems to be also influenced by atmospheric changes that lead to similar $\delta^{18}O$ pattern to the NE region and to a certain degree reflects this opposite pattern during the EH (Fig. 3.5a).

3.8 Conclusions

The SMT16 $\delta^{13}C$ record reveals a drier than present scenario during the early and mid-Holocene, in agreement with other regional speleothem $\delta^{13}C$ records and pollen data from central Brazil. This suggests an increase of water availability in the region throughout the Holocene associated with a denser vegetation. The strong positive correlation between the SMT16 $\delta^{13}C$ values and $^{87}Sr/^{86}Sr$ ratios indicates that a similar geochemical process or environmental setting affected these proxies during the Holocene, which is, however, different from the classical interpretations. Still, the $^{87}Sr/^{86}Sr$ ratios imply changes in local hydrology, where more (less) radiogenic values occur during drier (wetter) periods. We propose two mechanisms that may account for this: 1) how infiltrating water interacts with more radiogenic silt and clayey layers in the bedrock during drier periods compared to wetter periods, with diffuse flow through less permeable silicate layers increasing the radiogenic signal, while fracture flow through carbonate layers during wet conditions resulting in a decrease in the Sr ratio; 2) increased input of windblown dust from a more radiogenic source (Urucuia sandstone unit) during drier periods with sparser vegetation would increase the speleothem Sr isotope ratios, while reduced input from this source during wetter periods and denser vegetation would result in less radiogenic signatures closer to the limestone bedrock. This highlights that Sr isotopes are a site-specific proxy and local settings should be considered.

The long-term trend of the SMT $\delta^{18}O$ record is consistent with large scale $\delta^{18}O$ patterns in South America. However, this long-term trend responds to both variations in local moisture and the degree of rainout upstream that occurs during the moisture transport from the ocean to the cave site. From the early-to-late Holocene, it follows the increase in austral summer insolation, similar to records from NE Brazil, reaching a plateau during the late Holocene similar to other SACZ records. The low insolation and a resulting weak monsoon system during the early and middle

Holocene enabled rapid climate variability and different atmospheric conditions than observed today. Therefore, the SMT area was possibly more strongly influenced by other moisture sources from the NE, and the lower $\delta^{18}O$ values resulted from the degree of rainout upstream of the air masses reaching the area during this time. With the progressive increase in insolation and the re-establishment of the monsoon system, the influence from the South Atlantic source increased, as observed in the modern-day back trajectory analysis, which contributes to the formation of the SACZ.

CRediT authorship contribution statement

Marcela Eduarda Della Libera: Writing – review & editing, Writing – original draft, Formal analysis, Conceptualization, Investigation. **Julio Cauhy:** Writing – review & editing, Writing – original draft, Formal analysis, Investigation. **Cintia Stumpf:** Writing – review & editing, Formal analysis. **Roberto V. Santos:** Resources, Funding acquisition. **Francisco W. Cruz:** Resources, Writing – review & editing, Funding acquisition. **Nicolas M. Strikis:** Writing – review & editing. **Luciana F. Prado:** Resources. **Jean-Sebastian Moquet:** Formal analysis. **Michael Weber:** Writing – review & editing, Formal analysis. **Rebecca Orrison:** Writing – review & editing. **Hai Cheng:** Resources. **R. Lawrence Edwards:** Resources. **Valdir F. Novello:** Writing – review & editing, Supervision. **Hubert Vonhof:** Writing – review & editing, Funding acquisition, Supervision. **Denis Scholz:** Writing – review & editing, Funding acquisition, Supervision.

Declaration of competing interest

The authors declare that they have no known competing financial interests or personal relationships that could have appeared to influence the work reported in this paper.

Data availability

The new $\delta^{18}O$, $\delta^{13}C$ and $^{87}Sr/^{86}Sr$ records from São Mateus cave will be available at PANGAEA.

Acknowledgements

We acknowledge financial support for this project from the Max Planck Graduate Center Mainz, the Deutsche Forschungsgemeinschaft through grant INST 247/889-1 FUGG to DS. We also acknowledge the support from Coordenação de Aperfeiçoamento de Pessoal de Nível Superior (CAPES) through the master's scholarship (process number 1715493) to C.F. Stumpf., Conselho Nacional de Desenvolvimento Científico e Tecnológico (CNPq) to R.V. Santos (grant 310641/2014-4) and FAPESP grants 2017/50085-3 to F.W.C and 2011/12238-6 to J.S.M. We would also like to thank Sr. Ramiro for the assistance in the field work.

3.9 References

Ampuero, A., Stríkis, N.M., Apaéstegui, J., Vuille, M., Novello, V.F., Espinoza, J.C., Cruz, F.W., Vonhof, H., Mayta, V.C., Martins, V.T.S., Cordeiro, R.C., Azevedo, V., Sifeddine, A., 2020. The Forest Effects on the Isotopic Composition of Rainfall in the Northwestern Amazon Basin. Journal of Geophysical Research: Atmospheres 125. https://doi.org/10.1029/2019JD031445

Assis, A.C.C. de, Coelho, R.M., Pinheiro, E.S. da, Durigan, G., 2011. Water availability determines physiognomic gradient in an area of low-fertility soils under Cerrado vegetation. Plant Ecology 212, 1135–1147. https://doi.org/10.1007/s11258-010-9893-8

Auler, A., Farrant, A.R., 1996. A brief introduction to karst and caves in Brazil. Proc. Univ. Bristol Splaeol.Soc. 20, 187–200.

Azevedo, V., Strikis, N.M., Novello, V.F., Roland, C.L., Cruz, F.W., Santos, R.V., Vuille, M., Utida, G., De Andrade, F.R.D., Cheng, H., Edwards, R.L., 2021. Paleovegetation seesaw in Brazil since the Late Pleistocene: A multiproxy study of two biomes. Earth and Planetary Science Letters 563, 116880–116880. https://doi.org/10.1016/j.epsl.2021.116880

Banner, J.L., Musgrove, M., Asmerom, Y., Lawrence Edwards, R., Hoff, J.A., 1996. High-resolution temporal record of Holocene ground-water chemistry: Tracing links between climate and hydrology. https://doi.org/10.1130/0091-7613(1996)024%253C1049:HRTROH%253E2.3.CO;2

Bao, Y., Liu, Z., He, C., 2023a. Dipole Response of Millennial Variability in Tropical South American Precipitation and d18Op during the Last Deglaciation. Part II: d18Op Response. Journal of Climate 36, 4709–4721. https://doi.org/10.1175/JCLI-D-22-0289.1

Bao, Y., Liu, Z., He, C., 2023b. Dipole Response of Millennial Variability in Tropical South American Precipitation and δ18Op during the Last Deglaciation. Part I: Rainfall Response. Journal of Climate 36, 4691–4707. https://doi.org/10.1175/JCLI-D-22-0172.1

Barberi, M., Salgado-Labouriau, M.L., Suguio, K., 2000. Paleovegetation and paleoclimate of "Vereda de Águas Emendadas'', central Brazil, Journal of South American Earth Sciences.

Behling, H., 2002. Late Quaternary vegetation and climate dynamics in southeastern Amazonia inferred from Lagoa da Confusão in Tocantins State, northern Brazil.

Bernal, J.P., Cruz, F.W., Stríkis, N.M., Wang, X., Deininger, M., Catunda, M.C.A., Ortega-Obregón, C., Cheng, H., Edwards, R.L., Auler, A.S., 2016. High-resolution Holocene South American monsoon history recorded by a speleothem from Botuverá Cave, Brazil. Earth and Planetary Science Letters 450, 186–196. https://doi.org/10.1016/j.epsl.2016.06.008

Bird, B.W., Abbott, M.B., Vuille, M., Rodbell, D.T., Stansell, N.D., Rosenmeier, M.F., 2011. A 2,300-year-long annually resolved record of the South American summer monsoon from the Peruvian Andes. Proceedings of the National Academy of Sciences of the United States of America 108, 8583–8588. https://doi.org/10.1073/pnas.1003719108

Bustamante, M., Nardoto, G.B., Jcf, Takahashi, F., Vieira, L., 2012. Potential impacts of climate change on biogeochemical functioning of Cerrado ecosystems, Braz. J. Biol.

Campos, J., Dardenne, M.A., 1997. ESTRATIGRAFIA E SEDIMENTAÇÃO DA BACIA SANFRANCISCANA: UMA REVISÃO.

Campos, J.L.P.S., Cruz, F.W., Ambrizzi, T., Deininger, M., Vuille, M., Novello, V.F., Strikis, N.M., 2019. Coherent South American Monsoon Variability During the Last Millennium Revealed Through High-Resolution Proxy Records. Geophysical Research Letters 46, 8261–8270. https://doi.org/10.1029/2019GL082513

Cassino, R.F., Ledru, M.P., Santos, R. de A., Favier, C., 2020. Vegetation and fire variability in the central Cerrados (Brazil) during the Pleistocene-Holocene transition was influenced by oscillations in the SASM boundary belt. Quaternary Science Reviews 232. https://doi.org/10.1016/j.quascirev.2020.106209

Cassino, R.F., Martinho, C.T., da Silva Caminha, S.A.F., 2018. A Late Quaternary palynological record of a palm swamp in the Cerrado of central Brazil interpreted using modern analog data. Palaeogeography, Palaeoclimatology, Palaeoecology 490, 1–16. https://doi.org/10.1016/j.palaeo.2017.08.036

Cheng, H., Lawrence Edwards, R., Shen, C.C., Polyak, V.J., Asmerom, Y., Woodhead, J., Hellstrom, J., Wang, Y., Kong, X., Spötl, C., Wang, X., Calvin Alexander, E., 2013a. Improvements in 230Th dating, 230Th and 234U half-life values, and U-Th isotopic measurements by multi-collector inductively coupled plasma mass spectrometry. Earth and Planetary Science Letters. https://doi.org/10.1016/j.epsl.2013.04.006

Cheng, H., Sinha, A., Cruz, F.W., Wang, X., Edwards, R.L., D'Horta, F.M., Ribas, C.C., Vuille, M., Stott, L.D., Auler, A.S., 2013b. Climate change patterns in Amazonia and biodiversity. Nature Communications 4, 1411–1411. https://doi.org/10.1038/ncomms2415

Cruz, F.W., Vuille, M., Burns, S.J., Wang, X., Cheng, H., Werner, M., Lawrence Edwards, R., Karmann, I., Auler, A.S., Nguyen, H., 2009. Orbitally driven east-west antiphasing of South American precipitation. Nature Geoscience 2, 210–214. https://doi.org/10.1038/ngeo444

Dardenne, M.A., 1978. Síntese sobre a estratigrafia do Grupo Bambuí no Brasil Central. Anais do XXX Congr. Bras. de Geol. Recife, 597–610.

Deininger, M., Ward, B.M., Novello, V.F., Cruz, F.W., 2019. Late quaternary variations in the south american monsoon system as inferred by speleothems—new perspectives using the SISAL database. Quaternary 2. https://doi.org/10.3390/quat2010006

Della Libera, M.E., Novello, V.F., Cruz, F.W., Orrison, R., Vuille, M., Maezumi, S.Y., de Souza, J., Cauhy, J., Campos, J.L.P.S., Ampuero, A., Utida, G., Stríkis, N.M., Stumpf, C.F., Azevedo, V., Zhang, H., Edwards, R.L., Cheng, H., 2022. Paleoclimatic and paleoenvironmental changes in Amazonian lowlands over the last three millennia. Quaternary Science Reviews 279, 107383–107383. https://doi.org/10.1016/J.QUASCIREV.2022.107383

Escobar-Torrez, K., Ledru, M.P., Cassino, R.F., Bianchini, P.R., Yokoyama, E., 2024. Long-and short-term vegetation change and inferred climate dynamics and anthropogenic activity in the central Cerrado during the Holocene. Journal of Quaternary Science 39, 130–144. https://doi.org/10.1002/jqs.3567

Fairchild, I.J., Baker, A., 2011. From Process to Past Environments, Speleothem Science.

Fohlmeister, J., Riavo G. Voarintsoa, N., Lechleitner, F.A., Boyd, M., Brandtstätter, S., Jacobson, M.J., Oster, J., 2020. Main Controls on the Stable Carbon Isotope Composition of Speleothems. Geochimica et Cosmochimica Acta. https://doi.org/10.1016/j.gca.2020.03.042

Fohlmeister, J., Scholz, D., Kromer, B., Mangini, A., 2011. Modelling carbon isotopes of carbonates in cave drip water. Geochimica et Cosmochimica Acta 75, 5219–5228. https://doi.org/10.1016/j.gca.2011.06.023

Frumkin, A., Stein, M., 2004. The Sahara-East Mediterranean dust and climate connection revealed by strontium and uranium isotopes in a Jerusalem speleothem. Earth and Planetary Science Letters 217, 451–464. https://doi.org/10.1016/S0012-821X(03)00589-2

Garreaud, R.D., Vuille, M., Compagnucci, R., Marengo, J., 2009. Present-day South American climate. Palaeogeography, Palaeoclimatology, Palaeoecology 281, 180–195. https://doi.org/10.1016/j.palaeo.2007.10.032

Goede, A., McCulloch, M., McDermott, F., Hawkesworth, C., 1998. Aeolian contribution to strontium and strontium isotope variations in a Tasmanian speleothem. Chemical Geology 149, 37–50. https://doi.org/10.1016/S0009-2541(98)00035-7

Gorenstein, I., Prado, L.F., Bianchini, P.R., Wainer, I., Griffiths, M.L., Pausata, F.S.R., Yokoyama, E., 2022. A fully calibrated and updated mid-Holocene climate reconstruction for Eastern South America. Quaternary Science Reviews 292. https://doi.org/10.1016/j.quascirev.2022.107646

Gouveia, S.E.M., Pessenda, L.C.R., Aravena, R., Boulet, R., Scheel-Ybert, R., Bendassoli, J.A., Ribeiro, A.S., Freitas, H.A., 2002. Carbon isotopes in charcoal and soils in studies of paleovegetation and climate changes during the late Pleistocene and the Holocene in the southeast and centerwest regions of Brazil. https://doi.org/10.1016/S0921-8181(02)00064-4

Hersbach, H., Bell, B., Berrisford, P., Hirahara, S., Horányi, A., Muñoz-Sabater, J., Nicolas, J., Peubey, C., Radu, R., Schepers, D., Simmons, A., Soci, C., Abdalla, S., Abellan, X., Balsamo, G., Bechtold, P., Biavati, G., Bidlot, J., Bonavita, M., De Chiara, G., Dahlgren, P., Dee, D., Diamantakis, M., Dragani, R., Flemming, J., Forbes, R., Fuentes, M., Geer, A., Haimberger, L., Healy, S., Hogan, R.J., Hólm, E., Janisková, M., Keeley, S., Laloyaux, P., Lopez, P., Lupu, C., Radnoti, G., de Rosnay, P., Rozum, I., Vamborg, F., Villaume, S., Thépaut, J.N., 2020. The ERA5 global reanalysis. Quarterly Journal of the Royal Meteorological Society 146, 1999–2049. https://doi.org/10.1002/qj.3803

Hofmann, G.S., Silva, R.C., Weber, E.J., Barbosa, A.A., Oliveira, L.F.B., Alves, R.J.V., Hasenack, H., Schossler, V., Aquino, F.E., Cardoso, M.F., 2023. Changes in atmospheric circulation and evapotranspiration are reducing rainfall in the Brazilian Cerrado. Scientific Reports 13. https://doi.org/10.1038/s41598-023-38174-x

Huffman, G.J., Bolvin, D.T., Joyce, R., Nelkin, E.J., Tan, J., Braithwaite, D., Hsu, K., Kelley, O.A., Nguyen, P., Sorooshian, S., Watters, D.C., West, B.J., Xie, P., 2023. Algorithm Theoretical Basis Document (ATBD) NASA Global Precipitation Measurement (GPM) Integrated Multi-satellitE Retrievals for GPM (IMERG) Version 07.

Hurley, J.V., Galewsky, J., Worden, J., Noone, D., 2012. A test of the advection-condensation model for subtropical water vapor using stable isotopologue observations from Mauna Loa Observatory, Hawaii. Journal of Geophysical Research Atmospheres 117. https://doi.org/10.1029/2012JD018029

Klink, C.A., Sato, M.N., Cordeiro, G.G., Ramos, M.I.M., 2020. The role of vegetation on the dynamics of water and fire in the cerrado ecosystems: Implications for management and conservation. Plants 9, 1–27. https://doi.org/10.3390/plants9121803

Lawrence Edwards, R., Chen, J.H., Wasserburg, G.J., 1987. 238U234U230Th232Th systematics and the precise measurement of time over the past 500,000 years. Earth and Planetary Science Letters 81, 175–192. https://doi.org/10.1016/0012-821X(87)90154-3

Ledru, M.-P., Braga, P.I.S., Soubiès, F., Fournier, M., Martin, L., Suguio, K., Turcq, B., 1996. The last 50,000 years in the Neotropics (Southern Brazil): evolution of vegetation and climate. Palaeogeography, Palaeoclimatology, Palaeoecology 123, 239–257. https://doi.org/10.1016/0031-0182(96)00105-8

Lenters, J.D., Cook, K.H., 1997. On the origin of the Bolivian high and related circulation features of the South American climate. Journal of the Atmospheric Sciences 54, 656–677.

Marengo, J.A., Liebmann, B., Grimm, A.M., Misra, V., Silva Dias, P.L., Cavalcanti, I.F.A., Carvalho, L.M.V., Berbery, E.H., Ambrizzi, T., Vera, C.S., Saulo, A.C., Nogues-Paegle, J., Zipser, E., Seth, A., Alves, L.M., 2012. Recent developments on the South American monsoon system. International Journal of Climatology 32, 1–21. https://doi.org/10.1002/joc.2254

McDermott, F., 2004. Palaeo-climate reconstruction from stable isotope variations in speleothems: A review. Quaternary Science Reviews 23, 901–918. https://doi.org/10.1016/j.quascirev.2003.06.021

Moquet, J.S., Cruz, F.W., Novello, V.F., Stríkis, N.M., Deininger, M., Karmann, I., Santos, R.V., Millo, C., Apaestegui, J., Guyot, J.L., Siffedine, A., Vuille, M., Cheng, H., Edwards, R.L., Santini, W., 2016. Calibration of speleothem δ18O records against hydroclimate instrumental records in Central Brazil. Global and Planetary Change 139, 151–164. https://doi.org/10.1016/j.gloplacha.2016.02.001

Musgrove, M.L., Banner, J.L., 2004. Controls on the spatial and temporal variability of vadose dripwater geochemistry: Edwards aquifer, central Texas. Geochimica et Cosmochimica Acta 68, 1007–1020. https://doi.org/10.1016/j.gca.2003.08.014

Novello, V.F., Cruz, F.W., McGlue, M.M., Wong, C.I., Ward, B.M., Vuille, M., Santos, R.A., Jaqueto, P., Pessenda, L.C.R., Atorre, T., Ribeiro, L.M.A.L., Karmann, I., Barreto, E.S., Cheng, H., Edwards, R.L., Paula, M.S., Scholz, D., 2019. Vegetation and environmental changes in tropical South America from the last glacial to the Holocene documented by multiple cave sediment proxies. Earth and Planetary Science Letters 524, 115717–115717. https://doi.org/10.1016/j.epsl.2019.115717

Novello, V.F., Cruz, F.W., Moquet, J.S., Vuille, M., de Paula, M.S., Nunes, D., Edwards, R.L., Cheng, H., Karmann, I., Utida, G., Stríkis, N.M., Campos, J.L.P.S., 2018. Two Millennia of South Atlantic Convergence Zone Variability Reconstructed From Isotopic Proxies. Geophysical Research Letters 45, 5045–5051. https://doi.org/10.1029/2017GL076838

Novello, V.F., William da Cruz, F., Vuille, M., Pereira Silveira Campos, J.L., Stríkis, N.M., Apaéstegui, J., Moquet, J.S., Azevedo, V., Ampuero, A., Utida, G., Wang, X., Paula-Santos, G.M., Jaqueto, P., Ruiz Pessenda, L.C., Breecker, D.O., Karmann, I., 2021. Investigating δ13C values in stalagmites from tropical South America for the last two millennia. Quaternary Science Reviews 255. https://doi.org/10.1016/j.quascirev.2021.106822

Oliveira, P.E.D., Magnólia, A., Barreto, F., Suguio, K., 1999. Late Pleistocene=Holocene climatic and vegetational history of the Brazilian caatinga: the fossil dunes of the middle São Francisco River, Palaeogeography, Palaeoclimatology, Palaeoecology.

Orrison, R., Vuille, M., Smerdon, J.E., Apaéstegui, J., Leandro S Campos, J.P., Cruz, F.W., Eduarda Della Libera, M., 2022. South American Monsoon variability over the last millennium in paleoclimate records and isotope-enabled climate models. Climate of the Past. https://doi.org/10.5194/cp-2022-6

Pessenda, L.C.R., Gouveia, S.E.M., Ribeiro, A. de S., De Oliveira, P.E., Aravena, R., 2010. Late Pleistocene and Holocene vegetation changes in northeastern Brazil determined from carbon isotopes and charcoal records in soils. Palaeogeography, Palaeoclimatology, Palaeoecology 297, 597–608. https://doi.org/10.1016/j.palaeo.2010.09.008

Rodwell, M.J., Hoskins, B.J., 2001. Subtropical Anticyclones and Summer Monsoons. https://doi.org/10.1175/1520-0442(2001)014%253C3192:SAASM%253E2.0.CO;2

Roland, C.L., 2018. Utilização de análises isotópicas multiproxy (87Sr/86Sr, δ234U, δ13C, δ18O) na reconstrução paleoclimática e paleoambiental do centro-leste do Brasil, norte de Minas Gerais. Universidade Federal Fluminense.

Rolph, G., Stein, A., Stunder, B., 2017. Real-time Environmental Applications and Display sYstem: READY. Environmental Modelling and Software 95, 210–228. https://doi.org/10.1016/j.envsoft.2017.06.025

Sabino, S.M.L., Cassino, R.F., Gomes, M.O.S., Sant'anna, E.M.E., Rocha Augustin, C.H.R., De Oliveira, D.A., 2021. Late Holocene in central Brazil: vegetation changes and humidity variability in a tropical wetland. Journal of Quaternary Science 36, 1028–1039. https://doi.org/10.1002/jqs.3351

Salgado-Labouriau, M.L., Casseti, V., Ferraz-Vicentini, K.R., Martin, L., Soubi~s, F., Suguio, K., Turcq, B., 1997. Late Quaternary vegetational and climatic changes in cerrado and palm swamp from Central Brazil (No. 00310182/97), Palaeogeography, Palaeoclimatology, Palaeoecology.

Scholz, D., Hoffmann, D.L., 2011. StalAge - An algorithm designed for construction of speleothem age models. Quaternary Geochronology 6, 369–382. https://doi.org/10.1016/j.quageo.2011.02.002

Secretaria de Meio Ambiente e Desenvolvimento Sustentável, G. do E. de G., STCP Engenharia de Projetos Ltda, 2016. PLANO DE MANEJO ESPELEOLOGICO - GOVERNO DO ESTADO DE GOIÁS - PARQUE ESTADUAL DE TERRA RONCA.

Smith, R.J., Mayle, F.E., 2018. Impact of mid- to late Holocene precipitation changes on vegetation across lowland tropical South America: A paleo-data synthesis. Quaternary Research (United States) 89, 134–155. https://doi.org/10.1017/qua.2017.89

Stein, A.F., Draxler, R.R., Rolph, G.D., Stunder, B.J.B., Cohen, M.D., Ngan, F., 2015. Noaa's hysplit atmospheric transport and dispersion modeling system. Bulletin of the American Meteorological Society 96, 2059–2077. https://doi.org/10.1175/BAMS-D-14-00110.1

Stríkis, N.M., Chiessi, C.M., Cruz, F.W., Vuille, M., Cheng, H., De Souza Barreto, E.A., Mollenhauer, G., Kasten, S., Karmann, I., Edwards, R.L., Bernal, J.P., Sales, H.D.R., 2015. Timing and structure of Mega-SACZ events during Heinrich Stadial 1. Geophysical Research Letters 42, 5477. https://doi.org/10.1002/2015GL064048

Strikis, N.M., Cruz, F.W., Cheng, H., Karmann, I., Edwards, R.L., Vuille, M., Wang, X., De Paula, M.S., Novello, V.F., Auler, A.S., 2011. Abrupt variations in South American monsoon rainfall during the Holocene based on a speleothem record from central-eastern Brazil. Geology 39, 1075–1078. https://doi.org/10.1130/G32098.1

Sulca, J., Vuille, M., Silva, Y., Takahashi, K., 2016. Teleconnections between the peruvian central andes and northeast Brazil during extreme rainfall events in austral summer. Journal of Hydrometeorology 17, 499–515. https://doi.org/10.1175/JHM-D-15-0034.1

Terra, M. de C.N.S., Santos, R.M.D., Prado Júnior, J.A.D., De Mello, J.M., Scolforo, J.R.S., Fontes, M.A.L., Schiavini, I., Dos Reis, A.A., Bueno, I.T., Magnago, L.F.S., Ter Steege, H., 2018. Water availability drives gradients of tree diversity, structure and functional traits in the Atlantic-Cerrado-Caatinga transition, Brazil. Journal of Plant Ecology 11, 803–814. https://doi.org/10.1093/jpe/rty017

Torfstein, A., Goldstein, S.L., Stein, M., 2018. Enhanced Saharan dust input to the Levant during Heinrich stadials. Quaternary Science Reviews 186, 142–155. https://doi.org/10.1016/j.quascirev.2018.01.018

Utida, G., Cruz, F.W., Santos, R.V., Sawakuchi, A.O., Wang, H., Pessenda, L.C.R., Novello, V.F., Vuille, M., Strauss, A.M., Borella, A.C., Stríkis, N.M., Guedes, C.C.F., Dias De Andrade, F.R., Zhang, H., Cheng, H., Edwards, R.L., 2020. Climate changes in Northeastern Brazil from deglacial to Meghalayan periods and related environmental impacts. Quaternary Science Reviews 250. https://doi.org/10.1016/j.quascirev.2020.106655

van Breukelen, M.R., Vonhof, H.B., Hellstrom, J.C., Wester, W.C.G., Kroon, D., 2008. Fossil dripwater in stalagmites reveals Holocene temperature and rainfall variation in Amazonia. Earth and Planetary Science Letters 275, 54–60. https://doi.org/10.1016/j.epsl.2008.07.060

Vuille, M., Burns, S.J., Taylor, B.L., Cruz, F.W., Bird, B.W., Abbott, M.B., Kanner, L.C., Cheng, H., Novello, V.F., 2012. A review of the South American monsoon history as recorded in stable isotopic proxies over the past two millennia. Climate of the Past 8, 1309–1321. https://doi.org/10.5194/cp-8-1309-2012

Wang, J., Yang, B., Ljungqvist, F.C., Luterbacher, J., Osborn, T.J., Briffa, K.R., Zorita, E., 2017. Internal and external forcing of multidecadal Atlantic climate variability over the past 1,200 years. Nature Geoscience 10, 512–517. https://doi.org/10.1038/ngeo2962

Wang, X., Auler, A.S., Edwards, R.L., Cheng, H., Ito, E., Wang, Y., Kong, X., Solheid, M., 2007. Millennial-scale precipitation changes in southern Brazil over the past 90,000 years. Geophysical Research Letters 34. https://doi.org/10.1029/2007GL031149

Ward, B.M., Wong, C.I., Novello, V.F., McGee, D., Santos, R.V., Silva, L.C.R., Cruz, F.W., Wang, X., Edwards, R.L., Cheng, H., 2019. Reconstruction of Holocene coupling between the South America Monsoon System and local moisture variability from speleothem δ 18 O and 87 Sr/ 86 Sr records. Quaternary Science Reviews 210, 51–63. https://doi.org/10.1016/j.quascirev.2019.02.019

Weber, M., Lugli, F., Jochum, K.P., Cipriani, A., Scholz, D., 2018. Calcium Carbonate and Phosphate Reference Materials for Monitoring Bulk and Microanalytical Determination of Sr Isotopes. Geostandards and Geoanalytical Research 42, 77–89. https://doi.org/10.1111/ggr.12191

Weber, M., Tacail, T., Lugli, F., Clauss, M., Weber, K., Leichliter, J., Winkler, D.E., Mertz-Kraus, R., Tütken, T., 2020. Strontium Uptake and Intra-Population 87Sr/86Sr Variability of Bones and Teeth—Controlled Feeding Experiments With Rodents (Rattus norvegicus, Cavia porcellus). Frontiers in Ecology and Evolution 8. https://doi.org/10.3389/fevo.2020.569940

Wolf, A., Ersek, V., Braun, T., French, A.D., McGee, D., Bernasconi, S.M., Skiba, V., Griffiths, M.L., Johnson, K.R., Fohlmeister, J., Breitenbach, S.F.M., Pausata, F.S.R., Tabor, C.R., Longman, J., Roberts, W.H.G., Chandan, D., Peltier, W.R., Salzmann, U., Limbert, D., Trinh, H.Q., Trinh, A.D., 2023. Deciphering local and regional hydroclimate resolves contradicting evidence on the Asian monsoon evolution. Nature Communications 14. https://doi.org/10.1038/s41467-023-41373-9

Wong, M.L., Battisti, D.S., Liu, X., Ding, Q., Wang, X., 2023. A North–South Dipole Response of the South Atlantic Convergence Zone During the Mid-Holocene. Geophysical Research Letters 50, e2023GL105130. https://doi.org/10.1029/2023GL105130

Wong, M.L., Wang, X., Latrubesse, E.M., He, S., Bayer, M., 2021. Variations in the South Atlantic Convergence Zone over the mid-to-late Holocene inferred from speleothem δ18O in central Brazil. Quaternary Science Reviews 270. https://doi.org/10.1016/j.quascirev.2021.107178

Wortham, B.E., Wong, C.I., Silva, L.C.R., McGee, D., Montañez, I.P., Troy Rasbury, E., Cooper, K.M., Sharp, W.D., Glessner, J.J.G., Santos, R.V., 2017. Assessing response of local moisture conditions in central Brazil to variability in regional monsoon intensity using speleothem 87Sr/86Sr values. Earth and Planetary Science Letters 463, 310–322. https://doi.org/10.1016/j.epsl.2017.01.034

Zilli, M.T., Carvalho, L.M.V., Lintner, B.R., 2019. The poleward shift of South Atlantic Convergence Zone in recent decades. Climate Dynamics 52, 2545–2563. https://doi.org/10.1007/s00382-018-4277-1

3.10 Supplementary Material I

Speleothem-based reconstruction of Holocene changes in monsoonal patterns and environmental conditions in central Brazil

3.10.1 Supplementary Text

Supplementary text 3.1

For the solution analyses, calcium carbonate powder (5 – 10 mg) was drilled with a manual hand drill machine, with approximately 2 cm spacing, collecting 14 samples along the central axis of the stalagmite. Two samples of host rock were drilled following the same procedure. Two soil samples were collected above the cave, close to its entrance: one from the surface after removing organic tree litter, and a second from approximately 30 cm below the surface. The samples were manually cleaned from organic parts, such as roots and sticks, by hand picking, then dried at 100°C in a stove and further macerated in a porcelain mortar. Rock and soil samples were analyzed by Thermal Ionization Mass Spectrometry (TIMS) using a Finnigan MAT-262, whereas speleothem samples were analyzed using a Neptune MC-ICP-MS (Thermo Fisher Scientific), all analysis performed at Geochronology Laboratory of University of Brasilia. All data were calibrated against NIST SRM987, which has a certified nominal value of 0.71034 ±0.00026, and presented a mean of 0.71029 ±0.00001 (n = 6) during the period of analyses (Supp. Table 2).

The low-resolution $^{87}Sr/^{86}Sr$ record of SMT16 obtained by solution analysis was further complemented by in-situ laser ablation analysis of Sr isotopes. For in-situ analysis of Sr isotopes, a Neptune Plus MC-ICP-MS was coupled with an ArF Excimer 193 nm laser ablation system at the Institute for Geosciences, Johannes Gutenberg University Mainz, Germany, following the methods described in Weber *et al.* (2017). Nitrogen was introduced into the sample gas line using an Apex Omega HF desolvator system. Data acquisition was performed as a line scan of 500 µm length perpendicular to the growth axis, a transition rate of 5 µm/s, a pulse repetition rate of 20 Hz and a spot size of 150 µm, resulting in a fluence of 5 J/cm^2. Accuracy was monitored using NanoSr ($^{87}Sr/^{86}Sr = 0.70753 \pm 0.00003$, 1 SD, n = 21), JCp-1 (0.70917 ± 0.00001, 1 SD, n = 12) and JCt-1 (0.70915 ± 0.00001, 1 SD, n = 18), which all agree with the literature value (Weber *et al.*, 2018; Weber *et al.*, 2020). Sampling was made along the main axis with approximately 5 mm spacing, yielding a total of 87 analyses.

Supplementary text 3.2

In contrast with the strong positive correlation between the $\delta^{13}C$ values and $^{87}Sr/^{86}Sr$ (r = 0.7, p< 0.01), the Sr isotope ratios and the $\delta^{18}O$ record only show a moderate negative correlation (r = -0.4, p< 0.01) (Supp. Fig. 4,). This suggests that the processes involving water-rock interaction time with the limestone bedrock (see section 5) might not be the main source of $^{87}Sr/^{86}Sr$ variability during the Holocene. Yet, since the SMT16 Sr isotope ratios are generally much lower than those of the soil, it indicates that the percolating water indeed captures the signal of the limestone bedrock. However, the processes described above obviously superimpose this signal that would typically result in the negative $\delta^{18}O$ vs. $^{87}Sr/^{86}Sr$ correlation.

3.10.2 Supplementary Tables

Supplementary Table 3.1 – Analytical details of $^{87}Sr/^{86}Sr$ isotope ratio analyses

Instrument/ Method	**Sample Type**	**Preparation/Collection**	**Analytical Details**	**Calibration/Standards**
Neptune MC-ICP-MS	Speleothem (solution)	5–10 mg calcium carbonate powder drilled along central axis (2 cm spacing, 15 samples in total).	Solution adjusted to 5% HNO_3 for analysis using spray-chamber nebulizer. Measurements normalized to NIST SRM987.	NIST SRM987 ($^{87}Sr/^{86}Sr$: 0.71034 ± 0.00026); Lab value: 0.71029 ± 0.00001 (n=6).
TIMS (MAT-262)	Host rock, soil	Host rock: 2 samples drilled similarly to speleothem. Soil: 2 samples collected above cave, cleaned, dried, macerated.	Samples solubilized in 5% HNO_3 for precipitation on filament.	NIST SRM987 ($^{87}Sr/^{86}Sr$: 0.71034 ± 0.00026).
Neptune Plus MC-ICP-MS + LA	Speleothem (laser ablation)	In situ analysis, sampling along growth axis (5 mm spacing, 87 analyses). 500 µm-long line scan, 5µm/s transition rate.	Coupled with ArF Excimer 193 nm laser ablation system. Spot size: 150 µm, fluence: 5 J/cm², 20 Hz pulse repetition rate.	NanoSr ($^{87}Sr/^{86}Sr$: 0.70753 ± 0.00003); JCp-1 ($^{87}Sr/^{86}Sr$: 0.70917 ± 0.00001); JCt-1 ($^{87}Sr/^{86}Sr$: 0.70915 ± 0.00001).

Supplementary Table 3.2 – Values of NIST 987 obtained during analysis.

Measured values of NIST 987 during measurement			
#	lab run	value	error
5	NBS 987_1	0.71028	0.00001
6	NBS 987_2	0.71030	0.00001
8	NBS 987_1	0.71030	0.00001
9	NBS 987_2	0.71030	0.00001
13	NBS 987_1	0.71028	0.00001
14	NBS 987_2	0.71030	0.00001

Supplementary Table 3.3 - SMT16 ^{230}Th-U ages. Ages indicted with a „ ' ” were measured at the Geochronology Laboratory at the University of Minnesota (USA); the ages without were measured at the Institute of Global Environmental Change, Xi'an Jiaotong University (China).

Distance from the top (mm)	Sample Number	^{238}U (ppb)	^{232}Th (ppt)	^{230}Th / ^{232}Th (atomic x10-6)	δ^{234}U* (measured)	^{230}Th / ^{238}U (activity)	^{230}Th Age (yr) (uncorrected)	^{230}Th Age (yr) (corrected)	$\delta^{234}U_{Initial}$** (corrected)	230Th Age (yr BP)*** (corrected)
3	SMT16-2’	1941.1 ±6.2	1849 ±39	22 ±5	118.6 ±2.8	0.001295 ±0.0003	126 ±30	**102 ±35**	119 ±3	**40 ±35**
24	SMT16-23’	1519.5 ±5.0	413 ±18	378 ±43	120.9 ±2.8	0.006239 ±0.0007	609 ±65	**601 ±65**	121 ±3	**539 ±65**
46	SMT16-47’	1799.6 ±6.2	65 ±14	4996 ±1089	124.1 ±3.1	0.010999 ±0.0005	1072 ±50	**1071 ±50**	124 ±3	**1009 ±50**
73	SMT16-72’	2058.5 ±6.1	112 ±8	5489 ±425	114.7 ±2.6	0.0181 ±0.0004	1789 ±41	**1787 ±41**	115 ±3	**1725 ±41**
87	SMT16-96	3027.0 ±9	341 ±7	3331 ±68	131.6 ±2.0	0.0228 ±0.0001	2215 ±8	**2212 ±9**	132 ±2.0	**2144 ±9**
114	SMT16-114’	1631.3 ±4.4	126 ±8	6199 ±396	139.6 ±2.3	0.029028 ±0.0004	2812 ±40	**2810 ±40**	141 ±2	**2748 ±40**
133	SMT16-133	3073.0 ±8	248 ±5	6660 ±139	144.1 ±1.9	0.0325 ±0.0001	3145 ±11	**3143 ±11**	145 ±1.9	**3075 ±11**
155	SMT16-155’	1820.7 ±4.5	100 ±7	11282.6 ±785.1	144.2 ±2.3	0.037582691 ±0.00036	3640 ±37	**3638 ±37**	145.7 ±2.3	**3576 ±36.7**
186	SMT16-186	2308.0 ±5	264 ±5	6470.0 ±133	144.9 ±1.7	0.04488 ±0.0001	4357 ±13	**4354 ±13**	147.0 ±1.7	**4286 ±13**
216	SMT16-215	2317.0 ±4	283 ±6	7127.0 ±147	140.9 ±1.6	0.05272 ±0.0001	5154 ±15	**5151 ±15**	143.0 ±1.7	**5083 ±15**
242	SMT16-242	2308.0 ±4	70 ±2	33165.0 ±958	129.9 ±1.5	0.06068 ±0.0001	6014 ±16	**6013 ±16**	132.0 ±1.5	**5945 ±16**
264	SMT16-264’	1784.5 ±5.6	233 ±11	8448.7 ±417.3	129.0 ±2.7	0.067026896 ±0.00057	6666 ±61	**6663 ±61**	131.5 ±2.8	**6601 ±60.7**
291	SMT16-290	2437.0 ±4	1283 ±26	2374.0 ±48	139.4 ±1.6	0.07578 ±0.0002	7495 ±20	**7482 ±22**	142.0 ±1.6	**7414 ±22**
322	SMT16-321	2286.0 ±3	38 ±2	83244.0 ±4681	134.4 ±1.5	0.08493 ±0.0002	8473 ±22	**8473 ±22**	138.0 ±1.5	**8405 ±22**
347	SMT16-346	2532.0 ±5	39 ±1	99136.0 ±3571	128.5 ±1.7	0.09167 ±0.0002	9225 ±26	**9224 ±26**	132.0 ±1.7	**9150 6±26**
370	SMT16-368’	1160 ±4	64 ±12	29446.3 ±5718.0	124.9 ±2.9	0.0981 ±0.0010	9932 ±113	**9930 ±113**	128 ±3	**9868 ±113**
377	SMT16-378	983 ±1	12614 ±253	130.0 ±3	123.2 ±1.3	0.1015 ±0.0008	10307 ±85	**9975 ±250**	127 ±1.3	**9907 ±250**
404	SMT16-408	1007 ±1	183 ±4	9866.0 ±211	110.7 ±1.6	0.1085 ±0.0002	11194 ±30	**11189 ±30**	114 ±1.7	**11121 ±30**

U decay constants: $l_{238} = 1.55125x10^{-10}$ (Jaffey et al., 1971) and $l_{234} = 2.82206x10^{-6}$ (Cheng et al., 2013). Th decay constant: $l_{230} = 9.1705x10^{-6}$ (Cheng et al., 2013).

$*d^{234}U = ([^{234}U/^{238}U]_{activity} - 1)x1000$. ** $d^{234}U_{initial}$ was calculated based on ^{230}Th age (T), i.e., $d^{234}U_{initial} = d^{234}U_{measured}$ x e^{l234xT}.

Corrected ^{230}Th ages assume the initial $^{230}Th/^{232}Th$ atomic ratio of $4.4 \pm 2.2 x10^{-6}$. Those are the values for a material at secular equilibrium, with the bulk earth $^{232}Th/^{238}U$ value of 3.8. The errors are arbitrarily assumed to be 50%.

***B.P. stands for “Before Present” where the “Present” is defined as the year 1950 A.D.

3.10.3 Supplementary Figures

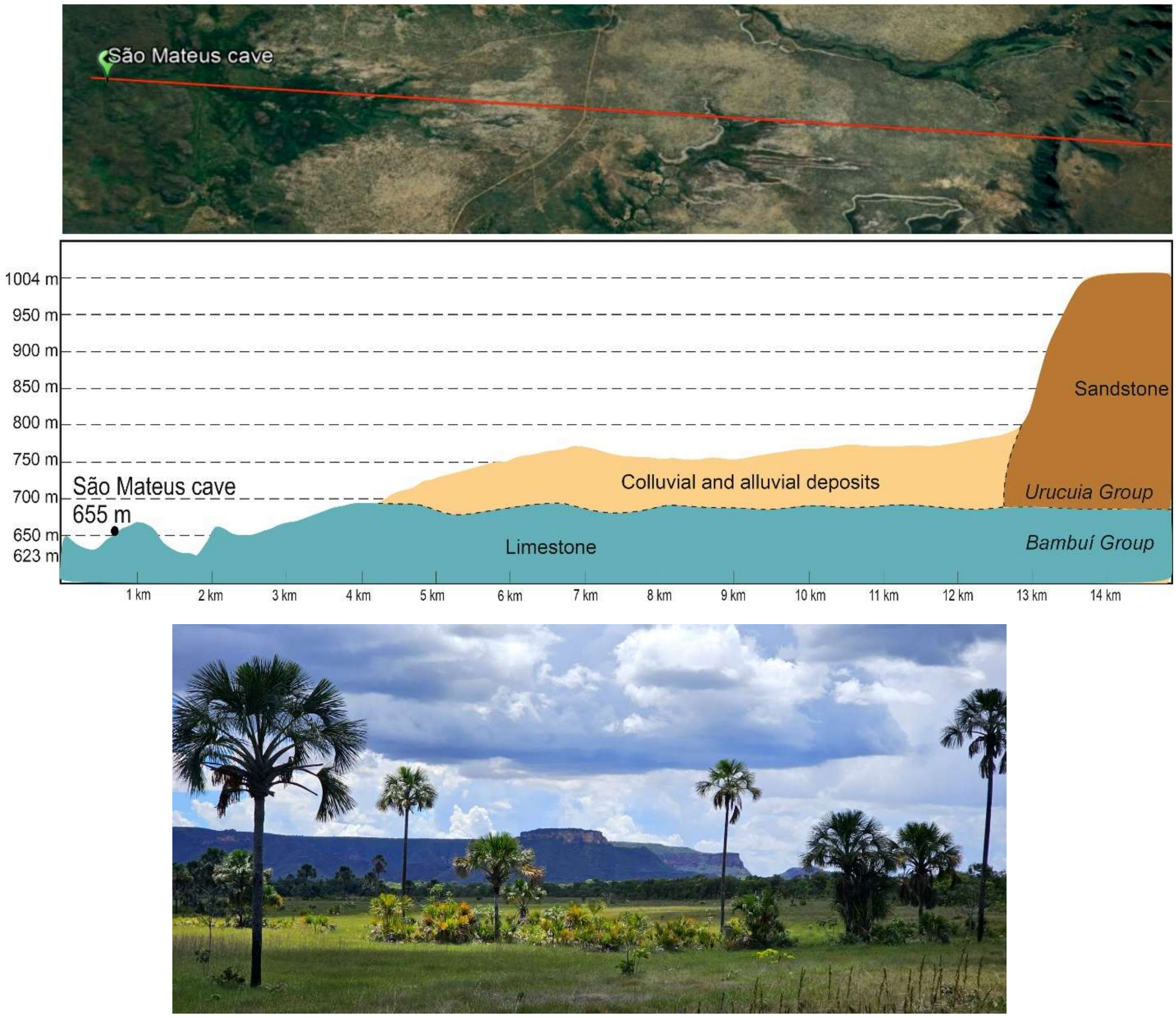

Supplementary Figure 3.1 – (top) Satellite image of São Mateus cave region, with transect line (red line) from the cave to Urucuia Group. Elevation profile of the transect with schematic geological context. In blue is represented the Bambuí group, the limestone unit; in brown the Urucuia group, sandstone unit; in yellow are represented the colluvial and alluvial deposits. The dashed lines represent the inferred contact between each unit. The black dot is the cave location. (bottom) View of the Urucuia Plateau.

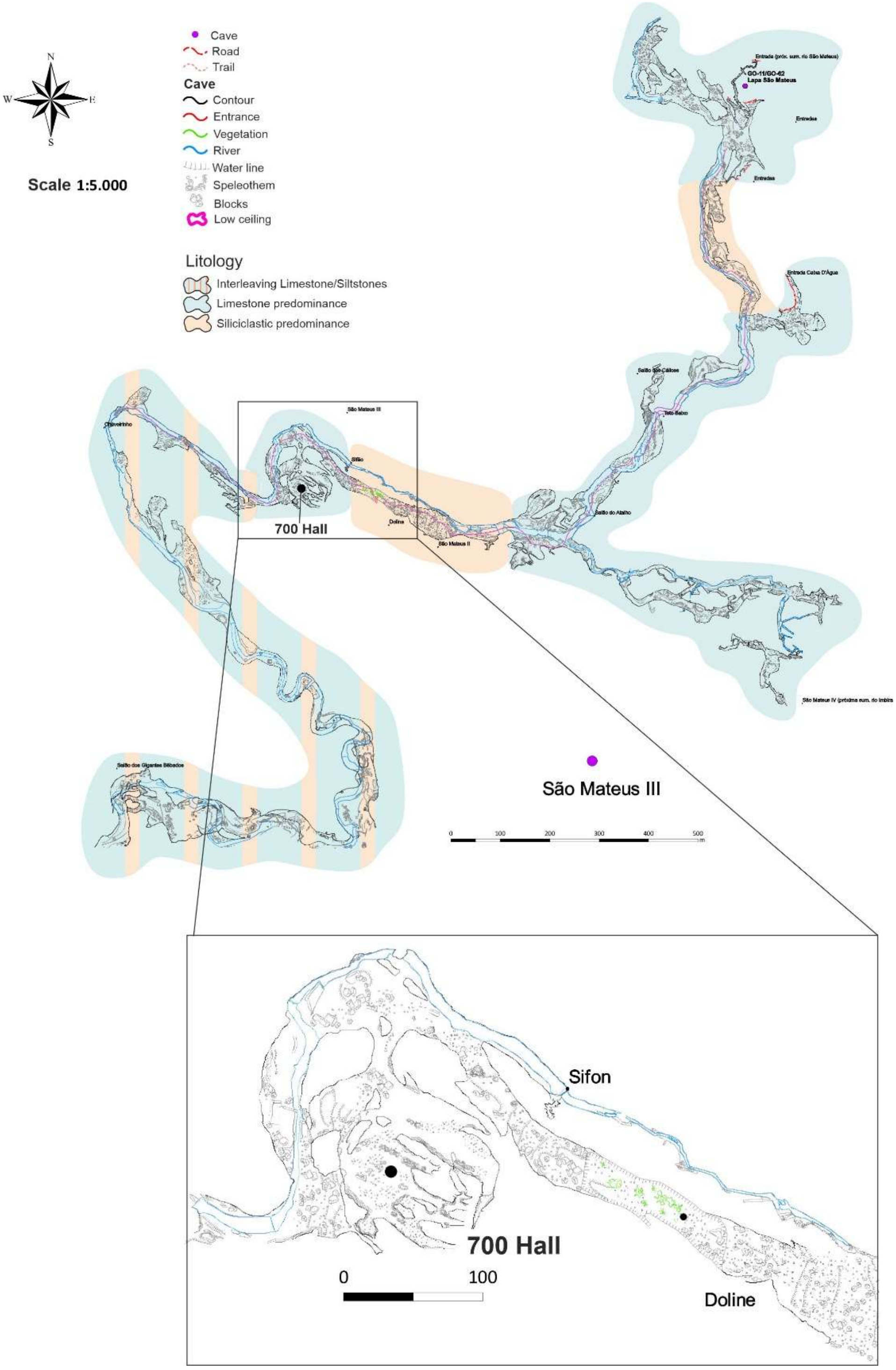

Supplementary Figure 3.2 - Adapted partial map of the geological characterization of São Mateus cave system obtained from the Speleological Management Plan of PETER. The white stretch represents the cave passages. The different colors and patterns around the cave passages indicate the predominant bedrock around each area of the cave. This is a zoomed in look at the 700 Hall, where SMT16 was collected. The original map in which was based this image, was the first official map of the cave, produced by CEU (Centro Excursionista Universitário) in the 70's (CEU, 1979), and totalize more than 10 km of cave length.

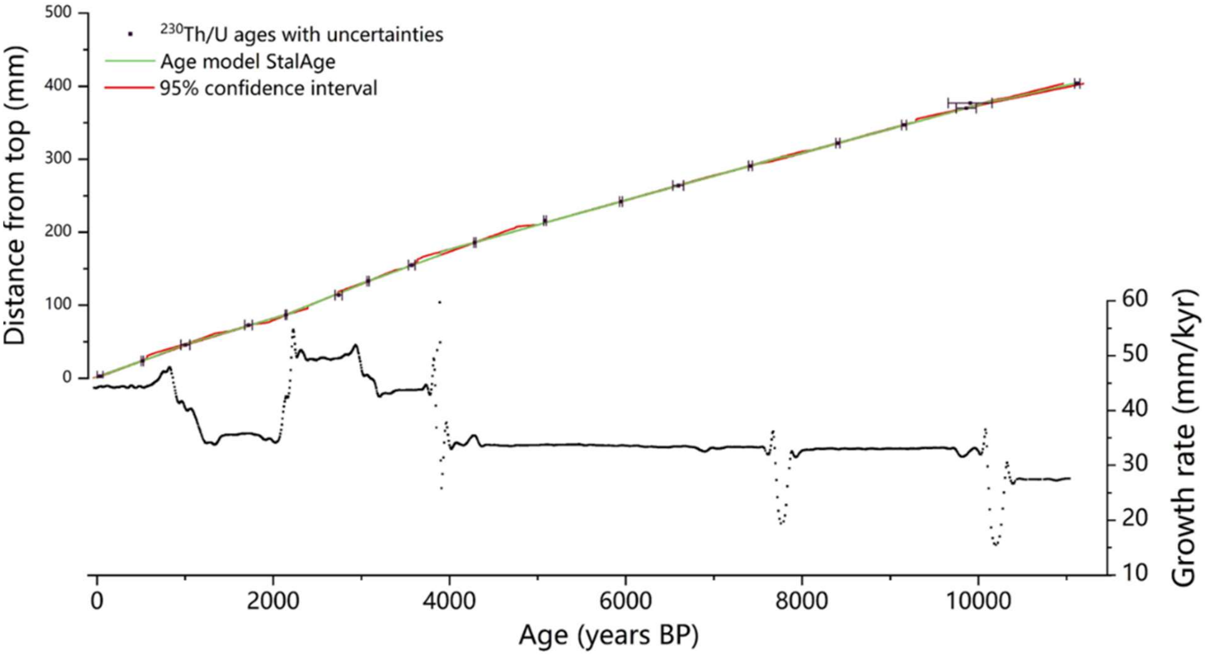

Supplementary Figure 3.3 – (top) Age-depth relationship for the SMT16 stalagmite. Black points represent the MC-ICP-MS ^{230}Th-U ages with the corresponding error bars, the green line represents the age-model calculated by StalAge (Scholz and Hoffmann, 2011), and the red lines show the corresponding age-uncertainties (95% confidence interval). (bottom) Growth rate of SMT16.

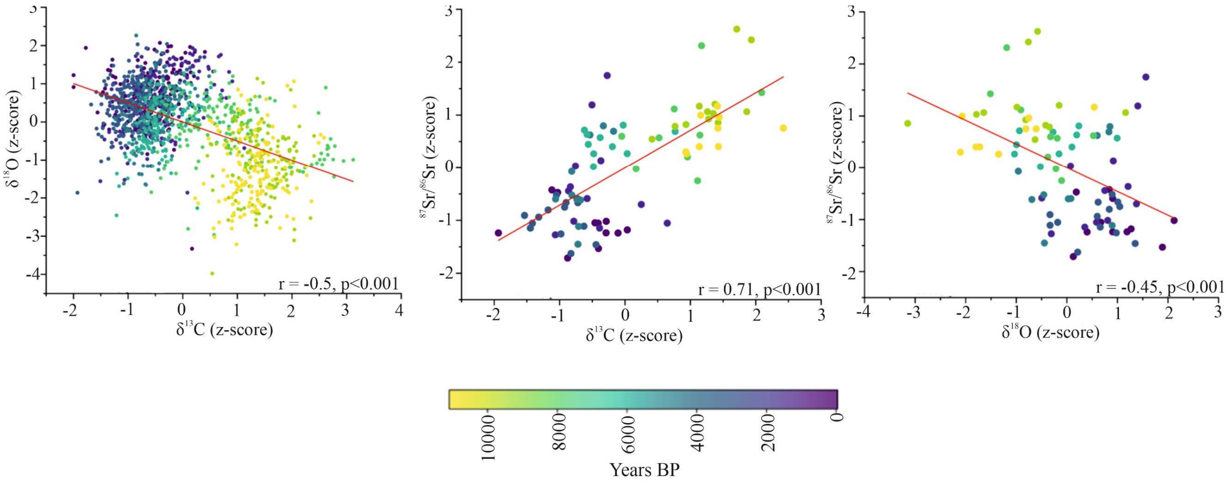

Supplementary Figure 3.4 – Depth-based correlations between the SMT16 ^{87}Sr/^{86}Sr, δ^{18}O and δ^{13}C records. Cross plots respectively, from left to right, of δ^{18}O vs. δ^{13}C, δ^{13}C vs. ^{87}Sr/^{86}Sr, and ^{87}Sr/^{86}Sr vs. δ^{18}O with their linear fit (red line). Color-scale showing year distribution between the records.

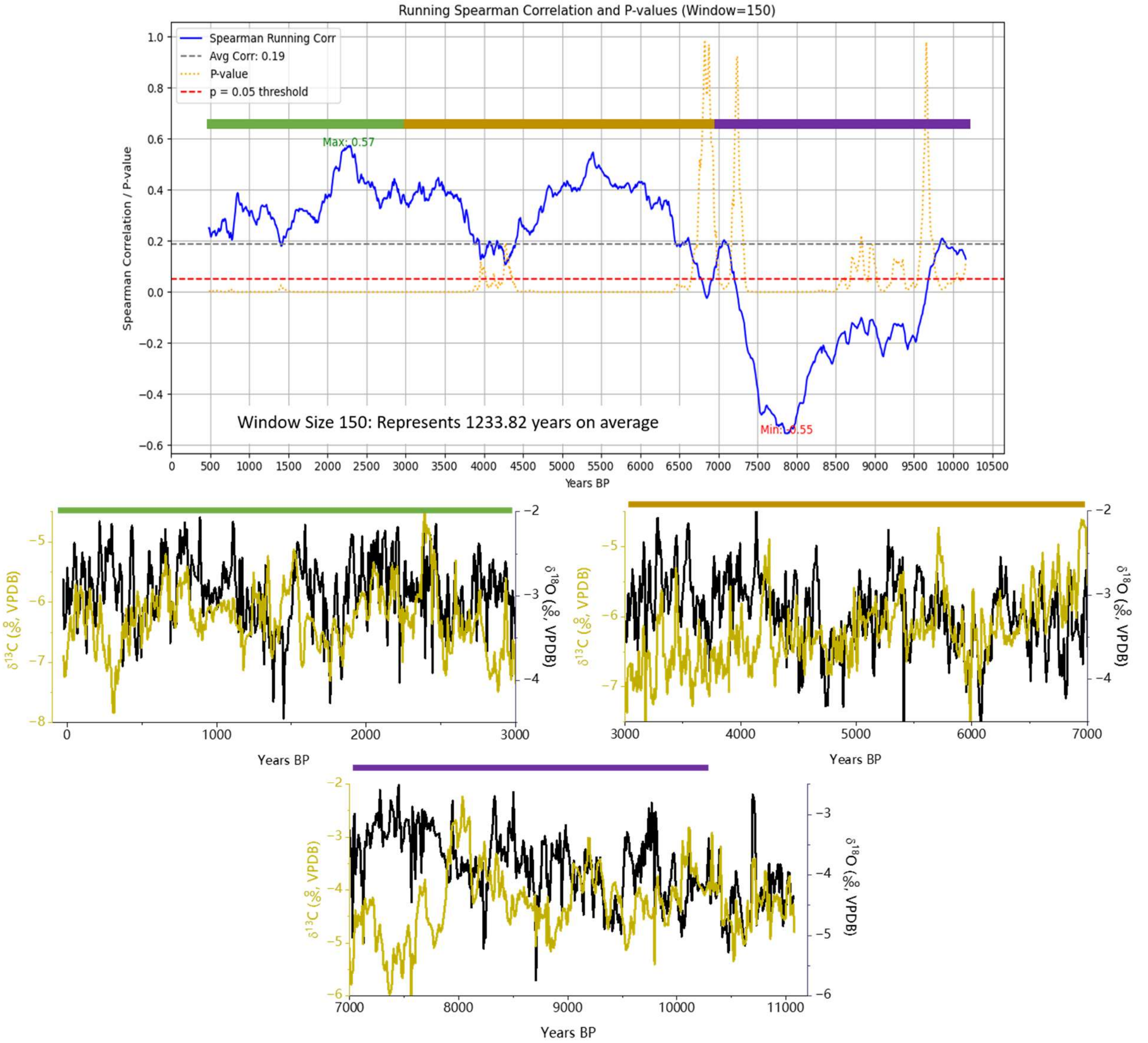

Supplementary Figure 3.5 – (a) Spearman running correlation analysis between SMT16 $\delta^{18}O$ and $\delta^{13}C$ records with a window size of 150 points, resulting on ~1233-year bins. The green, orange and purple bars on top of the correlation curve indicate the corresponding periods of (b) the zoomed-in comparison between $\delta^{18}O$ and $\delta^{13}C$ records.

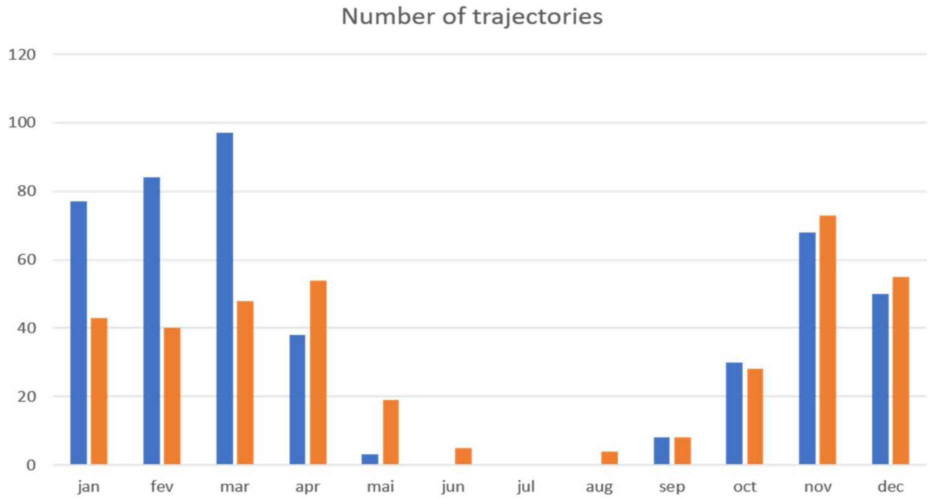

Supplementary Figure 3.6 – Contribution of trajectories from clusters East (blue) and North-east (orange) throughout the year.

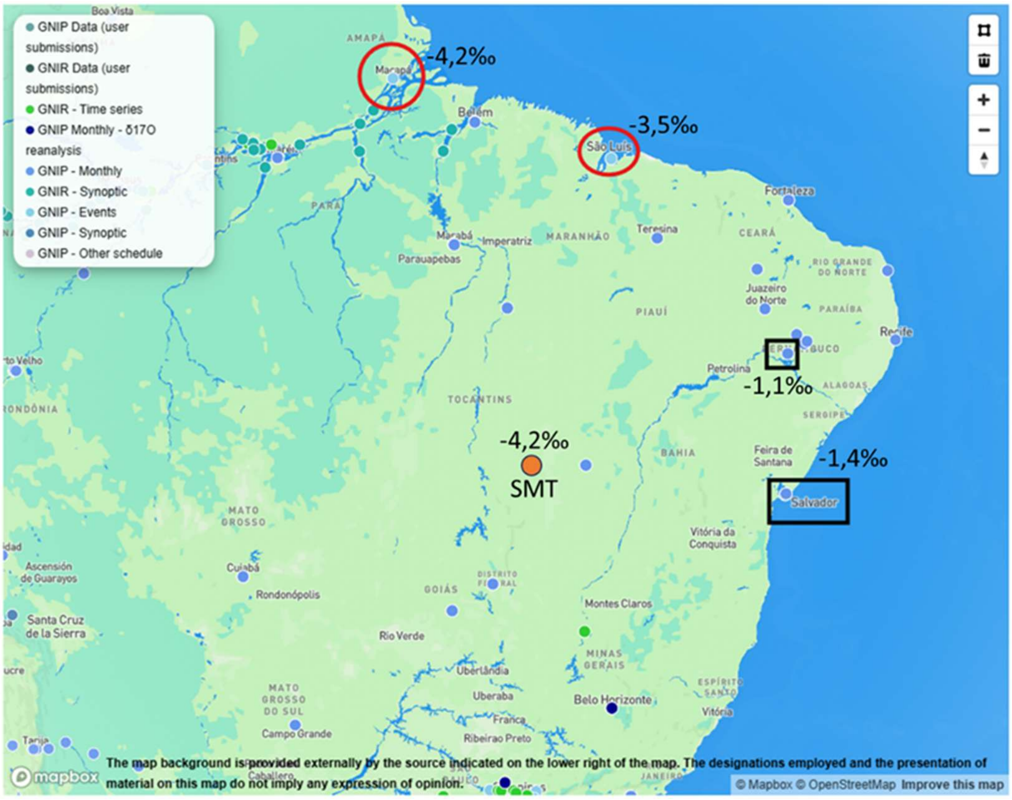

Supplementary Figure 3.7 – Mean rainfall δ^{18}O values based on the entire observation period available Global Network of Isotopes in Precipitation (GNIP) data from two stations where the trajectories go through the north-eastern pathway (Macapá and Sao Luis – red circles), and with two other stations that go through the eastern pathway (Pernambuco and Salvador – black squares).

Chapter 4 – Manuscript II

Overprinted forcing of millennial events during the last deglaciation period in tropical South America

Marcela Eduarda Della Libera[a,b]*; Julio Cauhy [a,b]; Valdir F. Novello[c]; Cintia Stumpf [c]; Roberto V. Santos[c]; Francisco W. Cruz Junior[d]; Nicolas M. Strikis[d]; Jean-Sebastian Moquet[f]; Michael Weber [a]; Hai Cheng [g]; Hubert Vonhof[b]; Denis Scholz[a]

[a] Institut für Geowissenschaften, Johannes Gutenberg-Universität Mainz, Germany
[b] Max Planck Institut für Chemie, Mainz, Germany
[c] Institute of Geosciences, University of Brasília, Brasília – DF, Brazil
[d] Instituto de Geociências, Universidade de São Paulo, São Paulo-SP, Brazil
[f] Institut des Sciences de la Terre d'Orléans (ISTO), Univ Orléans - Orléans, France
[g] Institute of Global Environmental Change, Xi'an Jiaotong University, Shaanxi, China
*Corresponding author:
Marcela E. Della Libera
Email: dellalibera.me@gmail.com

Paper in preparation-a

4.1 Abstract

Rapid and abrupt climate changes characterize the last deglaciation period, mostly driven by shifts in Northen Hemisphere (NH) temperatures and the inter-hemispheric heat distribution via the Atlantic meridional overturning circulation (AMOC). Among these events, the Bølling–Allerød (BA) interstadial stands out as one of the most significant events due to a pronounced warming in the NH. Particularly in South America, the BA remains relatively understudied in comparison with its predecessor (Heinrich Stadial 1) and successor (Younger Dryas) events. Here we present two new high-resolution $\delta^{18}O$ speleothem records from central-eastern and western Brazil, providing better comprehension of hydroclimate variability during the deglacial period, with a focus on the BA event. To place these records in a broader context, we bring a compilation of paleoclimate datasets across South America to assess the structure and spatial pattern of this event. Although South America exhibits a well-documented precipitation dipole on multiple timescales, our compilation reveals that this pattern weakens or disappears during the HS1–BA–YD sequence, and particularly during the BA. Moreover, we show how NH high-latitude abrupt climatic shifts can have a continent-wide response in tropical South America. Finally, our results offer a more comprehensive perspective on continental-scale climate dynamics during one of the most critical intervals of the last deglaciation.

4.2 Introduction

During the last deglaciation (~21-11.7 kyr BP), one of the most abrupt warm intervals recorded in Greenland ice cores is the Greenland Interstadial 1 (GI-1; 14.7–12.9 kyr BP) (Rasmussen *et al.*, 2014; Thiagarajan *et al.*, 2014). This interval, also known as the Bølling–Allerød (BA), followed the cold Heinrich Stadial 1 (HS1; 17.5–14.7 kyr BP) and marks a rapid transition to warmer conditions within decades to centuries (Thiagarajan *et al.*, 2014; Rasmussen *et al.*, 2014). The onset of the BA was associated with a strong recovery of the Atlantic Meridional Overturning Circulation (AMOC), widespread North Atlantic and global warming, sea-ice retreat, and reorganization of atmospheric circulation (Mcmanus *et al.*, 2004; Liu *et al.*, 2009; Shakun *et al.*, 2012). These changes triggered global temperature rise, reactivation of monsoon systems, and rapid transformations in hydrological regimes (Wang *et al.*, 2006; Shakun *et al.*, 2012; Chiessi *et al.*, 2015b).

In South America, the deglacial period was characterized by pronounced shifts in the hydroclimate regime (Fornace *et al.*, 2014; Chiessi *et al.*, 2015b; Mulitza *et al.*, 2017; Novello *et al.*, 2017). During the Bølling-Allerød interval, the stronger AMOC enhanced northward heat transport and altered atmospheric circulation patterns linked to the South American summer monsoon (SASM), such as a northward displacement of the Intertropical Convergence Zone (ITCZ), leading to drier conditions in several regions (Fornace *et al.*, 2014; Chiessi *et al.*, 2015b; Mulitza *et al.*, 2017; Novello *et al.*, 2017).

The SASM is the fundamental driver of the rainfall regime across South America. This large-scale circulation pattern delivers the vast majority of annual precipitation to the continent's core, including the Amazon Basin, the Cerrado savanna, and the Pantanal wetlands. It occurs during austral spring and summer (Oct-Mar – Fig.4.1) due to the increase in austral summer insolation and the consequent southward displacement of the ITCZ, which enhances the moisture flow from the Tropical Atlantic into the continent (Zhou and Lau, 2001; Vera *et al.*, 2006; Orrison *et al.*, 2022). The SASM is responsible for most of the moisture distribution over the continent along with its main component, the South Atlantic Convergence Zone (SACZ), a NW-SE convective band that stretches over central and southeastern Brazil into the South Atlantic Ocean (Carvalho, Jones and Liebmann, 2004) – Fig. 4.1). When the monsoon system is enhanced, especially over western Amazon and southern Brazil, the increased convection leads to a regional air subsidence over northeastern Brazil and tropical South Atlantic, establishing the upper-level circulation known as the Bolivian High – Nordeste Low (BH-NL) system (Lenters and Cook, 1997; Sulca *et al.*, 2016; Campos *et al.*, 2019). This leads to a well-known east-west rainfall dipole within South America (Cheng, Sinha, *et al.*, 2013; Campos *et al.*, 2019; Della Libera *et al.*, 2022; Orrison *et al.*, 2022).

The zonal dipole has been documented on different time scales, from orbital (Cruz *et al.*, 2009; Cheng, Sinha, *et al.*, 2013; Deininger *et al.*, 2019), millennial (Wong *et al.*, 2023; Della Libera *et al.*, accepted), to centennial time scales (Novello *et al.*, 2018; Campos *et al.*, 2019; Della Libera *et al.*, 2022), and its forcing has already been thoroughly discussed. For instance, on orbital time-scales, the SASM is highly sensitive to austral summer insolation, where increased (reduced) insolation leads to enhanced (weakened) monsoon strength (Deininger *et al.,* 2019; Cruz *et al.,* 2009). On millennial time scales, such as during the Holocene, the increase in insolation led to a progressive increase in monsoon strength, and positioning of the SACZ over central parts of Brazil was associated to the dipole configuration (Novello *et al.,* 2018; Della Libera *et al.*, accepted*;* (Wong *et al.*, 2023). On the other hand, as SACZ is located over central parts of Brazil, some regions may not present trends in their climate records during the Holocene as a consequence of their centered position in the dipole on orbital time-scales (Wong *et al.*, 2021); Della Libera *et al.*, accepted).

Climate variability in tropical South America during the deglacial period, especially during the Bølling-Allerød interval, has not been discussed in detail yet, although a lot of attention has been given to the preceding and following cold climate events, i.e., the HS1 and the Younger Dryas (YD; 12.9–11.7 kyr BP), respectively (e.g., Stríkis *et al.*, 2015; Novello *et al.*, 2017; Venancio *et al.*, 2020a,b). One of the few studies assessing the deglacial period is by Bao et al (2023a,b), who investigated the South American precipitation dipole using isotope-enabled climate model simulations and speleothem $\delta^{18}O$ data. They identified a persistent dipole pattern between the central–western Amazon and eastern Brazil/Atlantic coast, demonstrating that $\delta^{18}O$ in precipitation ($\delta^{18}O_P$) over the western Amazon is influenced by both the moisture-source and amount effects, whereas $\delta^{18}O_P$ in eastern Brazil primarily reflects variations in the isotopic composition of incoming moisture. At more inland sites in eastern Brazil, however, local rainfall variability can amplify the amount effect, particularly during large-scale millennial events of the last deglaciation. Despite these complex controls, they conclude that $\delta^{18}O_P$ largely tracks the rainfall-based dipole, marked by a wet–dry–wet sequence (HS1-BA-YD) in the east and the opposite in the west, still indicating a dynamically stable monsoon dipole structure during the deglacial events. Complementary isotope-enabled modeling studies (Orrison *et al.,* 2022; Wong *et al.*, 2023) further demonstrate that $\delta^{18}O$ variability across the SASM domain reflects both precipitation and circulation effects, with isotopic gradients modulated by moisture source and fractionation processes. Altogether, these findings suggest that while a robust precipitation dipole persists, the associated isotopic dipole integrates multiple hydrological and atmospheric processes.

Here, we present two new speleothem isotope records covering the deglacial period. The first is from São Mateus cave in central-eastern Brazil, occupying a strategic position at the midpoint of the dipole known from modern observations. The second is from Lavra cave in southwestern, lowland Amazon basin, located at the core region of SASM, filling a special gap of stalagmite records. Moreover, we compile proxy records from a broad region in tropical South America to create a spatially comprehensive proxy-based climate assessment of this time period. We present for the first time an in-phase climate behavior during the deglacial period that contrasts with the observed monsoon rainfall patterns documented during the other time periods, as it does not show the dipole pattern observed for example in the Holocene.

4.3 Samples and study areas

We sampled two speleothems that cover the period of interest. Stalagmite SMT16 (Supp. Fig. 4.1) was collected in the 700 Hall (Salão Setecentos) of São Mateus cave (13.67° S; 46.37° W, 623 m a.s.l. – Fig.1), located at the State Park of Terra Ronca (PETER), Goiás state, Central Brazil.SMT16 is a ~470 mm-long aragonite stalagmite without signs of recrystallization or dissolution, (Supp. Fig. 4.1). The climate in PETER is characterized as tropical semi-humid with a bimodal pattern of precipitation with wet summer and dry winter seasons. The mean annual precipitation between 1974 and 2023 is 1,428 mm yr^{-1} based on the meteorological station São Vicente (~14km from São Mateus cave). The largest part of rainfall (80%) occurs between October and April during the summer monsoon season and SACZ active period. The mean annual temperature is 24°C with the monthly mean ranging between 22.5 °C during winter and 25.8 °C during summer (Moquet *et al.*, 2016).

The flowstone LVR6 (~61 mm long) was collected in Lavra cave (11°40’S, 60°80’W, ~310 m a.s.l.), located in Pimenta Bueno city, Rondônia State, SW Amazon region in Brazil. The climate is characterized as tropical humid with an annual average temperature of 26°C. Located within the core SASM region, the average annual rainfall amount is about 1800 mm, 90% of which falls between October and April during the summer monsoon season.

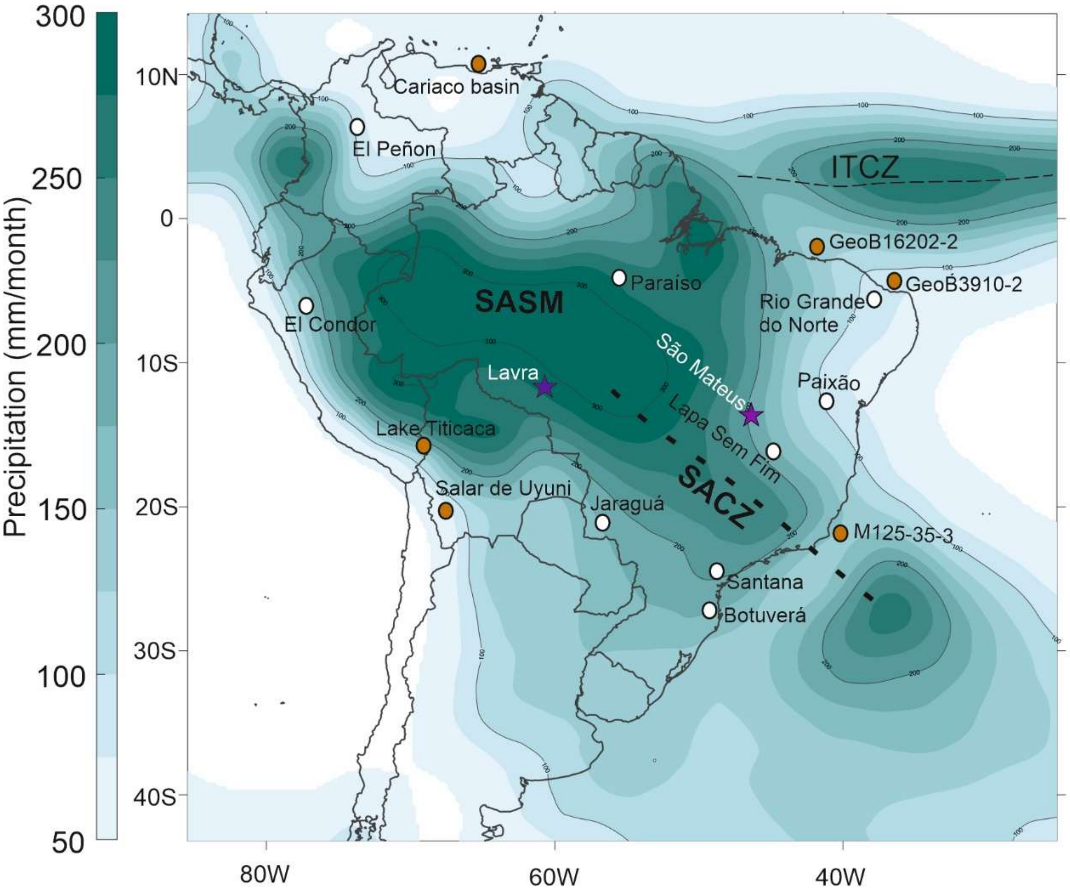

Figure 4.1 - Map of South America with austral summer precipitation during peak monsoon season (DJF) from Global Precipitation Measurement Mission (GPM, 2001-2020) (Huffman *et al.*, 2019). Main summer climate features over the continent indicated as SASM (South American Summer monsoon) and SACZ (South Atlantic Convergence Zone), with its mean location represented by the dashed line. The climatological DFJ location of Intertropical Convergence Zone (ITCZ) is represented by the dashed line. Map shows location of São Mateus (pink) and Gruta da Lavra caves (purple) along with the other records discussed in the paper, as follows: Rio Grande do Norte (Cruz *et al.*, 2009; Utida *et al.*, 2020); marine sediment core GeoB3910-2 (Jaeschke *et al.*, 2007); b) Paixão cave (Stríkis *et al.*, 2015); Lapa Sem Fim cave (Azevedo *et al.*, 2021); Jaraguá cave (Novello *et al.*, 2019); marine sediment core M125-35-3 (Meier *et al.*, 2020); Salar de Uyuni Natural (Baker *et al.*, 2001); El Condor cave (Cheng *et al.*, 2013a); Botuverá cave (Cruz *et al.*, 2006), Santanta cave (Cruz *et al.*, 2006); El Penon cave (Ramirez *et al.*, 2023); Cariaco Basin (Lea *et al.*, 2003; Deplazes et al, 2013); marine sediment core of GGC5 (McManus *et al.*, 2004); GeoB16202-2 (Mulitza *et al.*, 2017).

4.4 Methods

4.4.1 Chronology

The chronologies of SMT16 and LVR6 were determined by ^{230}Th dating and the analysis was performed by a multi-collector inductively coupled plasma mass spectrometry (MC-ICP-MS). SMT16 was prepared following the chemical procedures similar to those described in *Edwards et al.*, (1987), and analysed at the Geochronology Laboratory at the University of Minnesota (USA) and at the Institute of Global Environmental Change, Xi'an Jiaotong University (China), following the methods described in Cheng *et al.*, (2013b). LVR6 was prepared and analyzed at the Institute for Geosciences, Johannes-Gutenberg University-Mainz (Germany), following the methodology described in Klose *et al.* (2024). Both age models were constructed using StalAge (Scholz & Hoffmann, 2011) (Supp. Fig.4.1, 4.2). For LVR6, the low ^{230}Th/^{232}Th activity ratios suggest that conventional detrital corrections may be insufficient. Therefore, in order to account for high detrital contamination, we used the approach from Budsky *et al.* (2019) to estimate the best detrital correction factor based on the number of inversions and on the sum of age inversions.

4.4.2 Stable oxygen and Strontium isotope analysis

The isotopic profile of SMT16 for the 470 mm consists of 1512 points sampled with ~0.3mm spacing and is constrained by 25 ^{230}Th-U ages. LVR6 is a ~65mm long flowstone with its isotopic profile determined by 64 points sampled with 1mm spacing and the age model being constrained by 8 ^{230}Th-U ages (Supp. Fig. 4.2).

The SMT16 δ^{18}O analyses were performed at the Laboratory of Stable Isotopes at the Institute of Geoscience of the University of São Paulo (LES-USP) and at the Laboratory of Geodynamic, Geochronological and Environmental Studies of the University of Brasilia (LEGGA – UnB). At LES-USP, a Thermo-Finnigan Delta Plus Advantage mass spectrometer coupled to a Gas Bench online sample preparation system was used, and at LEGGA – UnB, a Thermo MAT 253 attached to a Kiel IV Carbonate device. LVR δ^{18}O analyses were performed at on a Thermo Delta V mass spectrometer equipped with a GASBENCH-II preparation device at the Max Planck Institute for Chemistry, Mainz. Stable isotope ratios are expressed in δ-notation against Vienna Pee Dee Belemnite (VPDB) using the following equation: $\delta^{18}O = [((^{18}O/^{16}O)_{sample} / (^{18}O/^{16}O)_{VPDB}) - 1] \times 10^3$ (example equation for the oxygen isotope values). Analytical uncertainties (1SD) based on the reproducibility of routinely measured in-house standards better than 0.1‰ for both analyses in all labs.

The $^{87}Sr/^{86}Sr$ isotope ratios for SMT16 were determined and analyzed by laser ablation (LA) MC-ICP-MS at Johannes-Gutenberg University (JGU) Mainz (Supp. Text 4.1). International Laser ablation MC-ICP-MS data were calibrated against NanoSr as the main reference material, with JCt-1 and JCp-1 acting as quality controls (Supp. Table 1). The $^{87}Sr/^{86}Sr$ ratios obtained from all three reference materials were within the range of published solution-based values (Weber *et al.*, 2018; 2020).

4.5 Results

The SMT16 $\delta^{18}O$ record covers the period between -0.024 (+0.01, -0.04) kyr BP and 15.71 (+0.034, -0.035) kyr BP. The longest section of the sample (0-404 mm) covers the Holocene period from -0.024 kyr BP to 11.07 (+0.11, -0.11) kyr BP and shows continuous growth. The average sampling resolution of the record is 8 years, and this section was already investigated by Della Libera *et al.,* accepted). The transition to the second section of the speleothem is marked by a clear shift in the dripping point and a thin white layer (Supp. Fig. 4.1), presenting a hiatus between 11.07 and 12.10 (+0.075, -0.09) kyr BP (1024 years) based on the age model. The section covering the deglacial period (406-470 mm) ranges from 12.10 to 15.71 kyr BP, with an overall 2σ ^{230}Th-U age uncertainty of 0.4% or ± 65 yr for the ^{230}Th-U ages (Supp. Table 4.2) and an average temporal resolution of 19 years. This period presents a lower $\delta^{18}O$ mean value (-5.4‰) compared to the Holocene (-3.3‰), with values ranging from -7.0 to -3.2‰. The $\delta^{18}O$ values are more negative during the HS1a (16.11 to 14.69 kyr BP – mean = -6‰) and the YD (mean= -6.2‰) in comparison with the BA period (mean = -4‰).

The LVR6 $\delta^{18}O$ record covers the deglacial period between 11.54 (+0.9, -1.9) to 16.11 (+3.6, -2.1) kyr BP with a mean of -6‰ (VPDB), with a total range of -6.9 to -5.1‰. It presents an overall 2σ ^{230}Th-U age uncertainty of 11% or ±1.64 kyr based on the ^{230}Th-U ages and an average temporal resolution of 72 years. The $^{232}Th/^{238}U$ ratio of the detrital component obtained by the method of Budsky *et al.* (2019) is 0.909, which deviates from the usually used bulk Earth value of 3.8, and results in significantly younger corrected ages of LVR6 compared to the ones corrected by the conventional method (Supp. Table 4.3). The $\delta^{18}O$ profile presents a trend towards more negative values from the oldest part of the record until 12.45 (+1.5, -0.74) kyr BP, with an increase until 11.54 kyr BP.

The $^{87}Sr/^{86}Sr$ record of SMT16 is composed of 104 data points, ranging from 0.70972 to 0.71186. The section of the speleothem corresponding to the Holocene (0-404mm) was already published and discussed by Della Libera *et al.* (accepted). The deglacial section (406-470 mm) presents much lower values than the Holocene section, ranging from 0.70972 to 0.71065 (Fig. 2c). The lowest values are observed within the oldest portion of the stalagmite between 15.7 and 14.6 kyr BP, followed by the highest values and peaking at 13.5 kyr BP. Subsequently, the values drop to 0.71012 at 12.1 kyr BP.

4.6 Discussion

4.6.1 Common climate behavior in tropical South America during the deglacial period

Our compilation of speleothem records across tropical South America for the end of the deglacial period reveals a coherent, in-phase relationship among all $\delta^{18}O$ records (Fig. 4.2). This pattern indicates a continent-wide synchronicity in $\delta^{18}O$ variability, spanning from 4–27°S and 39–77°W (Fig .4.1). In contrast to the Holocene and orbital time-scales, when the dipole pattern is in place, we observe the disappearance of the dipole structure during the millennial-scale HS1a, BA, and YD events, especially during the Bølling-Allerød. Previous studies have similarly reported coherent $\delta^{18}O$ and precipitation patterns across South America during this interval (Stríkis *et al.,* 2015; Novello *et al.,* 2017). Stríkis *et al.* (2015) evidenced an intensification of the SASM during the HS1a, while Novello *et al.* (2017) presented a coherent rainfall response across the monsoon belt from the Andes to southeastern Brazil during the transition from the LGM to the Holocene. Our compilation corroborates these earlier findings, but extends their interpretations both temporally and spatially through the integration of 13 records.

Even though we bring this vast compilation of continental records in South America to discuss this time period, a question that follows this consistent isotopic behavior is whether the overall low-high-low pattern observed in the $\delta^{18}O$ values are an isotope effect linked to large-scale atmospheric processes or if it also characterizes a cohesive climate pattern throughout tropical South America for the deglacial period. To address that, we bring records that primarily indicate local precipitation conditions in addition to the speleothem $\delta^{18}O$ records.

According to the local $^{87}Sr/^{86}Sr$ signal interpretation of SMT16 described in Della Libera *et al.* (accepted), the Sr isotopes in São Mateus cave present higher values during drier conditions, and wetter for lower values. In general, the Sr isotope signals in São Mateus present a specific local setting that drives the main $^{87}Sr/^{86}Sr$ changes: either the influence of mixed lithology (limestone vs. silicate layers) or increased dust input from the nearby sandstone unit during drier periods (Della Libera *et al.,* accepted) lead to an increase of the $^{87}Sr/^{86}Sr$ isotope values. The opposite scenario, i.e., wetter periods capture more the limestone signal, lowering the $^{87}Sr/^{86}Sr$ isotope values. Therefore, the $^{87}Sr/^{86}Sr$ SMT16 record indicates a wet-dry-wet sequence for the deglacial, following the same $\delta^{18}O$ structure (Fig. 4.2c). It suggests that the $\delta^{18}O$ is indeed representing the local rainfall during the deglacial period, at least in central-east Brazil. This pattern is corroborated by the models performed by Bao *et al.* (2023a,b), where they show that sites located in eastern Brazil, such as São Mateus, Paixão (Stríkis *et al.,* 2015) and Lapa Sem Fim (Stríkis *et al.,* 2015) caves, are consistent with the isotopic "amount effect" for the deglacial period, thus presenting a wet-dry-wet scenario during HS1a-BA-YD, respectively.

Over to the west at our Lavra cave site, a previous study by Della Libera *et al.* (2022) evidences the strong correlation between $\delta^{18}O$ and local rainfall in this region, since it is mainly controlled by SASM (90%) precipitation and it is located at the core region of the convective activity of the monsoon. Therefore, our record suggests increasingly wetter conditions during the HS1a followed by a drier event during the Bølling-Allerød and a further wetter period at the YD (Fig. 4.2f). Further evidence based on effective moisture records at other sites in western Amazonia, like in Lake Titicaca (Fornace *et al.,* 2014) and Salar de Uyuni (Baker *et al.*, 2001) - Fig. 4.2h) corroborates this pattern at the western region, presenting the same wet-dry-wet configuration during HS1a-BA-YD. Along with the preceding data from the east, this already evidences how east and western South America are presenting very similar precipitation and isotope behaviors, with still no sign of a dipole in place.

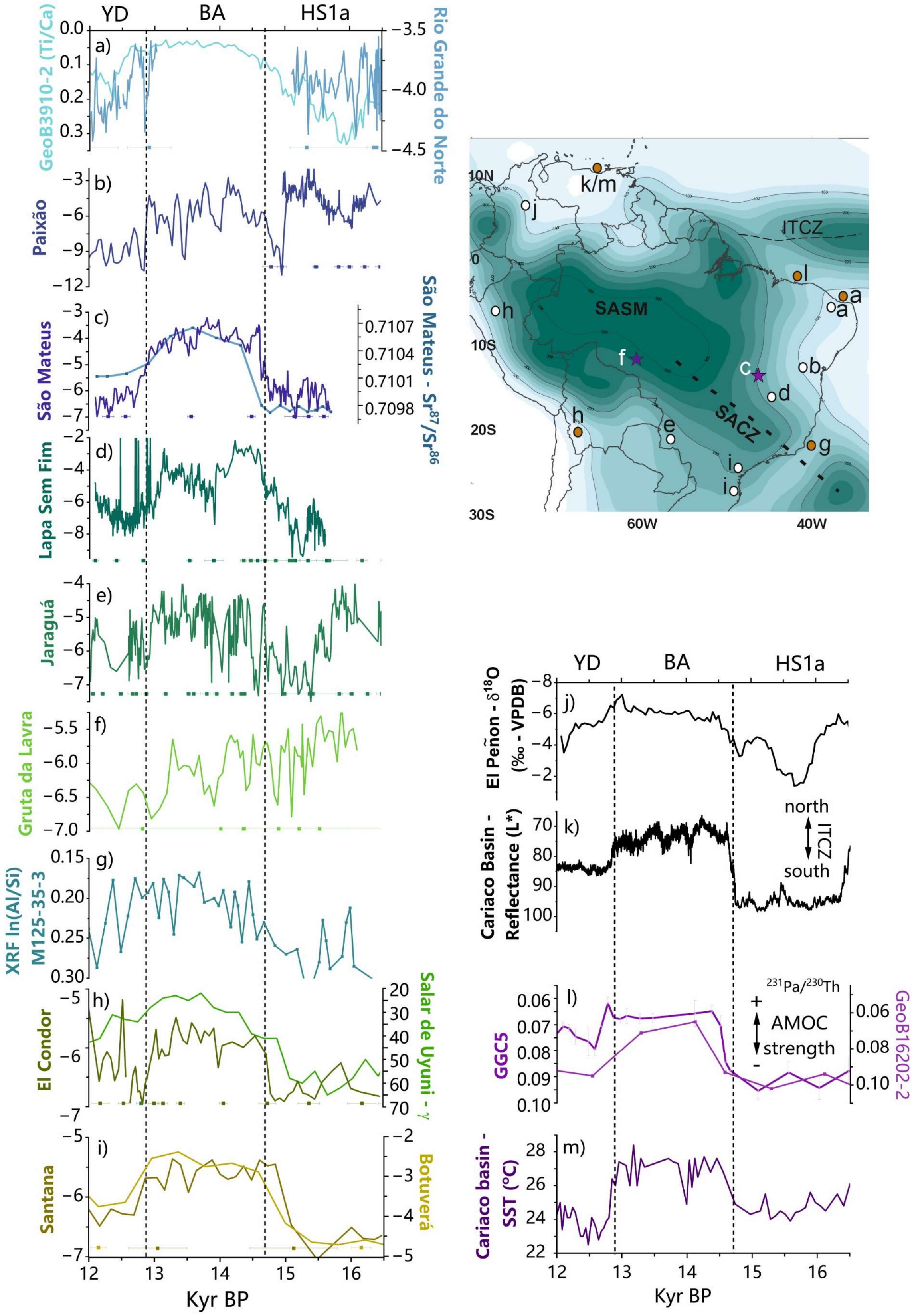

Figure 4.2 -Comparison between compiled records, also indicated in the map of South America as follows: a) Rio Grande do Norte $\delta^{18}O$ (dark blue – Cruz *et al.*, 2009; Utida *et al.*, 2020), marine sediment core GeoB3910-2 Ti/Ca

record (light blue – Jaeschke *et al.*, 2007) b) Paixão cave $\delta^{18}O$ record (Stríkis *et al.*, 2015); c) São Mateus $\delta^{18}O$ (purple) and $^{87}Sr/^{86}Sr$ (blue) records (this study); d) Lapa Sem Fim cave $\delta^{18}O$ record (Azevedo *et al.*, 2021); e) Jaraguá cave $\delta^{18}O$ record (Novello *et al.*, 2019); f) Gruta da Lavra cave $\delta^{18}O$ record (this study); g) marine sediment core M125-35-3 ln(Al/Si) record (Meier *et al.*, 2020); h) Salar de Uyuni Natural γ-radiation (c.p.s.) record (light green – Baker *et al.*, 2001a), El Condor cave $\delta^{18}O$ record (dark green – Cheng *et al.*, 2013); i) Botuverá cave $\delta^{18}O$ record (light yellow – Cruz *et al.*, 2006), Santanta cave $\delta^{18}O$ record (dark yellow – Cruz *et al.*, 2006); j) El Penon cave $\delta^{18}O$ record (Ramirez *et al.*, 2023); k) Cariaco Basin reflectance (*L) record (Deplazes et al, 2013); l) marine sediment core $^{231}Pa/^{230}Th$ records of GGC5 (dark purple – McManus *et al.*, 2004), and GeoB16202-2 (light purple – Mulitza *et al.*, 2017); m) Cariaco Basin SST (°C) record (Lea *et al.*, 2003).

Furthermore, other paleoprecipitation records from SA which used other proxies than $\delta^{18}O$ also corroborate the paleo rainfall pattern from the deglaciation period documented in São Mateus and Lavra caves. In northeastern Brazil, the marine sediment core GeoB3910-2 (Fig.4.2a - (Jaeschke *et al.*, 2007) shows high sedimentation rates during HS1a and YD relative to very low ones during Bølling-Allerød, indicating higher and lower rainfall amounts, respectively. Hiatuses in stalagmites indicative of water deficit at seepage cave waters occurs at BA period in caves located in Northeast Brazil (Utida *et al*, 2022), here represented as Rio Grande do Norte record, and East Amazon, i.e., Paraíso (Wang *et al.*, 2017). Further south at Botuverá cave (Cruz *et al.*, 2005; Vasconcelos *et al.*, 2025), a strong consistency between speleothem trace elements and $\delta^{18}O$ records is observed, showing a remarkable agreement between them across millennial-scale events (Vasconcelos *et al.,* 2025), thus also evidencing the same precipitation pattern. Finally, the marine sediment core M125-35-3 (Fig. 4.2g - (Meier *et al.*, 2022), located off SE Brazil where the catchment area drains the core region of the modern SACZ, also indicates higher precipitation during HS1a and YD compared to the BA (Meier *et al.,* 2022).

Overall, all the independent proxies presented above in several different regions within SA give more straightforward information about paleo-precipitation. Since these the records show a similar pattern to the one that observed in the speleothem $\delta^{18}O$ records, the evidence suggests that the deglacial climate across tropical South America was dominated by a wet-dry-wet pattern. Yet, this It supports the notion of a deglacial period in which the rainfall and isotope patterns were in phase with each other over a large area in South America, and the dipole is not in place in contrast to the observed in the Holocene (Vuille *et al.*, 2012; Campos *et al.*, 2019; Orrison *et al.*, 2022; Della Libera *et al.*, accepted).

4.6.2 Forcing of abrupt precipitation changes during the deglacial in South America

One remarkable difference between the deglaciation and the Holocene periods is that the former had much larger and more abrupt changes in temperature. These deglacial variations are largely driven by high-latitude forcings, including changes in the AMOC, a key mechanism for interhemispheric ocean heat redistribution (McManus *et al.*, 2004; Shakun *et al.*, 2012; Johnson *et al.*, 2019) and Northern Hemisphere temperature (Rasmussen *et al.*, 2014). Studies have shown that the millennial-scale climate fluctuations in South America during the deglaciation are closely aligned with abrupt events linked to AMOC variability (Stríkis *et al.*, 2015;Santos *et al.*, 2022) - Fig. 4.2l) and rapid Northern Hemisphere temperature shifts (Novello *et al.*, 2017), coeval to the records in Greenland ice cores (Rasmussen *et al.*, 2014; Fig. 4.3a). In contrast, during the Holocene, $\delta^{18}O$ records across tropical South America closely follow gradual changes in austral summer insolation (Cruz *et al.*, 2005; Vasconcelos *et al.*, 2025), and the precipitation dipole is established (Fig. 4.4). This indicates that insolation was the primary driver of South American climate during this period, with minimal coherence to Northern Hemisphere forcing, whose variability was substantially lower than during the deglaciation.

AMOC variations regulate cross-equatorial heat transport and influence precipitation patterns in tropical South America. When AMOC is weak, heat is retained in the Southern Hemisphere, increasing the North–South Atlantic temperature gradient, shifting the ITCZ southward toward the warmer ocean, and enhancing the SASM/SACZ systems (Meier *et al.*, 2022). Conversely, a strong AMOC transports more heat to the North Atlantic, cooling tropical Southern Hemisphere SSTs, warming the north, and driving a northward ITCZ shift (Santos *et al.*, 2022; Meier *et al.*, 2022). This can be observed in the concomitant wet phase in Cariaco Basin and El Peñon cave records (Fig. 4.2j, k, respectively), both located above the equator and behaving in antiphase with the sites below the equator in tropical South America, as discussed in the section above. Hence, these SST gradients modulate precipitation distribution across South America (Santos *et al.*, 2022; Meier *et al.*, 2022; Vasconcelos *et al.*, 2025). During interstadials, such as the BA, North Atlantic warming increases northern tropical Atlantic precipitation, weakens trade winds, and reduces rainfall over northeastern and central-east Brazil (Deplazes *et al.*, 2013). Weakened AMOC phases, such as HS1 and YD, produce the opposite effects.

Overall, the timing of these abrupt millennial-scale precipitation changes in tropical South America is closely linked to high-latitude Northern Hemisphere forcing and associated temperature shifts (Novello *et al.*, 2017; Stríkis *et al.*, 2015; Meier *et al.*, 2022). A closer comparison of the São Mateus, Lavra and other tropical South American δ^{18}O records with NH proxies, such as the Ca^{2+} and δ^{18}O from North Greenland Ice Cores records (NGRIP2- Rasmussen *et al.*, 2014 - Fig. 4.3a-i), reveals that the abrupt millennial-scale events (HS1a, BA and YD) occur synchronously across hemispheres. This reflects a tight interhemispheric coupling mediated by AMOC variability (Lea *et al.*, 2003); McManus *et al.*, 2004; Shakun *et al.*, 2012; Santos *et al.*, 2022), and, within dating errors, evidences the immediate response in South America to these events. Yet, although both HS1a and the YD exhibit strong climate anomalies, they present a certain distinction in the expression between different records within the overall wet event, whereas the Bølling–Allerød event seems to present a far more uniform response between records relative to the other two events. This continent-wide coherence signal is consistent with the sudden intensification of AMOC, resulting in widespread drying across the region.

4.6.3 Internal structure of the Bølling-Allerød in tropical South America

Even though the timing of onset and termination of the Bølling–Allerød in São Mateus δ^{18}O record follows the NH climate conditions, it does not appear to follow closely the all the short lived intra-interstadial oscillations within GI-1 (Fig. 4.3c), presenting only small oscillations in this period. In fact, it presents very similar variations to the Cariaco basin high resolution record (Fig. 4.3c - Deplazes *et al.*, 2013), which follows the intra-interstadial events with an apparent early beginning at the very start of every sub-event (Fig. 4.3a-c). São Mateus δ^{18}O record seems to follow the Cariaco variability, yet it presents a short negative excursion precisely at GI-1c2 timing of NGRIP2 (Fig. 4.3c). Moreover, the short-lived intra-interstadial can also be identified in the two higher-resolution δ^{18}O records of Jaraguá and Lapa Sem Fim caves (Fig. 3g, h), and in El Condor, in spite of the lower resolution. Therefore, since Cariaco basin is directly linked and very sensitive to ITCZ variations (Deplazes *et al.*, 2013), it could indicate that ITCZ was displaced southward at the very beginning of the events or shortly before. This led to short-lived dry conditions at Cariaco basin, concomitant with the strengthening of trade winds and easterlies that bring moisture to São Mateus cave region and SASM/SACZ (Della Libera *et al.*, accepted). Therefore, even though the excursions in the NGRIP2 record do not reach stadial values (Rasmussen *et al.*, 2014), corresponding variations are nevertheless recorded in South America, evidencing the high sensitivity of tropical South American climate to even minor oscillations in Northern Hemisphere temperature.

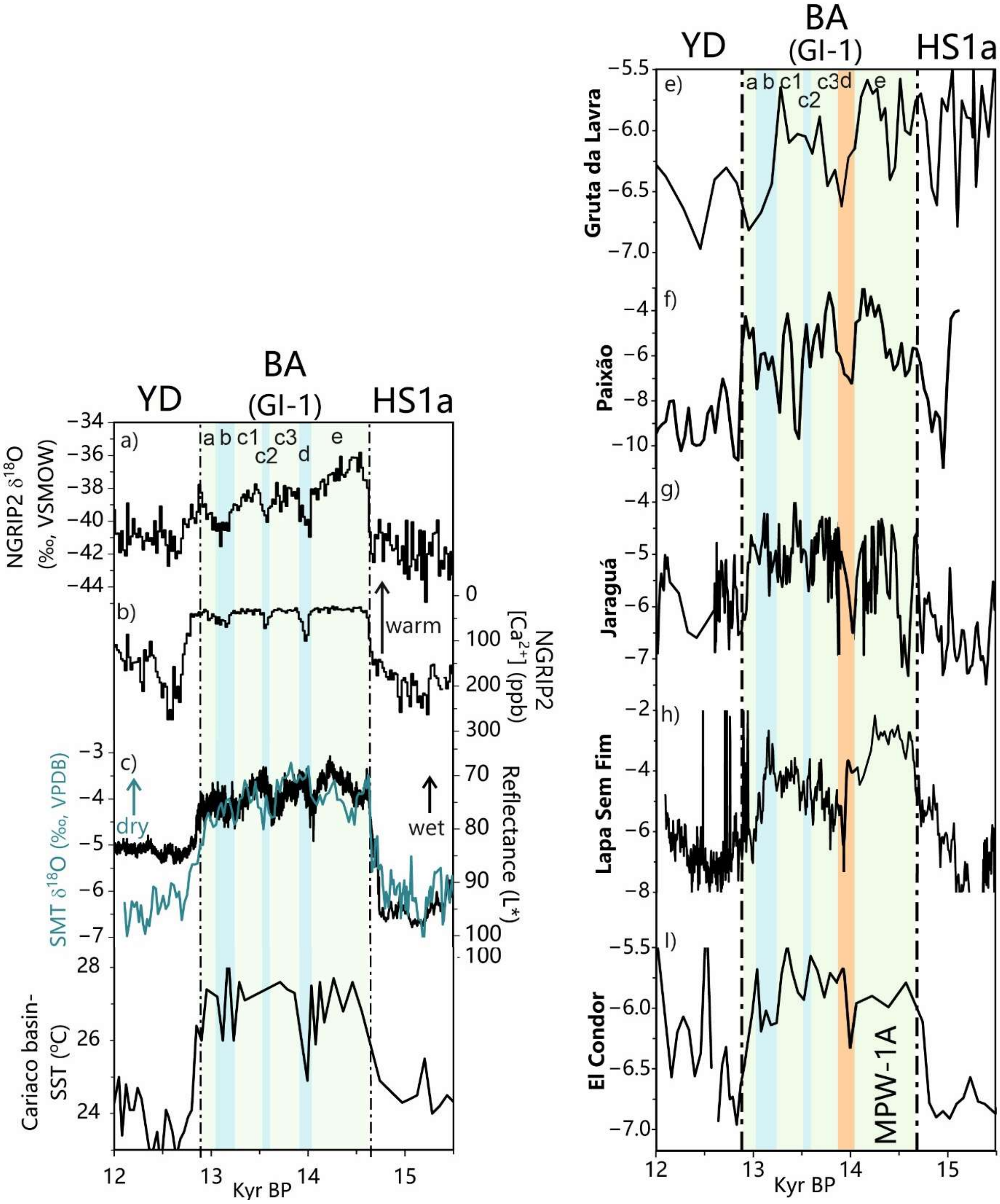

Figure 4.3 - Comparison of São Mateus, Lavra and other tropical South American δ¹⁸O records with NH proxies. a) NGRIP2 δ¹⁸O record (Rasmussen *et al.*, 2014); b) NGRIP2 Ca^{2+} record (Rasmussen *et al.*, 2014); c) São Mateus δ¹⁸O record (green, this study) and Cariaco basin reflectance (L*) (black, Deplazes *et al.*, 2013); d) Cariaco basin SST (°C) (Lea *et al.*, 2003); e) Lavra cave δ¹⁸O record (this study); f) Paixão cave (Stríkis *et al.*, 2015); g) Jaraguá cave (Novello *et al.*, 2019); h) Lapa Sem Fim cave (Azevedo *et al.*, 2021); i) El Condor cave δ¹⁸O record (Cheng *et al.*, 2013).

In contrast to the records mentioned above, the low-resolution Lavra record shows only minor variations that do not follow completely the same internal structure following neither Cariaco nor NGRIP record (Fig. 4.3e). Yet, it presents a very distinct negative excursion at ~13.9 kyr BP in the middle of the BA event (Fig. 4.3e). The same structure can be observed in other records from different regions of tropical South America, such as Paixão in northeastern Brazil, Lapa Sem Fim also in central-east, Jaraguá in central-west and El Condor in the Peruvian Altiplanos (Fig. 4.3e-i). All of these records present a concurrent pronounced negative excursion in the $\delta^{18}O$ records, what is likely a strong expression of the GI-1d event observed at the NGRIP2 record at 14 kyr BP (Fig. 4.3a). The GI-1d in the NGRIP ice core (Fig. 4.3a,b) is marked by a rise in Ca^{2+} together with a drop in $\delta^{18}O$ records, evidencing a transient return to colder, dustier conditions, i.e., a brief stadial-like reversal within the broader warm interval (Steffensen *et al.*, 2008; Rasmussen *et al.*, 2014). Although GI-1d is short, intra-interstadial oscillations can reflect transient reorganizations of ocean convection that lead to AMOC modulation and ITCZ/monsoon shifts, which will, in turn, alter South American precipitation patterns (Mcmanus *et al.*, 2004; Liu *et al.*, 2009; Kanner *et al.*, 2012; Deplazes *et al.*, 2013).

A remaining question, however, is why the event at the same time as GI-1d produced such a prominent hydrological signal in tropical South America compared to later sub-events, such as GI-1b, which appears stronger in the NGRIP2 $\delta^{18}O$ record (Fig. 4.3a). One possible explanation relies on the preceding event of Meltwater Pulse 1A (MWP-1A). This event was responsible for the fastest rate of sea-level rise due to melting of ice sheets in the deglaciation period, occurring between ~14.6-14 kyr BP (Fig. 4.3 - (Deschamps *et al.*, 2012; Santos *et al.*, 2022). This is coeval with reduced SST temperatures at the Brazilian margin and the most increased northward heat transport from the South Atlantic Ocean during the Bølling-Allerød (Santos *et al.*, 2022). The completion of the sea-level jump at ~14 kyr BP agrees with the sudden return to warmer SSTs at the Brazilian margins and with a short-lived return to less northward heat transport (Santos *et al.*, 2022), along with the most pronounced cooling in the Cariaco Basin (tropical North Atlantic) during the Bølling-Allerød event (Fig. 4.3d). Therefore, this might have been the strongest short-lived event during the Bølling-Allerød given the SSTs return to warmer conditions in the Southern Atlantic Ocean was the most pronounced of the entire period, which agrees with the less distinct intra-interstadial fluctuations observed later on.

Finally, the Holocene period is again modulated by the insolation rather than by changes in AMOC strength, with the SASM dipole pattern again in place (Fig. 4.4 - Cruz *et al.*, 2009; Cheng *et al.*, 2013; Campos *et al.* 2019; Della Libera *et al.*, 2022, accepted). The gradual increase in insolation throughout the Holocene reestablishment of the dipole structure: a dry early Holocene period throughout the SAMS domain with a negative (wetting) trend (Fig. 4g,h), in contrast to the records NE Brazil (RN) and eastern Amazonia (PAR) with an overall wet early Holocene and a trend to drier conditions for the same period (Fig. 4.3a,b,c), whereas SACZ records present weaker trends (Fig. 4d,e,f – Bernal *et al.*, 2016; Campos *et al.*, 2019; Wong *et al.*, 2021; Della Libera *et al.*, 2022, accepted).

This reflects how interhemispheric temperature gradients influence tropical precipitation dynamics through changes in large-scale atmospheric circulation during orbital and even short-lived events. While the enhanced precipitation and a coherent increase in precipitation over tropical South America has been discussed for the HS1a and YD periods (Novello *et al.*, 2017; Stríkis *et al.,*2015; Santos *et al.*, 2022), it is the first time that a dry period as the Bølling-Allerød is observed in such a continental extension, which was so uniformly dry that a dipole structure is no longer detectable on the millennial scale.

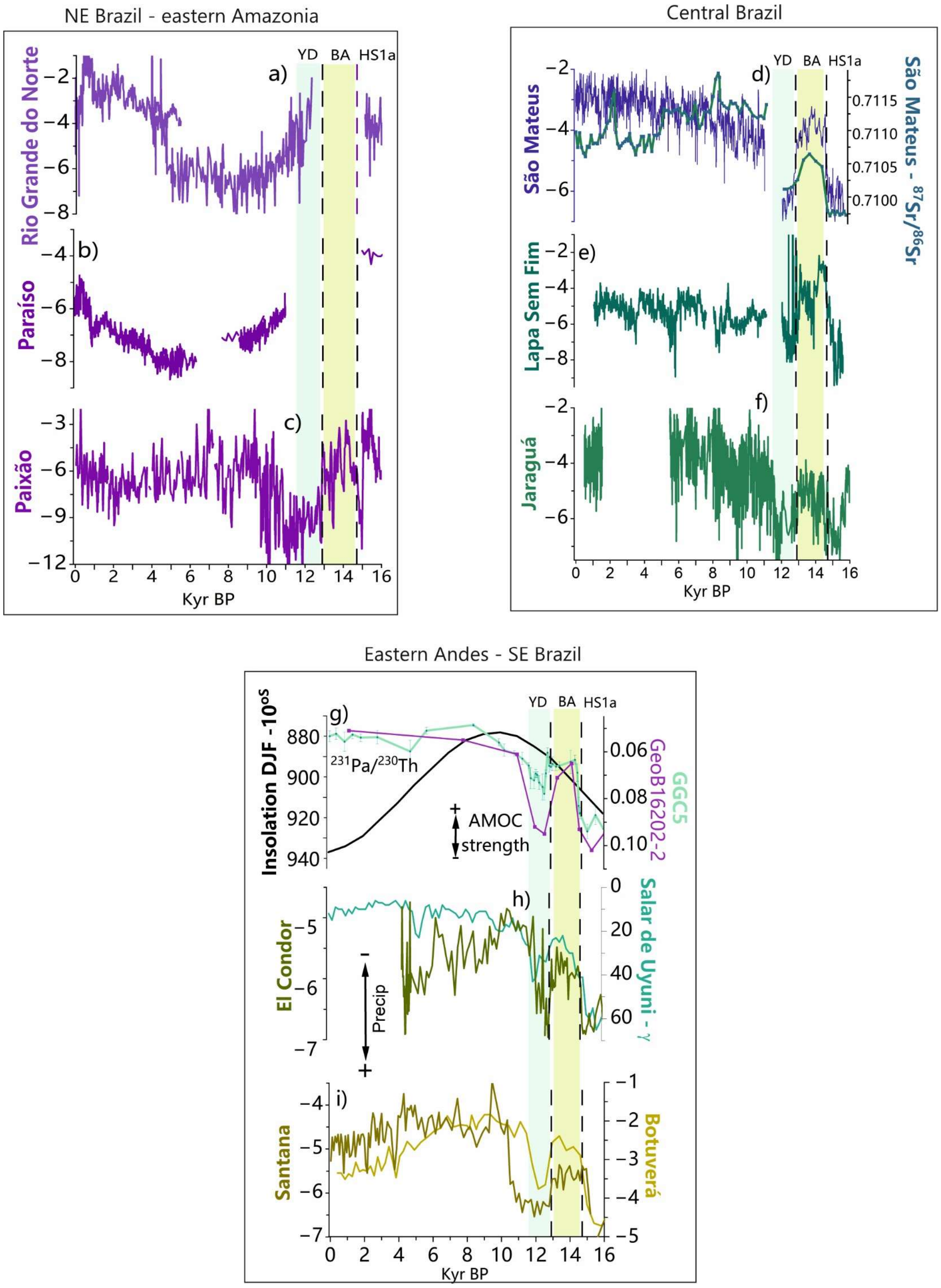

Figure 4.4 - Comparison between Holocene and deglacial time period between South American δ^{18}O records: a) Rio Grande do Norte δ^{18}O (Cruz *et al.*, 2009; Utida *et al.*, 2020), b) Paraíso cave (Wang *et al.*, 2017); c)Paixão cave (Stríkis *et al.*, 2015); d) São Mateus (blue) and ^{87}Sr/^{86}Sr (green) records (Della Libera *et al.*, accepted and this study); e) Lapa Sem Fim cave (Azevedo *et al.*, 2021); f) Jaraguá cave (Novello *et al.*, 2019); g) marine sediment core ^{231}Pa/^{230}Th records of GGC5 (green – McManus *et al.*, 2004), GeoB16202-2 (light purple – Mulitza *et al.*, 2017), and Insolation during DJF (10°S) (Berger & Loutre, 1991); h) Salar de Uyuni Natural γ-radiation (c.p.s.) record (light green – Baker *et al.*, 2001), El Condor cave δ^{18}O record (dark green – Cheng *et al.*, 2013a); i) Botuverá cave δ^{18}O record (light yellow – Cruz *et al.*, 2006), Santana cave δ^{18}O record (dark yellow – Cruz *et al.*, 2006).

4.7 Conclusions

Our compilation of continental and marine records across tropical South America shows a continent-wide in-phase climate variability during the HS1a-BA-YD deglacial events, suggesting that the east-west climate dipole known during the Holocene and in multiple time-scales was absent during the deglacial period. The new São Mateus (SMT16) and Lavra (LVR6) $\delta^{18}O$ records confirms that this pattern is consistent also at the north-eastern limit of SACZ in central-east Brazil and in the lowland region of Amazon, respectively. We compiled both speleothem $\delta^{18}O$ records and independent precipitation-sensitive proxies to access whether this synchronous variability was in fact a precipitation-led phasing or an isotope effect due to changes in atmospheric circulation. The data collected until this point suggest that the HS1a-BA-YD deglacial period was actually an in-phase precipitation period across the continent with a wet-dry-wet pattern, respectively, revealing the absence of the precipitation dipole. Moreover, the local $^{87}Sr/^{86}Sr$ signal from SMT16 as we have it suggests that there is a precipitation effect since it parallels the $\delta^{18}O$ trends. Yet, further investigation is still necessary to confirm this overall wet-dry-wet trend, for instance with trace element ratios.

Additionally, we show that the millennial-scale precipitation changes across tropical South America during the deglaciation were strongly linked to the AMOC-driven interhemispheric heat redistribution, a period of rapid climate, oceanic and AMOC changes in comparison with the gradual insolation forcing observed for the Holocene. Periods of weak AMOC (HS1 and YD) corresponded to enhanced SASM/SACZ activity and widespread wet conditions, while strong AMOC phases (Bølling-Allerød) led to ITCZ northward migration, weakened monsoonal circulation, and continent-wide drying. This general effect over the deglaciation is even possible when we look at the shorter time-scales events during the Bølling-Allerød event. The intra-interstadial events observed in Greenland ice cores during the GI-1 seem to correlate reasonably well with precipitation in South America, confirming synchronous inter-hemispheric response to even smaller events occurring in the northern hemisphere that yield short-lived changes in ITCZ position. The event at ~14 kyr BP stands out as a particularly strong hydrological anomaly in South America during the Bølling-Allerød event, likely intensified by oceanic reorganization following MWP-1A. Altogether, these findings highlight that tropical South American hydroclimate during the deglaciation was highly sensitive to abrupt AMOC variability, demonstrating tight hemispheric coupling.

4.8 References

Azevedo, V., Strikis, N.M., Novello, V.F., Roland, C.L., Cruz, F.W., Santos, R.V., Vuille, M., Utida, G., De Andrade, F.R.D., Cheng, H., Edwards, R.L., 2021. Paleovegetation seesaw in Brazil since the Late Pleistocene: A multiproxy study of two biomes. Earth and Planetary Science Letters 563, 116880–116880. https://doi.org/10.1016/j.epsl.2021.116880

Baker, P.A., Rigsby2, C.A., Seltzer3, G.O., Fritz, S.C., Lowensteink, T.K., Bacher, N.P., Veliz3, C., 2001. Tropical climate changes at millennial and orbital timescales on the Bolivian Altiplano (No. 14,900±16,600).

Bao, Y., Liu, Z., He, C., 2023a. Dipole Response of Millennial Variability in Tropical South American Precipitation and d18Op during the Last Deglaciation. Part II: d18Op Response. Journal of Climate 36, 4709–4721. https://doi.org/10.1175/JCLI-D-22-0289.1

Bao, Y., Liu, Z., He, C., 2023b. Dipole Response of Millennial Variability in Tropical South American Precipitation and δ18Op during the Last Deglaciation. Part I: Rainfall Response. Journal of Climate 36, 4691–4707. https://doi.org/10.1175/JCLI-D-22-0172.1

Berger, A., Loutre, M.F., 1991. Insolation values for the climate of the last 10 million years. Quaternary Science Reviews 10, 297–317. https://doi.org/10.1016/0277-3791(91)90033-Q

Bernal, J.P., Cruz, F.W., Stríkis, N.M., Wang, X., Deininger, M., Catunda, M.C.A., Ortega-Obregón, C., Cheng, H., Edwards, R.L., Auler, A.S., 2016. High-resolution Holocene South American monsoon history recorded by a speleothem from Botuverá Cave, Brazil. Earth and Planetary Science Letters 450, 186–196. https://doi.org/10.1016/j.epsl.2016.06.008

Budsky, A., Scholz, D., Wassenburg, J.A., Mertz-Kraus, R., Spötl, C., Riechelmann, D.F., Gibert, L., Jochum, K.P., Andreae, M.O., 2019. Speleothem δ13 C record suggests enhanced spring/summer drought in south-eastern Spain between 9.7 and 7.8 ka – A circum-Western Mediterranean anomaly? The Holocene 29, 1113–1133. https://doi.org/10.1177/0959683619838021

Campos, J.L.P.S., Cruz, F.W., Ambrizzi, T., Deininger, M., Vuille, M., Novello, V.F., Strikis, N.M., 2019. Coherent South American Monsoon Variability During the Last Millennium Revealed Through High-Resolution Proxy Records. Geophysical Research Letters 46, 8261–8270. https://doi.org/10.1029/2019GL082513

Carvalho, L.M.V., Jones, C., Liebmann, B., 2004. The South Atlantic convergence zone: Intensity, form, persistence, and relationships with intraseasonal to interannual activity and extreme rainfall. Journal of Climate 17, 88–108. https://doi.org/10.1175/1520-0442(2004)017%253C0088:TSACZI%253E2.0.CO;2

Cheng, H., Lawrence Edwards, R., Shen, C.C., Polyak, V.J., Asmerom, Y., Woodhead, J., Hellstrom, J., Wang, Y., Kong, X., Spötl, C., Wang, X., Calvin Alexander, E., 2013a. Improvements in 230Th dating, 230Th and 234U half-life values, and U-Th isotopic measurements by multi-collector inductively coupled plasma mass spectrometry. Earth and Planetary Science Letters. https://doi.org/10.1016/j.epsl.2013.04.006

Cheng, H., Sinha, A., Cruz, F.W., Wang, X., Edwards, R.L., D'Horta, F.M., Ribas, C.C., Vuille, M., Stott, L.D., Auler, A.S., 2013b. Climate change patterns in Amazonia and biodiversity. Nature Communications 4, 1411–1411. https://doi.org/10.1038/ncomms2415

Chiessi, C.M., Mulitza, S., Mollenhauer, G., Silva, J.B., Groeneveld, J., Prange, M., 2015. Thermal evolution of the western South Atlantic and the adjacent continent during Termination 1. Clim. Past 11, 915–929. https://doi.org/10.5194/cp-11-915-2015

Cruz, F.W., Burns, S.J., Karmann, I., Sharp, W.D., Vuille, M., 2006. Reconstruction of regional atmospheric circulation features during the late Pleistocene in subtropical Brazil from oxygen isotope composition of speleothems. Earth and Planetary Science Letters 248, 495–507. https://doi.org/10.1016/j.epsl.2006.06.019

Cruz, F.W., Vuille, M., Burns, S.J., Wang, X., Cheng, H., Werner, M., Lawrence Edwards, R., Karmann, I., Auler, A.S., Nguyen, H., 2009. Orbitally driven east-west antiphasing of South American precipitation. Nature Geoscience 2, 210–214. https://doi.org/10.1038/ngeo444

Deininger, M., Ward, B.M., Novello, V.F., Cruz, F.W., 2019. Late quaternary variations in the south american monsoon system as inferred by speleothems—new perspectives using the SISAL database. Quaternary 2. https://doi.org/10.3390/quat2010006

Della Libera, M.E., Novello, V.F., Cruz, F.W., Orrison, R., Vuille, M., Maezumi, S.Y., de Souza, J., Cauhy, J., Campos, J.L.P.S., Ampuero, A., Utida, G., Stríkis, N.M., Stumpf, C.F., Azevedo, V., Zhang, H., Edwards, R.L., Cheng, H., 2022. Paleoclimatic and paleoenvironmental changes in Amazonian lowlands over the last three millennia. Quaternary Science Reviews 279, 107383–107383. https://doi.org/10.1016/J.QUASCIREV.2022.107383

Deplazes, G., Lückge, A., Peterson, L.C., Timmermann, A., Hamann, Y., Hughen, K.A., Röhl, U., Laj, C., Cane, M.A., Sigman, D.M., Haug, G.H., 2013. Links between tropical rainfall and North Atlantic climate during the last glacial period. Nature Geoscience 6, 213–217. https://doi.org/10.1038/ngeo1712

Deschamps, P., Durand, N., Bard, E., Hamelin, B., Camoin, G., Thomas, A.L., Henderson, G.M., Okuno, J., Yokoyama, Y., 2012. Ice-sheet collapse and sea-level rise at the Bølling warming 14,600 years ago. Nature 483, 559–564. https://doi.org/10.1038/nature10902

Fornace, K.L., Hughen, K.A., Shanahan, T.M., Fritz, S.C., Baker, P.A., Sylva, S.P., 2014. A 60,000-year record of hydrologic variability in the Central Andes from the hydrogen isotopic composition of leaf waxes in Lake Titicaca sediments. Earth and Planetary Science Letters 408, 263–271. https://doi.org/10.1016/j.epsl.2014.10.024

Jaeschke, A., Rühlemann, C., Arz, H., Heil, G., Lohmann, G., 2007. Coupling of millennial-scale changes in sea surface temperature and precipitation off northeastern Brazil with high-latitude climate shifts during the last glacial period. Paleoceanography 22, 2006PA001391. https://doi.org/10.1029/2006PA001391

Johnson, H.L., Cessi, P., Marshall, D.P., Schloesser, F., Spall, M.A., 2019. Recent Contributions of Theory to Our Understanding of the Atlantic Meridional Overturning Circulation. JGR Oceans 124, 5376–5399. https://doi.org/10.1029/2019JC015330

Kanner, L.C., Burns, S.J., Cheng, H., Edwards, R.L., 2012. High-Latitude Forcing of the South American Summer Monsoon During the Last Glacial. Science 335, 570–573. https://doi.org/10.1126/science.1213397

Klose, J., Weber, M., Scholz, D., 2024. Central European warm phases recorded by episodic speleothem growth during MIS 3. Communications Earth and Environment 5. https://doi.org/10.1038/s43247-024-01863-0

Lawrence Edwards, R., Chen, J.H., Wasserburg, G.J., 1987. 238U234U230Th232Th systematics and the precise measurement of time over the past 500,000 years. Earth and Planetary Science Letters 81, 175–192. https://doi.org/10.1016/0012-821X(87)90154-3

Lea, D.W., Pak, D.K., Peterson, L.C., Hughen, K.A., 2003. Synchroneity of Tropical and High-Latitude Atlantic Temperatures over the Last Glacial Termination, Global Biogeochem. Cycles.

Lenters, J.D., Cook, K.H., 1997. On the origin of the Bolivian high and related circulation features of the South American climate. Journal of the Atmospheric Sciences 54, 656–677.

Liu, Z., Otto-Bliesner, B.L., He, F., Brady, E.C., Tomas, R., Clark, P.U., Carlson, A.E., Lynch-Stieglitz, J., Curry, W., Brook, E., Erickson, D., Jacob, R., Kutzbach, J., Cheng, J., 2009. Transient Simulation of Last Deglaciation with a New Mechanism for Bølling-Allerød Warming. Science 325, 310–314. https://doi.org/10.1126/science.1171041

Mcmanus, J.F., Francois, R., Gherardi, J.-M., Keigwin, L.D., Brown-Leger, & S., 2004. Collapse and rapid resumption of Atlantic meridional circulation linked to deglacial climate changes.

Meier, K.J.F., Jaeschke, A., Rethemeyer, J., Chiessi, C.M., Albuquerque, A.L.S., Wall, V., Friedrich, O., Bahr, A., 2022. Coupled Oceanic and Atmospheric Controls of Deglacial Southeastern South America Precipitation and Western South Atlantic Productivity. Front. Mar. Sci. 9, 878116. https://doi.org/10.3389/fmars.2022.878116

Moquet, J.S., Cruz, F.W., Novello, V.F., Stríkis, N.M., Deininger, M., Karmann, I., Santos, R.V., Millo, C., Apaestegui, J., Guyot, J.L., Siffedine, A., Vuille, M., Cheng, H., Edwards, R.L., Santini, W., 2016. Calibration of speleothem δ18O records against hydroclimate instrumental records in Central Brazil. Global and Planetary Change 139, 151–164. https://doi.org/10.1016/j.gloplacha.2016.02.001

Mulitza, S., Chiessi, C.M., Schefuß, E., Lippold, J., Wichmann, D., Antz, B., Mackensen, A., Paul, A., Prange, M., Rehfeld, K., Werner, M., Bickert, T., Frank, N., Kuhnert, H., Lynch-Stieglitz, J., Portilho-Ramos, R.C., Sawakuchi, A.O., Schulz, M., Schwenk, T., Tiedemann, R., Vahlenkamp, M., Zhang, Y., 2017. Synchronous and proportional deglacial changes in Atlantic meridional overturning and northeast Brazilian precipitation. Paleoceanography 32, 622–633. https://doi.org/10.1002/2017PA003084

Novello, V.F., Cruz, F.W., McGlue, M.M., Wong, C.I., Ward, B.M., Vuille, M., Santos, R.A., Jaqueto, P., Pessenda, L.C.R., Atorre, T., Ribeiro, L.M.A.L., Karmann, I., Barreto, E.S., Cheng, H., Edwards, R.L., Paula, M.S., Scholz, D., 2019. Vegetation and environmental changes in tropical South America from the last glacial to the Holocene documented by multiple cave sediment proxies. Earth and Planetary Science Letters 524, 115717–115717. https://doi.org/10.1016/j.epsl.2019.115717

Novello, V.F., Cruz, F.W., Moquet, J.S., Vuille, M., de Paula, M.S., Nunes, D., Edwards, R.L., Cheng, H., Karmann, I., Utida, G., Stríkis, N.M., Campos, J.L.P.S., 2018. Two Millennia of South Atlantic Convergence Zone Variability Reconstructed From Isotopic Proxies. Geophysical Research Letters 45, 5045–5051. https://doi.org/10.1029/2017GL076838

Novello, V.F., Cruz, F.W., Vuille, M., Stríkis, N.M., Edwards, R.L., Cheng, H., Emerick, S., De Paula, M.S., Li, X., Barreto, E.D.S., Karmann, I., Santos, R.V., 2017. A high-resolution history of the South American Monsoon from Last Glacial Maximum to the Holocene. Scientific Reports 7. https://doi.org/10.1038/srep44267

Orrison, R., Vuille, M., Smerdon, J.E., Apaéstegui, J., Leandro S Campos, J.P., Cruz, F.W., Eduarda Della Libera, M., 2022. South American Monsoon variability over the last millennium in paleoclimate records and isotope-enabled climate models. Climate of the Past. https://doi.org/10.5194/cp-2022-6

Ramirez, V.M., Cruz, F.W., Vuille, M., Novello, V.F., Stríkis, N.M., Cheng, H., Zhang, H.W., Bernal, J.P., Du, W.J., Ampuero, A., Deininger, M., Chiessi, C.M., Tejedor, E., Campos, J.L., Ait Brahim, Y., Edwards, R.L., 2023. Summer insolation controlled movements of Intertropical Convergence Zone during last glacial cycle in northern South America. Communications Earth and Environment 4. https://doi.org/10.1038/s43247-023-01124-6

Rasmussen, S.O., Bigler, M., Blockley, S.P., Blunier, T., Buchardt, S.L., Clausen, H.B., Cvijanovic, I., Dahl-Jensen, D., Johnsen, S.J., Fischer, H., Gkinis, V., Guillevic, M., Hoek, W.Z., Lowe, J.J., Pedro, J.B., Popp, T., Seierstad, I.K., Steffensen, J.P., Svensson, A.M., Vallelonga, P., Vinther, B.M., Walker, M.J.C., Wheatley, J.J., Winstrup, M., 2014. A stratigraphic framework for abrupt climatic changes during the Last Glacial period based on three synchronized Greenland ice-core records: refining and extending the INTIMATE event stratigraphy. Quaternary Science Reviews 106, 14–28. https://doi.org/10.1016/j.quascirev.2014.09.007

Santos, T.P., Shimizu, M.H., Nascimento, R.A., Venancio, I.M., Campos, M.C., Portilho-Ramos, R.C., Ballalai, J.M., Lessa, D.O., Crivellari, S., Nagai, R.H., Chiessi, C.M., Kuhnert, H., Bahr, A., Albuquerque, A.L.S., 2022. A data-model perspective on the Brazilian margin surface warming from the Last Glacial Maximum to the Holocene. Quaternary Science Reviews 286, 107557. https://doi.org/10.1016/j.quascirev.2022.107557

Scholz, D., Hoffmann, D.L., 2011. StalAge - An algorithm designed for construction of speleothem age models. Quaternary Geochronology 6, 369–382. https://doi.org/10.1016/j.quageo.2011.02.002

Shakun, J.D., Clark, P.U., He, F., Marcott, S.A., Mix, A.C., Liu, Z., Otto-Bliesner, B., Schmittner, A., Bard, E., 2012. Global warming preceded by increasing carbon dioxide concentrations during the last deglaciation. Nature 484, 49–54. https://doi.org/10.1038/nature10915

Steffensen, J.P., Andersen, K.K., Bigler, M., Clausen, H.B., Dahl-Jensen, D., Fischer, H., Goto-Azuma, K., Hansson, M., Johnsen, S.J., Jouzel, J., Masson-Delmotte, V., Popp, T., Rasmussen, S.O., Röthlisberger, R., Ruth, U., Stauffer, B., Siggaard-Andersen, M.-L., Sveinbjörnsdóttir, Á.E., Svensson, A., White, J.W.C., 2008. High-Resolution Greenland Ice Core Data Show Abrupt Climate Change Happens in Few Years. Science 321, 680–684. https://doi.org/10.1126/science.1157707

Stríkis, N.M., Chiessi, C.M., Cruz, F.W., Vuille, M., Cheng, H., De Souza Barreto, E.A., Mollenhauer, G., Kasten, S., Karmann, I., Edwards, R.L., Bernal, J.P., Sales, H.D.R., 2015. Timing and structure of Mega-SACZ events during Heinrich Stadial 1. Geophysical Research Letters 42, 5477. https://doi.org/10.1002/2015GL064048

Sulca, J., Vuille, M., Silva, Y., Takahashi, K., 2016. Teleconnections between the peruvian central andes and northeast Brazil during extreme rainfall events in austral summer. Journal of Hydrometeorology 17, 499–515. https://doi.org/10.1175/JHM-D-15-0034.1

Thiagarajan, N., Subhas, A.V., Southon, J.R., Eiler, J.M., Adkins, J.F., 2014. Abrupt pre-Bølling-Allerød warming and circulation changes in the deep ocean. Nature 511, 75–78. https://doi.org/10.1038/nature13472

Utida, G., Cruz, F.W., Santos, R.V., Sawakuchi, A.O., Wang, H., Pessenda, L.C.R., Novello, V.F., Vuille, M., Strauss, A.M., Borella, A.C., Stríkis, N.M., Guedes, C.C.F., Dias De Andrade, F.R., Zhang, H., Cheng, H., Edwards, R.L., 2020. Climate changes in Northeastern Brazil from deglacial to Meghalayan periods and related environmental impacts. Quaternary Science Reviews 250. https://doi.org/10.1016/j.quascirev.2020.106655

Vasconcelos, L.C., Cruz, F.W., Bernal, J.P., Campos, M.C., Piacsek, P., Campos, J.L., Zhang, H., Stríkis, N., Vuille, M., Utida, G., Millo, C., Edward, R.L., Cheng, H., 2025. The coupling between monsoon rainfall and Sea Surface Temperature in the subtropical South Atlantic during the Last Glacial Period. Global and Planetary Change 255, 105121–105121. https://doi.org/10.1016/j.gloplacha.2025.105121

Venancio, I.M., Shimizu, M.H., Santos, T.P., Lessa, D.O., Dias, B.B., Chiessi, C.M., Mulitza, S., Kuhnert, H., Tiedemann, R., Vahlenkamp, M., Bickert, T., Belem, A.L., Sampaio, G., Albuquerque, A.L.S., Nobre, C., 2020a. Ocean-atmosphere interactions over the western South Atlantic during Heinrich stadials. Global and Planetary Change 195, 103352. https://doi.org/10.1016/j.gloplacha.2020.103352

Venancio, I.M., Shimizu, M.H., Santos, T.P., Lessa, D.O., Portilho-Ramos, R.C., Chiessi, C.M., Crivellari, S., Mulitza, S., Kuhnert, H., Tiedemann, R., Vahlenkamp, M., Bickert, T., Sampaio, G., Albuquerque, A.L.S., Veiga, S., Nobre, P., Nobre, C., 2020b. Changes in surface hydrography at the western tropical Atlantic during the Younger Dryas. Global and Planetary Change 184, 103047. https://doi.org/10.1016/j.gloplacha.2019.103047

Vera, C., Higgins, W., Amador, J., Ambrizzi, T., Garreaud, R., Gochis, D., Gutzler, D., Lettenmaier, D., Marengo, J., Mechoso, C.R., Nogues-Paegle, J., Silva Dias, P.L., Zhang, C., 2006. Toward a unified view of the American monsoon systems. Journal of Climate 19, 4977–5000. https://doi.org/10.1175/JCLI3896.1

Vuille, M., Burns, S.J., Taylor, B.L., Cruz, F.W., Bird, B.W., Abbott, M.B., Kanner, L.C., Cheng, H., Novello, V.F., 2012. A review of the South American monsoon history as recorded in stable isotopic proxies over the past two millennia. Climate of the Past 8, 1309–1321. https://doi.org/10.5194/cp-8-1309-2012

Wang, X., Auler, A.S., Edwards, R.L., Cheng, H., Ito, E., Solheid, M., 2006. Interhemispheric anti-phasing of rainfall during the last glacial period. Quaternary Science Reviews, Critical Quaternary Stratigraphy 25, 3391–3403. https://doi.org/10.1016/j.quascirev.2006.02.009

Wang, X., Auler, A.S., Edwards, R.L., Cheng, H., Ito, E., Wang, Y., Kong, X., Solheid, M., 2007. Millennial-scale precipitation changes in southern Brazil over the past 90,000 years. Geophysical Research Letters 34. https://doi.org/10.1029/2007GL031149

Weber, M., Lugli, F., Jochum, K.P., Cipriani, A., Scholz, D., 2018. Calcium Carbonate and Phosphate Reference Materials for Monitoring Bulk and Microanalytical Determination of Sr Isotopes. Geostandards and Geoanalytical Research 42, 77–89. https://doi.org/10.1111/ggr.12191

Weber, M., Tacail, T., Lugli, F., Clauss, M., Weber, K., Leichliter, J., Winkler, D.E., Mertz-Kraus, R., Tütken, T., 2020. Strontium Uptake and Intra-Population 87Sr/86Sr Variability of Bones and Teeth—Controlled Feeding Experiments With Rodents (Rattus norvegicus, Cavia porcellus). Frontiers in Ecology and Evolution 8. https://doi.org/10.3389/fevo.2020.569940

Wong, M.L., Battisti, D.S., Liu, X., Ding, Q., Wang, X., 2023. A North–South Dipole Response of the South Atlantic Convergence Zone During the Mid-Holocene. Geophysical Research Letters 50, e2023GL105130. https://doi.org/10.1029/2023GL105130

Wong, M.L., Wang, X., Latrubesse, E.M., He, S., Bayer, M., 2021. Variations in the South Atlantic Convergence Zone over the mid-to-late Holocene inferred from speleothem δ18O in central Brazil. Quaternary Science Reviews 270. https://doi.org/10.1016/j.quascirev.2021.107178

Zhou, J., Lau, K.M., 2001. Principal modes of interannual and decadal variability of summer rainfall over South America. International Journal of Climatology 21, 1623–1644. https://doi.org/10.1002/joc.700

4.9 Supplementary Material II

Overprinted forcing of millennial events during the last deglaciation period in tropical South America

4.9.1 Supplementary text

For in-situ analysis of Sr isotopes, a Neptune Plus MC-ICP-MS was coupled with an ArF Excimer 193 nm laser ablation system at the Institute for Geosciences, Johannes Gutenberg University Mainz, Germany, following the methods described in Weber *et al.* (2017). Nitrogen was introduced into the sample gas line using an Apex Omega HF desolvator system. Data acquisition was performed as a line scan of 500 μm length perpendicular to the growth axis, a transition rate of 5 μm/s, a pulse repetition rate of 20 Hz and a spot size of 150 μm, resulting in a fluence of 5 J/cm^2. Accuracy was monitored using NanoSr (^{87}Sr/^{86}Sr = 0.70753 ± 0.00003, 1 SD, n = 21), JCp-1 (0.70917 ± 0.00001, 1 SD, n = 12) and JCt-1 (0.70915 ± 0.00001, 1 SD, n = 18), which all agree with the literature value (Weber *et al.*, 2018; Weber *et al.*, 2020). Sampling was made along the main axis with approximately 5 mm spacing, yielding a total of 87 analyses.

4.9.2 Supplementary Figures

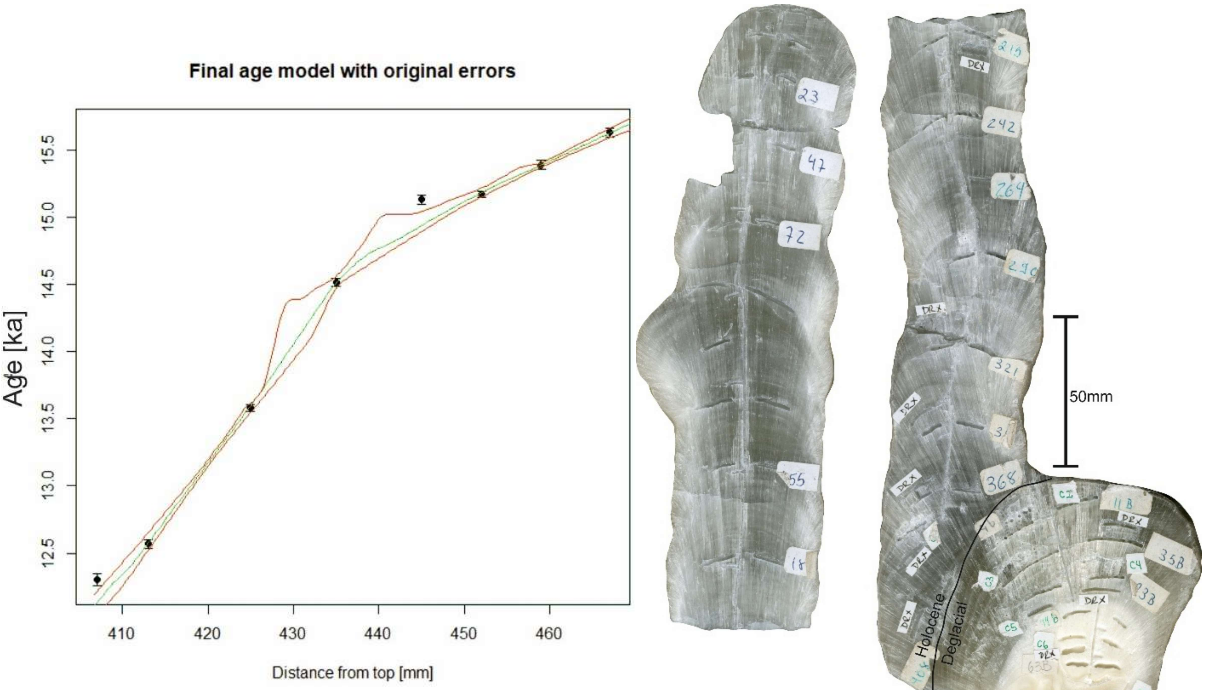

Supplementary Figure 4.1 – (left) SMT16 age-depth relationship for the deglacial period. Black points represent the MC-ICP-MS ^{230}Th-U ages with the corresponding 2σ uncertainties, the green line represents the age-model calculated by StalAge (Scholz and Hoffmann, 2011), and the red lines show the corresponding age-uncertainties (95% confidence interval). (right) SMT16 scan, evidencing the hiatus between the Holocene and Deglacial period.

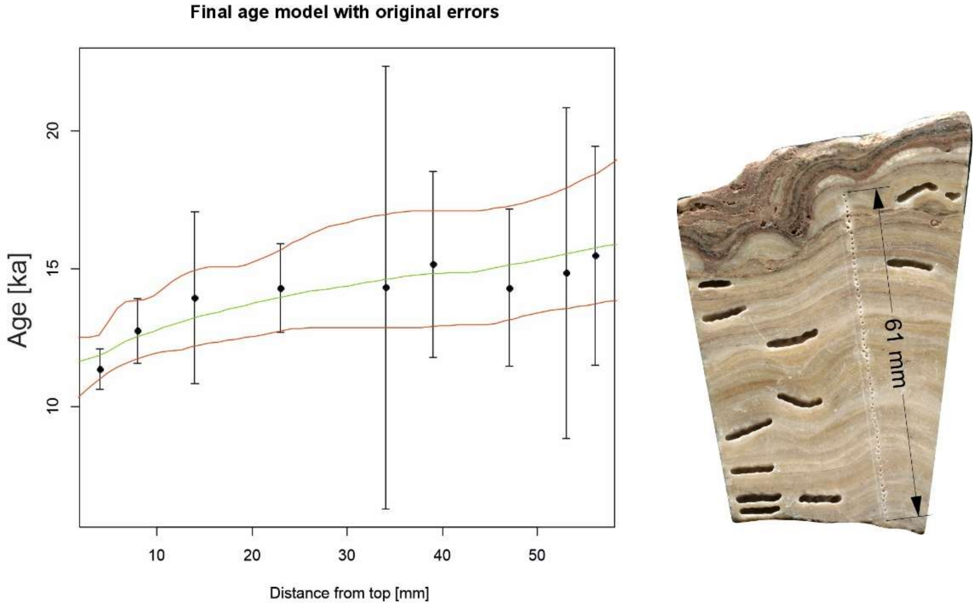

Supplementary Figure 4.2 – LVR6 age-depth relationship for the deglacial period. Black points represent the MC-ICP-MS ^{230}Th-U ages with the corresponding 2σ uncertainties, the green line represents the age-model calculated by StalAge (Scholz and Hoffmann, 2011), and the red lines show the corresponding age-uncertainties (95% confidence interval).

4.9.3 Supplementary Tables

Supplementary Table 4.1 - Analytical details of $^{87}Sr/^{86}Sr$ isotope ratio analyses

Instrument	Sample Type	Preparation/Collection	Analytical Details	Calibration/Standards
Neptune Plus MC-ICP-MS + LA	Speleothem (laser ablation)	In situ analysis, sampling along growth axis (5 mm spacing, 87 analyses). 500 µm-long line scan, 5µm/s transition rate.	Coupled with ArF Excimer 193 nm laser ablation system. Spot size: 150 µm, fluence: 5 J/cm², 20 Hz pulse repetition rate.	NanoSr ($^{87}Sr/^{86}Sr$: 0.70753 ± 0.00003); JCp-1 ($^{87}Sr/^{86}Sr$: 0.70917 ± 0.00001); JCt-1 ($^{87}Sr/^{86}Sr$: 0.70915 ± 0.00001).

Supplementary Table 4.2 - SMT16 ^{230}Th-U ages for the deglacial period.

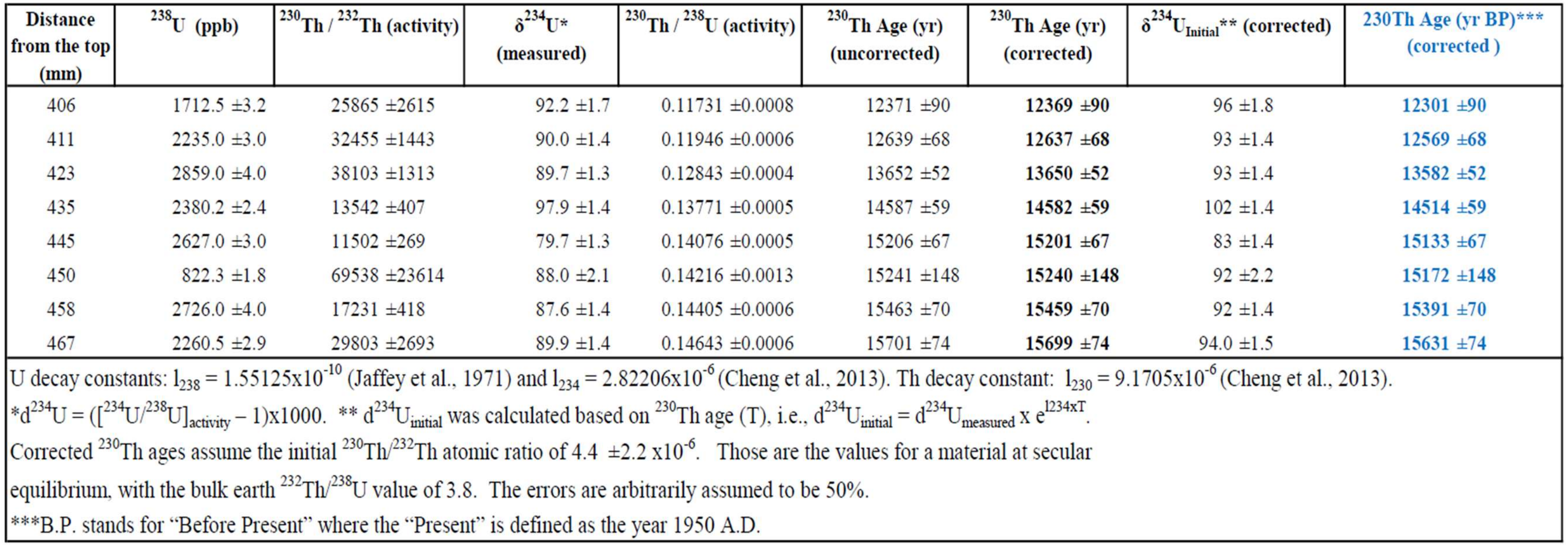

Distance from the top (mm)	^{238}U (ppb)	^{230}Th / ^{232}Th (activity)	δ^{234}U* (measured)	^{230}Th / ^{238}U (activity)	^{230}Th Age (yr) (uncorrected)	^{230}Th Age (yr) (corrected)	$\delta^{234}U_{Initial}$** (corrected)	230Th Age (yr BP)*** (corrected)
406	1712.5 ±3.2	25865 ±2615	92.2 ±1.7	0.11731 ±0.0008	12371 ±90	**12369 ±90**	96 ±1.8	**12301 ±90**
411	2235.0 ±3.0	32455 ±1443	90.0 ±1.4	0.11946 ±0.0006	12639 ±68	**12637 ±68**	93 ±1.4	**12569 ±68**
423	2859.0 ±4.0	38103 ±1313	89.7 ±1.3	0.12843 ±0.0004	13652 ±52	**13650 ±52**	93 ±1.4	**13582 ±52**
435	2380.2 ±2.4	13542 ±407	97.9 ±1.4	0.13771 ±0.0005	14587 ±59	**14582 ±59**	102 ±1.4	**14514 ±59**
445	2627.0 ±3.0	11502 ±269	79.7 ±1.3	0.14076 ±0.0005	15206 ±67	**15201 ±67**	83 ±1.4	**15133 ±67**
450	822.3 ±1.8	69538 ±23614	88.0 ±2.1	0.14216 ±0.0013	15241 ±148	**15240 ±148**	92 ±2.2	**15172 ±148**
458	2726.0 ±4.0	17231 ±418	87.6 ±1.4	0.14405 ±0.0006	15463 ±70	**15459 ±70**	92 ±1.4	**15391 ±70**
467	2260.5 ±2.9	29803 ±2693	89.9 ±1.4	0.14643 ±0.0006	15701 ±74	**15699 ±74**	94.0 ±1.5	**15631 ±74**

U decay constants: $l_{238} = 1.55125 \times 10^{-10}$ (Jaffey et al., 1971) and $l_{234} = 2.82206 \times 10^{-6}$ (Cheng et al., 2013). Th decay constant: $l_{230} = 9.1705 \times 10^{-6}$ (Cheng et al., 2013).

*$d^{234}U = ([^{234}U/^{238}U]_{activity} - 1) \times 1000$. ** $d^{234}U_{initial}$ was calculated based on ^{230}Th age (T), i.e., $d^{234}U_{initial} = d^{234}U_{measured} \times e^{l234xT}$.

Corrected ^{230}Th ages assume the initial $^{230}Th/^{232}Th$ atomic ratio of $4.4 \pm 2.2 \times 10^{-6}$. Those are the values for a material at secular equilibrium, with the bulk earth $^{232}Th/^{238}U$ value of 3.8. The errors are arbitrarily assumed to be 50%.

***B.P. stands for "Before Present" where the "Present" is defined as the year 1950 A.D.

Supplementary Table 4.3 – LVR6 ^{230}Th-U ages. The activity ratios were used to calculate the correction factor following the method of Budsky *et al.* (2019b).

Distance from the top (mm)	^{238}U (ppb)	^{230}Th / ^{232}Th (activity)	δ^{234}U* (measured)	^{230}Th / ^{238}U (activity)	^{230}Th Age (yr) (uncorrected)	^{230}Th Age (yr) (corrected-conventional)**	^{230}Th Age (yr) (corrected)***	$\delta^{234}U_{Initial}$**** (corrected)	^{230}Th Age (yr BP) (corrected)
4	162.7 ±1.0363	8.732 ±0.0238	1.2445 ±0.0017	0.1277 ±0.0057	12887 ±39	11765 ±544	11447 ±737	1.25278 ±0.0017	**11372 ±737**
8	96.7 ±0.6496	6.476 ±0.0292	1.2542 ±0.0028	0.1465 ±0.0089	15266 ±74	13489 ±873	12828 ±1182	1.26403 ±0.0029	**12753 ±1182**
14	85.1 ±0.5242	3.241 ±0.0146	1.2520 ±0.0070	0.1672 ±0.0230	20214 ±100	15557 ±2303	14034 ±3108	1.26332 ±0.0073	**13959 ±3108**
23	124.0 ±0.7554	5.443 ±0.0148	1.2402 ±0.0034	0.1617 ±0.0118	17578 ±51	15163 ±1159	14393 ±1610	1.25068 ±0.0035	**14318 ±1610**
34	85.5 ±0.5268	1.954 ±0.0055	1.2279 ±0.0155	0.1940 ±0.0547	29938 ±96	18651 ±5592	14402 ±8043	1.24020 ±0.0165	**14327 ±8043**
39	76.0 ±0.4617	3.256 ±0.0118	1.2248 ±0.0065	0.1767 ±0.0239	21901 ±88	16909 ±2536	15243 ±3368	1.23575 ±0.0071	**15168 ±3368**
47	63.9 ±0.4191	3.587 ±0.0155	1.2324 ±0.0057	0.1686 ±0.0203	20158 ±96	15970 ±2047	14385 ±2856	1.24308 ±0.0061	**14310 ±2856**
53	80.9 ±0.5001	2.292 ±0.0075	1.2334 ±0.0119	0.1890 ±0.0414	26621 ±99	18045 ±4355	14924 ±6003	1.24560 ±0.0127	**14849 ±6003**
56	85.9 ±0.5408	2.942 ±0.0118	1.2245 ±0.0079	0.1857 ±0.0285	23836 ±111	17849 ±2936	15556 ±3971	1.23612 ±0.0085	**15481 ±3971**

U decay constants: $l_{238} = 1.55125\text{x}10^{-10}$ (Jaffey et al., 1971) and $l_{234} = 2.82206\text{x}10^{-6}$ (Cheng et al., 2013). Th decay constant: $l_{230} = 9.1705\text{x}10^{-6}$ (Cheng et al., 2013).

*$\delta^{234}U = ([^{234}U/^{238}U]_{activity} - 1)\text{x}1000$. **** $\delta^{234}U_{initial}$ was calculated based on ^{230}Th age (T), i.e., $\delta^{234}U_{initial} = \delta^{234}U_{measured}\ \text{x}\ e^{l234\text{x}T}$.

** Conventionally detritus corrected ages ($^{232}Th/^{238}U$) = 1.25

*** Corrected ($^{234}U/^{238}U$) and ($^{230}Th/^{238}U$) activity ratios were calculated for various assumed detrital ($^{232}Th/^{238}U$)_d values, and the correction factor of 0.909 was chosen as the value minimizing age inversions (Budsky et al., 2019b).

The errors are arbitrarily assumed to be 50%.

Corrected ages are reported in B.P.(Before Present) where the “Present” is defined as 1950.

Chapter 5 – Manuscript III

Tropical South American temperature responses to rapid high-latitude climate shifts since the last deglaciation

Marcela Eduarda Della Libera[a,b]*; Julio Cauhy [a,b]; Valdir F. Novello[c]; Angela Ampuero[d]; Francisco W. Cruz Junior[d]; Nicolas M. Strikis[d]; Alfredo Martínez-García[b]; Hubert Vonhof[b]; Denis Scholz[a]

[a] Institut für Geowissenschaften, Johannes Gutenberg-Universität Mainz, Germany
[b] Max Planck Institut für Chemie, Mainz, Germany
[c] Institute of Geosciences, University of Brasília, Brasília – DF, Brazil
[d] Instituto de Geociências, Universidade de São Paulo, São Paulo-SP, Brazil

Paper in preparation - b

5.1 Abstract

Reconstructing past temperature variations is essential for understanding climate systems and improve projections for future climate changes. In central-east South America, modern warming has been shown to progress faster than global average. Nonetheless, paleotemperature records remain sparse in central South America, which limits our ability to evaluate the response of this region to rapid shifts in global forcings, such as during the deglacial period. Studies show that temperature evolution during the deglaciation was characterized by high-latitude rapid warming episodes associated with major reorganizations of the Atlantic Meridional Overturning Circulation (AMOC), which led to perturbations in inter-hemispheric heat distribution. Yet, how these perturbations affect temperatures in tropical South America and the thermal evolution of this region is still largely unknown. Here we present a new 15k-year paleotemperature reconstruction from a precisely dated speleothem collected in central-eastern Brazil. The temperature record is based on the glycerol dialkyl glycerol tetraether (GDGT) paleothermometer, revealing a total of 6.1°C±0.81 (2std = 0.81°C) of temperature shifts over the last 15k years. Our findings provide evidence of a non-linear temperature increase since the last deglaciation with abrupt warming and cooling events in response to high-latitude forcings, shifts in South Atlantic sea-surface temperatures (SSTs), and increases in atmospheric CO_2. Finally, we present a temperature gradient within central-east Brazil and show how paleoclimate models might underestimate rapid temperature changes.

5.2 Introduction

The last deglaciation period (~21-11.7 ka BP) is marked by several climate changes punctuated by abrupt, large-scale reorganizations of oceanic and atmospheric circulations (McManus *et al.*, 2004; Liu *et al.*, 2009). Prominent millennial-scale events during this interval include the Henrich Stadial 1 (HS1 – 18-14.7 ka BP), the Bølling–Allerød (BA – 14.7-12.9 ka BP) and the Younger dryas (YD - 12-9-11.7 ka BP), with each of these events recorded initially as rapid shifts in ice-core and marine sediment records (e.g. NGRIP members, 2004; Rasmussen *et al.*, 2014). These events are widely associated with perturbations of the Atlantic Meridional Overturning Circulation (AMOC) and changes in North Atlantic freshwater forcing (McManus *et al.*, 2004; Liu *et al.*, 2009; Clark *et al.*, 2001). These perturbations led to changes in oceanic circulation and heat distribution between the hemispheres, such as shifts in the Intertropical Convergence Zone (ITCZ), and consequent alterations in global temperatures and abrupt reorganizations of hydrological regimes (Wang *et al.*, 2006; Shakun *et al.*, 2012; Chiessi *et al.*, 2015). Following the YD, the Holocene (from ~11.7 ka BP to the present) established boundary conditions that are often characterized as relatively free of abrupt climate changes, although it exhibits notable regional variability and multiple climatic excursions (e.g. Bernal *et al.*, 2016; Stríkis *et al.*, 2011; Orrison *et al.*, 2022)

Variations in AMOC have a significant impact on the climate of South America. AMOC-forced changes in sea surface temperature (SSTs) patterns in the South Atlantic Ocean trigger shifts in atmospheric circulation (Chiessi *et al.*, 2015). The upper-level oceanic circulation at the Brazilian margin (western South Atlantic) is dominated by a northward-flowing current, the North Brazil current (NBC), and a southward-flowing current, the Brazilian current (BC) (Fig. 5.1 - Chiessi *et al.*, 2015; Santos *et al.* 2022). Both currents originate at ~10°S, where the southern South Equatorial Current (sSEC) bifurcates and feeds both currents (Chiessi *et al.*, 2015). When AMOC weakens, less warm water is carried northward from the South Atlantic into the Northern Hemisphere, resulting in a relative warming of the South Atlantic basin and cooling of the North Atlantic, which is a classic manifestation of the “bipolar seesaw” mechanism (Chiessi *et al.*, 2015; Meier *et al.*, 2022). This SST dipole alters the zonal energy balance across the equator, driving a southward displacement of the ITCZ, enhancing moisture input over tropical South America (Vuille *et al.*, 2012; Bernal *et al.*, 2016).

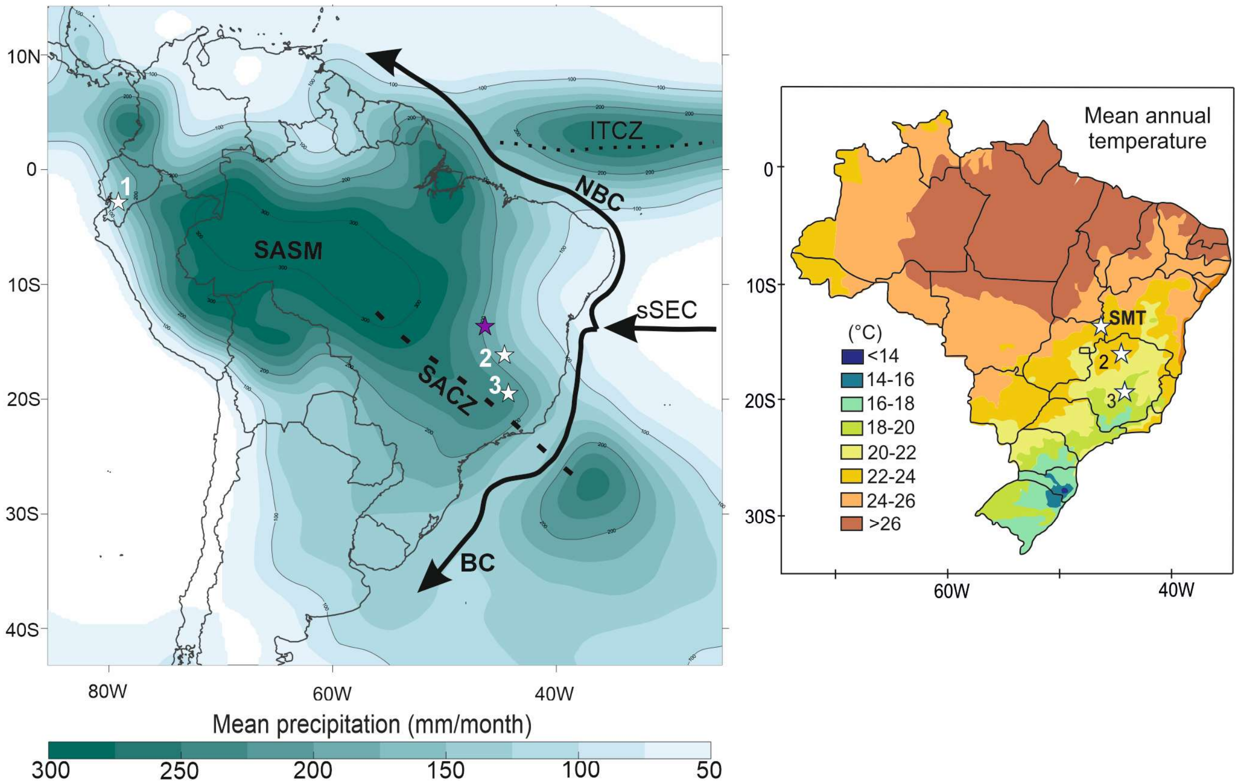

Figure 5.1 – (left) Map of South America with monthly mean austral summer precipitation during peak monsoon season (DJF) from Global Precipitation Measurement Mission (GPM, 2001-2020) (Huffman *et al.*, 2019). The main summer climate features over the continent are indicated as SASM (South American Summer monsoon) and SACZ (South Atlantic Convergence Zone), with the mean location of the SACZ represented by the dashed line. Black arrows represent the direction of flow of the southern South Equatorial Current (sSEC), North Brazilian Current (NBC) and the Brazilian Current (BC). Stars represent the locations of paleoclimate records discussed in the text. The purple star represents São Mateus cave (this study); 1) Lake Llaviucu (Zhao *et al.*, 2024); 2) Lapa Sem Fim cave (Stríkis *et al.*, 2015); 3) Rei do Mato cave (Ampuero *et al.*, under review). The climatological DFJ location of ITCZ is represented by the dottet line. (right) Mean annual temperature in Brazil based on Alvares *et al.* (2013), with the starts indicating São Mateus (SMT), Lapa Sem Fim (2), and Rei do Mato (3) caves.

Despite the already great effort to understand the role these ocean circulation changes play in the South American hydroclimate, little is known about the temperature effects in tropical continental areas during the deglaciation. Only a few continental temperature records are available (e.g. Stute *et al.*, 1995; Palacios *et al.*, 2020; Zhao *et al.*, 2024), especially for the Brazilian low latitudes, which limits our understanding of land–ocean coupling and regional thermal gradients. In general, these records are spatially very distant and reveal distinct magnitudes of deglacial warming, such as a ~5.4°C increase from the last glacial maximum to the Holocene in Northeastern Brazil (Stute *et al.*, 1995) and a ~4°C increase in Ecuadorian lakes for the same period (Zhao *et al.*, 2024). Additionally, one of the most recent paleotemperature reconstructions in lowland South America, Rei do Mato cave temperature record in central-east Brazil (Ampuero *et al.*, under review), shows a ~6.3°C warming from the glacial to the Holocene. All records broadly capture the main structure of deglacial temperature change, but uncertainties persist regarding the true amplitude, spatial coherence, and millennial-scale variability of warming across tropical South America.

Research in central-eastern Brazil, especially in the Cerrado savanna region, indicates that post-industrial temperature rise has exceeded the global average, which brings attention to the region's sensitivity to continental thermal anomalies and the importance of establishing long-term temperature records in this region (Stríkis *et al.*, 2024; Reboita *et al.*, 2024). In this context, we present a new 16 k year paleotemperature reconstruction for central-eastern Brazil based on speleothem glycerol dialkyl glycerol tetraether (GDGT) paleothermometry (Baker *et al.*, 2019; Blyth & Schouten, 2013). We show how surface temperature in this region responded to major climate shifts during the deglacial and Holocene periods and, in comparison with Rei do Mato record, we investigate the evolution of temperature gradient across central-eastern Brazil.

5.3 Study site, sample and current cave temperature

São Mateus cave (13.67° S; 46.37° W, 623 m a.s.l.) is located at the State Park of Terra Ronca (PETER), Goiás state, Central Brazil. The cave is developed in Neoproterozoic karstified dolostone interbedded with limestones of the Sete Lagoas Formation, Bambuí Group (Dardenne, 1987; Auler and Farrant, 1996). The climate at PETER is tropical semi-humid with a distinct wet–dry seasonality between summer and winter. Mean annual precipitation is 1,428 mm yr^{-1} (1974–2023; São Vicente station, ~14 km from São Mateus Cave), with about 80% of rainfall occurring between October-April during the summer monsoon. Mean surface annual temperature is 24 °C, ranging from 22.5 °C in winter to 25.8 °C in summer (Moquet *et al.*, 2016). The present-day local vegetation is generally characterized as Cerrado (Brazilian savanna), more specifically as a dry deciduous forest, which means this vegetation loses significant arboreal cover during the dry season (winter).

The stalagmite used in this study, SMT16, was collected at the Setecentos Hall, located ca. 150 m away from the cave entrance, and ca. 30 m above the modern level of the São Mateus River. SMT16 is a ~470 mm-long aragonite stalagmite without signs of recrystallization or dissolution, (Supp. Fig. 5.1). The sample is divided between a long (0-404mm) and a short (406-467mm) section, marked by a shift in the dripping point and by a thin white layer (Supp. Fig. 5.1). Temperature in Setecentos Hall is constant throughout the year, with a mean of 23.8°C and only 0.2°C variation, and a constant relative humidity of 100% (Governo do Estado de Goiás, 2016).

5.4 Methods

The chronology of SMT16 is built on with 26 ages obtained via the ^{230}Th-U dating method with data collected via multi-collector inductively coupled plasma mass spectrometry following the methods described in Cheng *et al.* (2013a). The age-depth model was established by StalAge (Scholz & Hoffmann, 2011). A more detailed description of the methods used for the determination of SMT16 stalagmite is already described at Della Libera *et al.* (2026, in prep-a).

To reconstruct the cave temperatures, we used the TEX_{86} index (TetraEther index of 86 carbon atoms), which is calculated based on the relative abundances of the different isoprenoids of the GDGT lipids (Schouten *et al.* 2002). The method of analysis for the determination of the relative amounts of GDGTs lipids in SMT16 was based on an adaptation of the methods proposed by Blyth and Schouten (2013). Approximately 1 g of sample was collected from SMT16 at ~2cm depth intervals, resulting in 29 samples over the length of the record, except at the lower part of the stalagmite, where a stacked collection was made to obtain more detailed analysis. The samples were collected in chips and later pulverized for analysis. After pulverization, GDGTs were extracted chemically (a detailed explanation can be found in Supplementary Text 1). The external analytical precision was assessed using a speleothem standard in every batch prepared from a flowstone material from Scladina Cave, Belgium. The extracts were analyzed using an Agilent 1260 Infinity high-performance liquid chromatography (HPLC) coupled to an Agilent 6130 single-quadrupole MS with C_{46}-GDGT as an internal standard, using a small adaptation of the method proposed by Hopmans *et al.* (2016), as described Auderset *et al.* (2020). Individual GDGTs were quantified from ion chromatograms, and the TEX_{86} index (TetraEther index of 86 carbon atoms) was calculated from the relative abundances of GDGT-1, GDGT-2, GDGT-3, and crenarchaeol isomer (Schouten *et al.* 2002). Cave temperature estimates were obtained by using the recent calibration proposed by Baker *et al.* (2019):

$$\text{Cave air T} = -7.34 + 34.64 * TEX_{86}$$

An average cave *T* of 14.8°C with a standard deviation of 0.4 °C (1 s.d., n=22) was obtained from the Scladina Cave standard. The uncertainties shown in Fig. 2 are 2 s.d. (0.8 °C) based on the measurements of the external analytical precision of the Scladina standard. According to Baker *et al.* (2019), the general TEX86 calibration uncertainty is ~1°C (2 s.d.), which primarily affects absolute values and not the sample-to-sample variability.

5.5 Results

The SMT16 stalagmite covers the period between -0.024 kyr BP and 15.71 kyr BP. The long section of the speleothem covers the Holocene period constrained by 18 ^{230}Th/U-ages presenting an average 2σ-uncertainty of 0.23 % (more details in Della Libera et al., accepted). The short section covers the deglacial period from 12.10 to 15.71 kyr BP, with an overall 2σ ^{230}Th-U age uncertainty of 0.4% or ± 65 yr based on the 8 ^{230}Th-U ages that constrain this section (more details in Della Libera et al, in prep.-a).

The SMT16 TEX86 record covers the period between -0.03 (+16, -17) and 15.03 (+101, -44) kyr BP, with ranging temperatures between 25.1 °C and 19 °C (Fig. 5.2b). The mean temperature over the 15-kyr record is 22.7 °C. Mean temperature during the deglacial period is 23.1°C and 22.6 °C during the Holocene. Prior to the beginning of the BA, temperature is stable at around 23 °C before rapidly increasing to 23.5 °C at the onset of the BA (~14.86 -14.83 BP). This followed by a 1.9 °C decline in temperature until 13 kyr BP. The transition from the BA to the YD at 12.9 kyr BP is characterized by a rapid increase from 21.7 to 24.1 °C. After the hiatus, the early Holocene is marked by the lowest temperatures of the record, 19°C, at ~10.71 kyr BP, followed by a gradual increase until ~7.37 kyr BP. From this point towards the present, temperatures are stable at ~23.7 °C, punctuated by a transient increase of temperature to 25.1°C at ~2.07 kyr BP.

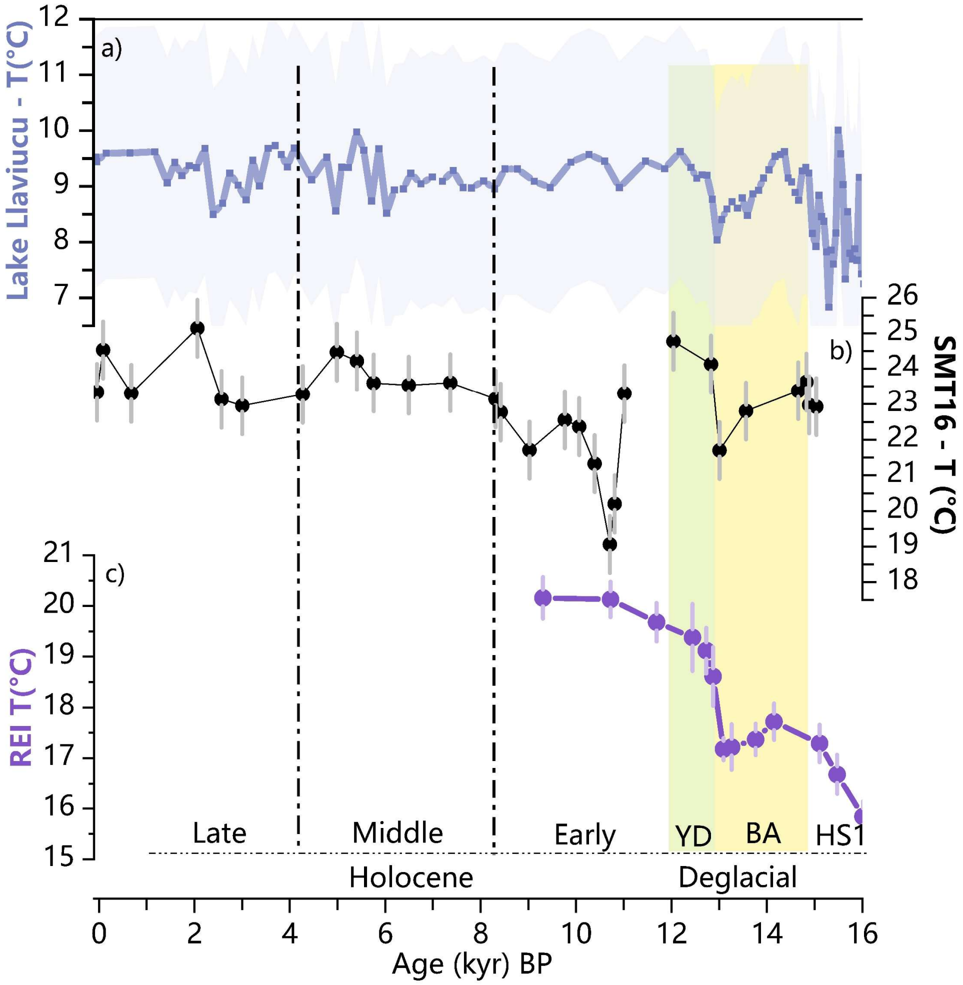

Figure 5.2 - Comparison between proxy-based temperature reconstructions in South America. a) Laguna Llaviucu derived from organic biomarkers (Zhao *et al.*, 2024); b) SMT16 derived from organic biomarkers, with error bars of 0.8°C (2s.d.) (this study); Rei do Mato microthermometry temperature (Ampuero *et al.*, under review).

5.6 Discussion

5.6.1 Regional temperature and comparisons withTraCE21kii model simulation

The SMT16 temperature reconstruction reveals distinct variations that align with major deglacial and Holocene climatic events. Temperatures were relatively high during the end of HS1, followed by a short-lived warming at the onset of the BA. This period was then marked by a progressive cooling trend, culminating in an abrupt temperature increase at the onset of the YD (Fig.5.2b). During the YD, temperatures reached values comparable to those observed during the warmest phases of the Holocene, highlighting strong regional sensitivity to abrupt climate shifts.

The timing and structure of temperature variations observed in the SMT16 record is remarkably consistent with other continental paleotemperature records from tropical South America (Fig. 5.2). Similar patterns appear in Rei do Mato cave record (REI - 19.48 °S; 44.17 °W - Ampuero *et al.*, under review), located ~600 km south of São Mateus cave (Fig. 5.2c), and in Lake Llaviucu record (2.8 °S; 79.1 °W - Zhao *et al.*, 2024) in the Ecuadorian Andes (Fig. 5.2a). Lake Llaviucu shows 1.4°C of warming during the final phase of HS1, in agreement with the 0.7°C rise recorded in SMT16. Although Rei do Mato record does not cover the very end of HS1, its 0.4°C increase between 15.1–14.1 ka BP is comparable in magnitude with our record. The subsequent cooling during the BA is noticeably stronger at SMT16 (1. 7°C) in comparison with REI (0.5 °C), presenting more than triple the decrease, and showing a similar amplitude decline as the Lake Llaviucu record (1.6 °C). In contrast, the YD warming shows closer agreement between the two central-eastern Brazilian sites. SMT16 records a 3.1 °C rise, similar to the 2.2 °C increase at REI, both exceeding the more moderate 1.6 °C warming observed at Lake Llaviucu. Together, these records reveal a broadly synchronized pattern of deglacial temperature change across tropical South America, yet with varying amplitudes that likely reflect distinct regional responses to large-scale atmospheric circulation as well as hydrological shifts or local effects on proxy-to-proxy sensitivity.

Although São Mateus and Rei do Mato caves are located within the same central-eastern Brazilian region, a clear temperature gradient exists between them. Currently, São Mateus mean surface annual temperature is on average 2.7 °C warmer than Rei do Mato. Yet, during the deglacial period this difference was ~5.1°C, indicating a steeper thermal contrast in the past. Such a pronounced gradient raises questions about whether large-scale climate models can capture the spatial heterogeneity of temperature across this region. Ampuero *et al.* (under review) showed that the transient TraCE21kii model simulation (He and Clark, 2022) reproduces both the timing and magnitude of temperature changes at REI record with moderate skill (Fig. 5.3c). In contrast, the simulation run for the São Mateus location fails to capture the overall structure of our record, with the simulation producing a warmer BA relative to both HS1 and the YD (Fig. 5.3a). The only feature the simulation reproduces is the sharp BA-YD transition with a 1.3 °C positive excursion, which occurs in phase but with smaller amplitude compared to the SMT16 reconstruction. Still, it is a brief warming followed by a decrease in temperatures, not reproducing the continued temperature increase during the YD (Fig. 5.3a). In fact, both the TraCE21Kii simulation run for

Lapa Sem Fim cave (LSF - Stríkis *et al.*, 2015 – Fig. 5.3b), which sits ~300 km south of São Mateus, and for Rei do Mato cave, have a more similar structure as our SMT16 paleotemperature (Fig. 5.3b, c). Still, the range of temperatures are much higher in the SMT16 record, which is indeed captured by the TraCE21kii run for São Mateus cave site (Fig. 5.3a). While the model reproduces a spatial thermal gradient between São Mateus and Rei do Mato caves, it underestimates the full amplitude between the two sites (~3.5 °C) in comparison to our reconstruction (~5.1 °C). Therefore, the stronger deglacial temperature gradient between the two sites likely reflects location-specific and atmospheric circulation effects that the model's coarse spatial resolution cannot fully resolve.

During the early Holocene, the SMT paleotemperature record shows a sharp cooling reaching its minimum temperature of the entire record of 19°C at 10.7 BP. A slight cooling is also observed at Lake Llaviucu, whereas no comparable change appears in the REI temperature record. Yet, the pronounced deglacial thermal gradient across central-eastern Brazil disappears, as São Mateus temperatures drop to values similar to those observed at Rei do Mato (Fig. 5.2). The early-Holocene cooling is followed by a steady recovery, with temperatures rising until ~7.3 ka BP and remaining above the long-term mean of 23 °C thereafter.

This early Holocene evolution is again not reproduced by the São Mateus TraCE21kii model, which lacks the pronounced cooling and subsequent recovery observed in our reconstruction. However, the simulation for the nearby LSF shows a broadly similar pattern to the SMT16 record, though the changes are expressed more smoothly (Fig. 5.3b). For the mid- to late Holocene, the São Mateus TraCE21kii model presents a closer agreement with the SMT16 temperature record compared to the deglacial period, even though it infers lower temperatures after the early Holocene as compared to our record. This suggests that the model better captures large-scale regional dynamics than localized responses. The persistent mismatch between modeled and reconstructed temperatures demonstrates the importance of local boundary conditions, such as land–atmosphere feedbacks, regional moisture balance, and oceanic influences from the adjacent western Atlantic in modulating the thermal evolution of eastern Brazil (Gentine *et al.,* 2019; Cabrera *et al.,* 2025). These regional processes, and their interaction with large-scale climatic forcings, are explored in the following section.

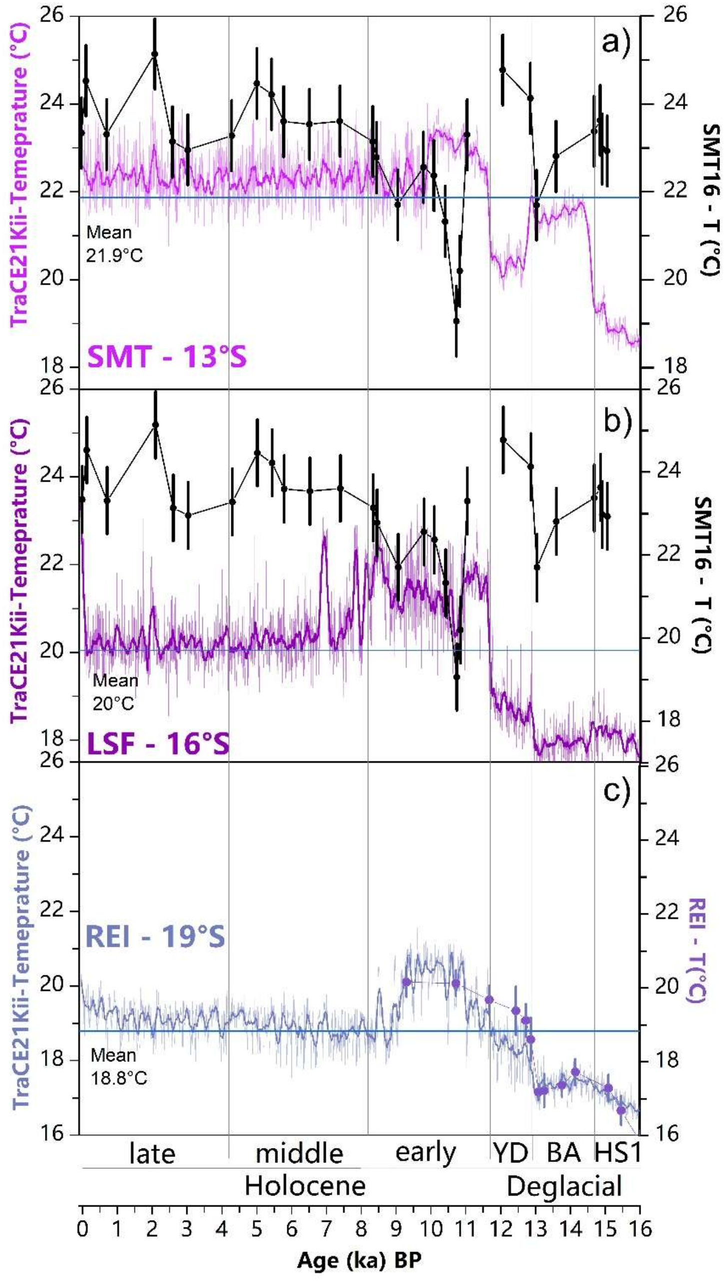

Figure 5.3 - Comparison between temperature reconstructed from São Mateus and surface temperature simulations from TraCE21kii (He and Clark, 2021) from three different sites. a) Temperature evolution at São Mateus cave (black circles) and TraCE21kii decadal averages (thin light pink) and a 250-year smoothing window (darker pink). b) same as a), but for Lapa Sem Fim cave location (16°09'S, 44°36'W). c) same as a), but for Rei do Mato cave location (19°48'S; 44°17'W). In all the plots, the blue line is the mean temperature value of the simulation for the entire period.

5.6.2 Temperature and local $\delta^{18}O$ response to high-latitude forcings

To assess the local climatic dynamics involving temperature, atmospheric circulation, and hydrological variability, we compare our temperature record with a $\delta^{18}O$ reconstruction from the same stalagmite previously studied by Della Libera *et al.* (accepted; in prep-a – Fig. 5.4d). The overall structure of the SMT16 temperature record shows cooling during the BA and warming in the YD, concomitant with high $\delta^{18}O$ values in SMT16 during the BA, followed by a sharp decrease at the onset of the YD around 12.9 ka BP (Fig. 5.4d). According to Della Libera (in prep-a) and Bao *et al.* (2023a,b), $\delta^{18}O$ variations in central-east Brazil during the deglacial period are strongly modulated by the amount effect. This relationship suggest that drier and comparatively colder conditions prevailed during the BA, whereas the YD was characterized by enhanced convection and warmer conditions, with temperature approaching those of the Late Holocene. This pattern is in agreement with the inter-hemispheric heat distribution associated with AMOC/Atlantic changes during this period (Fig. 5.4a). Relatively strong northward heat transport into the Northern Hemisphere (enhanced AMOC) during the BA corresponds to a northward displacement of the ITCZ and reduced moisture delivery from the southern Atlantic easterly flow into eastern Brazil (Zilli *et al.* 2019; Bao *et al.* 2023; Wong *et al.* 2023; Della Libera, in prep-a). As São Mateus sits closer to the influence domain of the North Brazil Current (NBC)/tropical western South Atlantic circulation (Fig. 5.1), the low SST observed in the NBC during this period further corroborates the low temperatures seen in SMT16 (Fig. 5.4c - Venancio *et al.* 2019, 2020; Chiessi *et al.* 2015: Santos *et al.* 2022). The opposite scenario during the YD, with reduced AMOC strength, results in heat storage at the western South Atlantic, increasing the strength of the easterlies and enhancing moisture input in the area, strengthening SACZ (Chaves and Nobre, 2004; Venancio *et al.* 2019, 2020: Meier *et al.*, 2022).

Moreover, together with the AMOC variations, these BA-YD variations are concomitant with the Antarctic cold reversal (ACR), a well-documented Antarctic cooling event centered roughly 14.5–12.9 ka BP, concomitant with the BA (Fig. 5.4b). This provides an extratropical southern-hemisphere background that would reinforce the south-to-north thermal gradient and modulate mid-latitude easterlies and Southern Ocean heat release during the BA interval (WAIS, 2013). Therefore, the BA–YD oscillation observed at São Mateus and Rei do Mato (Fig. 5.4d) paleotemperature records are temporally coeval with the Antarctic temperatures shifts, CO_2 variations (Fig. 5.4b), and NBC temperatures shifts (Fig. 5.4c). These combined changes likely impacted Southern Ocean circulation with significant changes in South Atlantic SSTs and atmospheric circulation (Venancio *et al.* 2019, 2020; Santos et al, 2022).

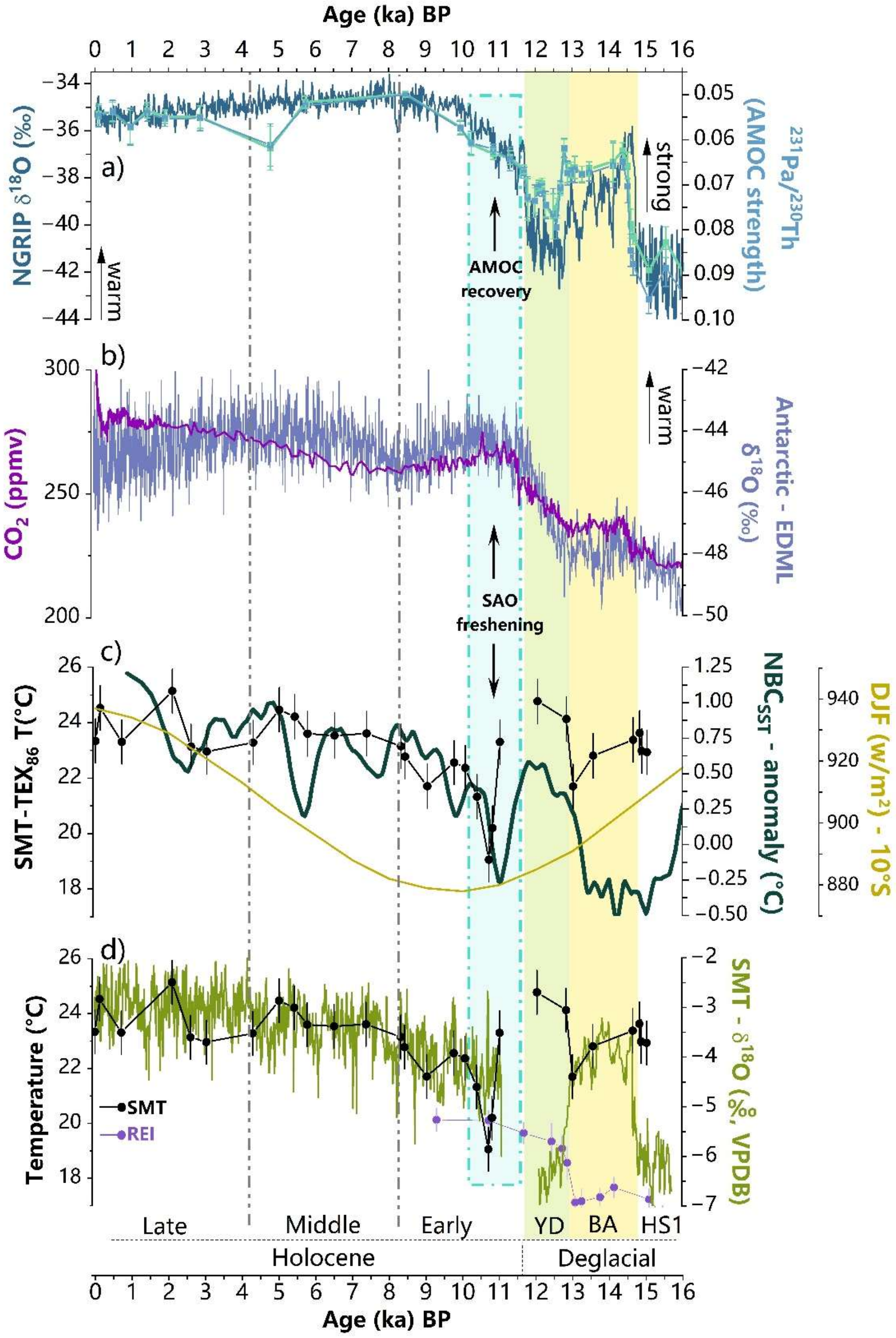

Figure 5.4 - Comparison of SMT temperature and oxygen isotope records with Rei do Mato temperature reconstructions and forcings. a) North Greenland Ice Core Project (NGRIP members, 2004) $\delta^{18}O$ record (dark blue line), OCE326-GGC5 ^{231}Pa / ^{230}Th-based record of the strength of the Atlantic meridional overturning circulation (McManus *et al.*, 2004) (light blue and green lines with squares). b) Antarctic records of CO_2 concentration composite (Köhler *et al.*, 2017) and temperature difference from present at EDML site (Lemieux-Dudon *et al.*, 2006). c) SMT TEX_{86} temperature reconstruction (black circles and line – this study),

insolation curve for DJF at 10°S (Berger and Loutre, 1991-yellow line), North Brazilian Current (NBC) sea surface temperature (SST) anomaly based on a stack composite of 6 marine sediment cores (Santos *et al.*, 2022 – green line); d) SMT TEX$_{86}$ temperature reconstruction (black circles and line – this study), SMT16 δ^{18}O record (green line, Della Libera *et al.*, accepted), Rei do Mato cave microthermometry-based temperature reconstruction (Ampuero *et al.*, under review – purple circles). The dashed and shaded blue rectangle indicates the cooling event at SMT16 temperature record.

Temperature shifts during the BA and YD events were much more pronounced at the São Mateus site than at Rei do Mato. A process that could explain this difference is the influence of ocean currents influencing each site. São Mateus sits closer to the domain of the NBC/tropical western Atlantic circulation (10 °S), whereas Rei do Mato is more influenced by the BC)/subtropical South Atlantic system as it sits further south (Santos *et al.*, 2022; Chiessi *et al.*, 2015). Paleotemperature and SST compilations for the Brazilian margin show distinct, spatially variable SST responses across the NBC–BC transition that track changes in ocean transport and upper-ocean heat content (Meier *et al.*, 2022; Santos *et al.*, 2022, Chiessi *et al.*, 2015; Barh *et al.*, 2018). Some of the deglacial studies for these currents show that the NBC region experiences larger temperature swings than the BC region during both the BA and the YD due to the AMOC bipolar seesaw between the northern and southern Atlantic oceans (McManus *et al.*, 2004; Chiessi *et al.*, 2015; Bahr *et al.* 2018; Santos *et al.*, 2022). For instance, during the YD, temperature records from the tropical NBC domain present a 3–5 °C warming, whereas reconstructions from the BC present a spatial heterogeneity, but with all pointing to a ~1-1.5 °C increase (Chiessi *et al.*, 2015; Venancio *et al.*, 2020; Santos *et al.*, 2022). This difference is in accordance with the temperature differences observed between São Mateus and Rei do Mato sites, which increased by a total of 3.1 °C and 2.2 °C, respectively during the BA-YD transition. This suggests that the western South Atlantic temperatures might have a significant influence in temperatures over the continent, as suggested previously (Swingedouw *et al.*, 2009; Marson *et al.*, 2014).

Throughout the Holocene, the overall increasing trend in São Mateus paleotemperature record follows the increase in SMT16 δ^{18}O values (Fig. 3d). In contrast to the deglacial period, when SMT16 δ^{18}O variations were primarily driven by the amount effect (Della Libera *et al.*, in prep-a), the major changes in δ^{18}O values in SMT16 during the Holocene reflect shifts in moisture source and atmospheric circulation (Della Libera *et al.*, accepted). Higher values are associated with precipitation coming directly from the South Atlantic Ocean, i.e., the easterlies, whereas lower values are associated with the offshore monsoonal pathway, which runs over a much longer continental stretch before reaching the area, depleting the oxygen and potentially bringing less moisture compared to the easterlies (Ampuero *et al.* 2020; Bao *et al.*, 2023; Della Libera *et al.*, accepted). Therefore, this isotope–temperature relationship suggests that Holocene temperature changes in eastern Brazil were closely linked to reorganizations of regional circulation patterns and moisture sources.

The pronounced early Holocene cooling at São Mateus at 10.7 ka BP (Fig. 5.4d, light blue rectangle) marks the coldest point of the SMT16 record (19 ºC). At this point, the temperatures drop to similar values as REI, extinguishing the earlier temperature gradient between them (Fig. 5.4d). Concomitantly, the NBC experiences its largest temperature anomaly of the last 16 ka, showing a strong agreement with the temperature decline at São Mateus (Fig. 5.4c). The coherence between NBC_{SSTs} and São Mateus indicate that they are either influenced by the same mechanism or that the NBC_{SSTs} have indeed a strong influence over central-eastern Brazil temperatures. The anomaly in NBC_{SST} is coeval with a major Antarctic freshwater release between 11.6–10.2 ka (Golledge *et al.*, 2014; Santos *et al.* 2022). Such freshening in the South Atlantic Ocean had a strong influence in cooling the upper South Atlantic and reduce SSTs (>1 °C) and air temperatures (>1–2 °C) along the Brazilian margin (Swingedouw *et al.*, 2009; Marson *et al.*, 2014; Santos *et al.*, 2022). This increase in freshwater coincides with peak Antarctic $\delta^{18}O$ values and elevated atmospheric CO_2 concentrations (Fig. 5.4b), which played a key role in amplifying global temperature responses during the deglaciation through ocean–atmosphere feedbacks (Shakun *et al.* 2012). Moreover, the AMOC recovery led to a warming of the North Atlantic Ocean, which is in constant increase during the early Holocene as observed from the NGRIP record (Fig. 5.4a), enhancing the northward heat transport (McManus *et al.* 2004). Therefore, all these mechanisms were at play at the time of the cooling event at São Mateus. Yet, this pronounced cooling is not expressed in the SMT16 $\delta^{18}O$ record (Fig. 5.4d), suggesting a temporary decoupling between local temperature and atmospheric circulation, likely reflecting a shift in moisture source or precipitation regime.

After this brief cooling and subsequent stabilization of AMOC, the increasing austral summer insolation seems to be the main forcing behind the moderate constant rise in temperatures in São Mateus region throughout until the middle Holocene (Fig. 5.4c). The continuous synchronic warming trend between the SMT16 temperature, the NBC_{SST} stack, and the increase in SMT16 $\delta^{18}O$ values reflect a reinforced ocean–atmosphere coupling along the western South Atlantic (Santos *et al.*, 2022; Meier *et al.* 2022). The increasing insolation likely led to an already known southward shift of ITCZ, a strengthening of the SASM/SACZ, and enhanced oceanic heat transport via easterlies into central-eastern Brazil (Haug *et al.* 2001; Bernal *et al.*, 2016; Wong *et al.*, 2023;

Della Libera *et al.*, accepted), which led the São Mateus site to transition into the persistently warmer conditions that characterize the late Holocene. Ultimately, the paleotemperature record of SMT16 shows how regional temperature evolution in eastern Brazil was mostly driven by high-latitude perturbations in the deglaciation and by the gradual dominance of insolation and oceanic forcing during the Holocene, marking the establishment of modern tropical South Atlantic climate dynamics.

5.7 Conclusions

Our 15-kyr paleotemperature reconstruction from São Mateus cave reveals rapid temperature shifts during the deglacial and early Holocene period. Overall, the new SMT16 paleotemperature record evidences a coupled ocean–atmosphere response to interhemispheric heat redistribution driven by variations in AMOC strength and Antarctic temperatures. A 1.7 °C cooling during the BA/ACR period and an abrupt 3.1 °C warming at the onset of the YD follows Antarctica temperature trends and major AMOC transitions, linking interhemispheric heat redistribution to tropical continental responses. These shifts likely altered the ITCZ position and the intensity of the easterlies, with higher temperatures corresponding to wetter conditions at São Mateus.

While transient TraCE-21Kii simulations reproduce general deglacial trends and the timing of the BA–YD transition, they underestimate both the amplitude of temperature changes and the thermal gradient between sites within central-east Brazil. This suggests that regional oceanic and atmospheric processes (e.g., NBC/BC variability, SST gradients, and land–atmosphere feedbacks) are not fully resolved. Finally, the SMT16 paleotemperature record reveals the most prominent cooling of 4.3°C of the last 15-kyr during the early Holocene, which was likely triggered by a major Antarctic freshwater discharge, the associated recovery of AMOC, and a sharp increase in atmospheric CO_2. After this event, a gradual warming is observed in the SMT16 paleotemperature record until the mid-Holocene, in agreement with increasing insolation and CO2 concentrations. In general, our new record in comparison with other paleotemperature records from the region evidence the tight coupling between high-latitude forcing and tropical South American climate, highlighting the sensitivity of continental temperatures in central-eastern Brazil to abrupt ocean–atmosphere reorganizations.

5.8 References

Alvares, C.A., Stape, J.L., Sentelhas, P.C., De Moraes Gonçalves, J.L., 2013. Modeling monthly mean air temperature for Brazil. Theor Appl Climatol 113, 407–427. https://doi.org/10.1007/s00704-012-0796-6

Ampuero, A., Stríkis, N.M., Apaéstegui, J., Vuille, M., Novello, V.F., Espinoza, J.C., Cruz, F.W., Vonhof, H., Mayta, V.C., Martins, V.T.S., Cordeiro, R.C., Azevedo, V., Sifeddine, A., 2020. The Forest Effects on the Isotopic Composition of Rainfall in the Northwestern Amazon Basin. Journal of Geophysical Research: Atmospheres 125. https://doi.org/10.1029/2019JD031445

Auderset, A., Schmitt, M., Martínez-García, A., 2020. Simultaneous extraction and chromatographic separation of n-alkanes and alkenones from glycerol dialkyl glycerol tetraethers via selective Accelerated Solvent Extraction. Organic Geochemistry 143, 103979. https://doi.org/10.1016/j.orggeochem.2020.103979

Auler, A., Farrant, A.R., 1996. A brief introduction to karst and caves in Brazil. Proc. Univ. Bristol Splaeol.Soc. 20, 187–200.

Bahr, A., Hoffmann, J., Schönfeld, J., Schmidt, M.W., Nürnberg, D., Batenburg, S.J., Voigt, S., 2018. Low-latitude expressions of high-latitude forcing during Heinrich Stadial 1 and the Younger Dryas in northern South America. Global and Planetary Change 160, 1–9. https://doi.org/10.1016/j.gloplacha.2017.11.008

Baker, A., Blyth, A.J., Jex, C.N., Mcdonald, J.A., Woltering, M., Khan, S.J., 2019. Glycerol dialkyl glycerol tetraethers (GDGT) distributions from soil to cave: Refining the speleothem paleothermometer. Organic Geochemistry 136. https://doi.org/10.1016/j.orggeochem.2019.06.011

Bao, Y., Liu, Z., He, C., 2023a. Dipole Response of Millennial Variability in Tropical South American Precipitation and d18Op during the Last Deglaciation. Part II: d18Op Response. Journal of Climate 36, 4709–4721. https://doi.org/10.1175/JCLI-D-22-0289.1

Bao, Y., Liu, Z., He, C., 2023b. Dipole Response of Millennial Variability in Tropical South American Precipitation and δ18Op during the Last Deglaciation. Part I: Rainfall Response. Journal of Climate 36, 4691–4707. https://doi.org/10.1175/JCLI-D-22-0172.1

Berger, A., Loutre, M.F., 1991. Insolation values for the climate of the last 10 million years. Quaternary Science Reviews 10, 297–317. https://doi.org/10.1016/0277-3791(91)90033-Q

Bernal, J.P., Cruz, F.W., Stríkis, N.M., Wang, X., Deininger, M., Catunda, M.C.A., Ortega-Obregón, C., Cheng, H., Edwards, R.L., Auler, A.S., 2016. High-resolution Holocene South American monsoon history recorded by a speleothem from Botuverá Cave, Brazil. Earth and Planetary Science Letters 450, 186–196. https://doi.org/10.1016/j.epsl.2016.06.008

Blyth, A.J., Schouten, S., 2013. Calibrating the glycerol dialkyl glycerol tetraether temperature signal in speleothems. Geochimica et Cosmochimica Acta 109, 312–328. https://doi.org/10.1016/j.gca.2013.02.009

Cabrera, M., Pezzi, L., Santini, M., Mendes, C., 2025. Quantifying the Influence of Sea Surface Temperature Anomalies on the Atmosphere and Precipitation in the Southwestern Atlantic Ocean and Southeastern South America. Atmosphere 16. https://doi.org/10.3390/atmos16070887

Chaves, R.R., Nobre, P., 2004. Interactions between sea surface temperature over the South Atlantic Ocean and the South Atlantic Convergence Zone. Geophysical Research Letters 31, 2003GL018647. https://doi.org/10.1029/2003GL018647

Cheng, H., Lawrence Edwards, R., Shen, C.C., Polyak, V.J., Asmerom, Y., Woodhead, J., Hellstrom, J., Wang, Y., Kong, X., Spötl, C., Wang, X., Calvin Alexander, E., 2013. Improvements in 230Th dating, 230Th and 234U half-life values, and U-Th isotopic measurements by multi-collector inductively coupled plasma mass spectrometry. Earth and Planetary Science Letters. https://doi.org/10.1016/j.epsl.2013.04.006

Clark, P.U., Marshall, S.J., Clarke, G.K.C., Hostetler, S.W., Licciardi, J.M., Teller, J.T., 2001. Freshwater Forcing of Abrupt Climate Change During the Last Glaciation. Science 293, 283–287. https://doi.org/10.1126/science.1062517

Dardenne, M.A., 1978. Síntese sobre a estratigrafia do Grupo Bambuí no Brasil Central. Anais do XXX Congr. Bras. de Geol. Recife, 597–610.

Gentine, P., Massmann, A., Lintner, B.R., Hamed Alemohammad, S., Fu, R., Green, J.K., Kennedy, D., Vilà-Guerau De Arellano, J., 2019. Land-atmosphere interactions in the tropics - A review. Hydrology and Earth System Sciences 23, 4171–4197. https://doi.org/10.5194/hess-23-4171-2019

Golledge, N.R., Menviel, L., Carter, L., Fogwill, C.J., England, M.H., Cortese, G., Levy, R.H., 2014. Antarctic contribution to meltwater pulse 1A from reduced Southern Ocean overturning. Nat Commun 5, 5107. https://doi.org/10.1038/ncomms6107

Governo do Estado de Goiás, Secretaria de Meio Ambiente e Desenvolvimento Sustentável, STCP Engenharia de Projetos Ltda, 2016. Guia rápido de aplicação: Plano de Manejo Espeleológico — Parque Estadual de Terra Ronca. Retrieved from https://goias.gov.br/meioambiente/wp-content/uploads/sites/33/2016/06/PME_PETER_Guia_Final_revisao-e98.pdf (accessed 22 September 2025).

Haug, G.H., Hughen, K.A., Sigman, D.M., Peterson, L.C., Röhl, U., 2001. Southward migration of the intertropical convergence zone through the holocene. Science 293, 1304–1308. https://doi.org/10.1126/science.1059725

Hopmans, E.C., Schouten, S., Sinninghe Damsté, J.S., 2016. The effect of improved chromatography on GDGT-based palaeoproxies. Organic Geochemistry 93, 1–6. https://doi.org/10.1016/j.orggeochem.2015.12.006

Köhler, P., Nehrbass-Ahles, C., Schmitt, J., Stocker, T.F., Fischer, H., 2017. A 156 kyr smoothed history of the atmospheric greenhouse gases CO_2, CH_4, and N_2O and their radiative forcing. Earth System Science Data 9, 363–387. https://doi.org/10.5194/essd-9-363-2017

Lemieux-Dudon, B., Blayo, E., Petit, J.R., Waelbroeck, C., Svensson, A., Ritz, C., Barnola, J.M., Narcisi, B.M., Parrenin, F., 2010. Consistent dating for Antarctic and Greenland ice cores. Quaternary Science Reviews 29, 8–20. https://doi.org/10.1016/j.quascirev.2009.11.010

Liu, Z., Otto-Bliesner, B.L., He, F., Brady, E.C., Tomas, R., Clark, P.U., Carlson, A.E., Lynch-Stieglitz, J., Curry, W., Brook, E., Erickson, D., Jacob, R., Kutzbach, J., Cheng, J., 2009. Transient Simulation of Last Deglaciation with a New Mechanism for Bølling-Allerød Warming. Science 325, 310–314. https://doi.org/10.1126/science.1171041

Marson, J.M., Wainer, I., Mata, M.M., Liu, Z., 2014. The impacts of deglacial meltwater forcing on the South Atlantic Ocean deep circulation since the Last Glacial Maximum. Climate of the Past 10, 1723–1734. https://doi.org/10.5194/cp-10-1723-2014

Mcmanus, J.F., Francois, R., Gherardi, J.-M., Keigwin, L.D., Brown-Leger, & S., 2004. Collapse and rapid resumption of Atlantic meridional circulation linked to deglacial climate changes.

Meier, K.J.F., Jaeschke, A., Rethemeyer, J., Chiessi, C.M., Albuquerque, A.L.S., Wall, V., Friedrich, O., Bahr, A., 2022. Coupled Oceanic and Atmospheric Controls of Deglacial Southeastern South America Precipitation and Western South Atlantic Productivity. Front. Mar. Sci. 9, 878116. https://doi.org/10.3389/fmars.2022.878116

North Greenland Ice Core Project members, 2004. High-resolution record of Northern Hemisphere climate extending into the last interglacial period. Nature 431, 147–151. https://doi.org/10.1038/nature02805

Palacios, D., Stokes, C.R., Phillips, F.M., Clague, J.J., Alcalá-Reygosa, J., Andrés, N., Angel, I., Blard, P.H., Briner, J.P., Hall, B.L., Dahms, D., Hein, A.S., Jomelli, V., Mark, B.G., Martini, M.A., Moreno, P., Riedel, J., Sagredo, E., Stansell, N.D., Vázquez-Selem, L., Vuille, M., Ward, D.J., 2020. The deglaciation of the Americas during the Last Glacial Termination. Earth-Science Reviews 203. https://doi.org/10.1016/j.earscirev.2020.103113

Rasmussen, S.O., Bigler, M., Blockley, S.P., Blunier, T., Buchardt, S.L., Clausen, H.B., Cvijanovic, I., Dahl-Jensen, D., Johnsen, S.J., Fischer, H., Gkinis, V., Guillevic, M., Hoek, W.Z., Lowe, J.J., Pedro, J.B., Popp, T., Seierstad, I.K., Steffensen, J.P., Svensson, A.M., Vallelonga, P., Vinther, B.M., Walker, M.J.C., Wheatley, J.J., Winstrup, M., 2014. A stratigraphic framework for abrupt climatic changes during the Last Glacial period based on three synchronized Greenland ice-core records: refining and extending the INTIMATE event stratigraphy. Quaternary Science Reviews 106, 14–28. https://doi.org/10.1016/j.quascirev.2014.09.007

Reboita, M.S., Willian de Souza Ferreira, G., Gabriel Martins Ribeiro, J., Ali, S., 2024. Assessment of precipitation and near-surface temperature simulation by CMIP6 models in South America. Environ. Res.: Climate 3, 025011. https://doi.org/10.1088/2752-5295/ad3fdb

Santos, T.P., Shimizu, M.H., Nascimento, R.A., Venancio, I.M., Campos, M.C., Portilho-Ramos, R.C., Ballalai, J.M., Lessa, D.O., Crivellari, S., Nagai, R.H., Chiessi, C.M., Kuhnert, H., Bahr, A., Albuquerque, A.L.S., 2022. A data-model perspective on the Brazilian margin surface warming from the Last Glacial Maximum to the Holocene. Quaternary Science Reviews 286, 107557. https://doi.org/10.1016/j.quascirev.2022.107557

Scholz, D., Hoffmann, D.L., 2011. StalAge - An algorithm designed for construction of speleothem age models. Quaternary Geochronology 6, 369–382. https://doi.org/10.1016/j.quageo.2011.02.002

Schouten, S., Hopmans, E.C., Schefuß, E., Sinninghe Damsté, J.S., 2002. Distributional variations in marine crenarchaeotal membrane lipids: a new tool for reconstructing ancient sea water temperatures? Earth and Planetary Science Letters 204, 265–274. https://doi.org/10.1016/S0012-821X(02)00979-2

Shakun, J.D., Clark, P.U., He, F., Marcott, S.A., Mix, A.C., Liu, Z., Otto-Bliesner, B., Schmittner, A., Bard, E., 2012. Global warming preceded by increasing carbon dioxide concentrations during the last deglaciation. Nature 484, 49–54. https://doi.org/10.1038/nature10915

Stríkis, N.M., Buarque, P.F.S.M., Cruz, F.W., Bernal, J.P., Vuille, M., Tejedor, E., Santos, M.S., Shimizu, M.H., Ampuero, A., Du, W., Sampaio, G., Sales, H. dos R., Campos, J.L., Kayano, M.T., Apaèstegui, J., Fu, R.R., Cheng, H., Edwards, R.L., Mayta, V.C., Francischini, D. da S., Arruda, M.A.Z., Novello, V.F., 2024. Modern anthropogenic drought in Central Brazil unprecedented during last 700 years. Nature Communications 15. https://doi.org/10.1038/s41467-024-45469-8

Stríkis, N.M., Chiessi, C.M., Cruz, F.W., Vuille, M., Cheng, H., De Souza Barreto, E.A., Mollenhauer, G., Kasten, S., Karmann, I., Edwards, R.L., Bernal, J.P., Sales, H.D.R., 2015a. Timing and structure of Mega-SACZ events during Heinrich Stadial 1. Geophysical Research Letters 42, 5477. https://doi.org/10.1002/2015GL064048

Stríkis, N.M., Chiessi, C.M., Cruz, F.W., Vuille, M., Cheng, H., De Souza Barreto, E.A., Mollenhauer, G., Kasten, S., Karmann, I., Edwards, R.L., Bernal, J.P., Sales, H.D.R., 2015b. Timing and structure of Mega-SACZ events during Heinrich Stadial 1. Geophysical Research Letters 42, 5477–5484. https://doi.org/10.1002/2015GL064048

Strikis, N.M., Cruz, F.W., Cheng, H., Karmann, I., Edwards, R.L., Vuille, M., Wang, X., De Paula, M.S., Novello, V.F., Auler, A.S., 2011. Abrupt variations in South American monsoon rainfall during the Holocene based on a speleothem record from central-eastern Brazil. Geology 39, 1075–1078. https://doi.org/10.1130/G32098.1

Stute, M., Forster, M., Frischkorn, H., Serejo, A., Clark, J.F., Schlosser, P., Broecker, W.S., Bonani, G., 1995. Cooling of Tropical Brazil (5°C) During the Last Glacial Maximum. Science 269, 379–383. https://doi.org/10.1126/science.269.5222.379

Swingedouw, D., Fichefet, T., Goosse, H., Loutre, M.F., 2009. Impact of transient freshwater releases in the Southern Ocean on the AMOC and climate. Climate Dynamics 33, 365–381. https://doi.org/10.1007/s00382-008-0496-1

Venancio, I.M., Shimizu, M.H., Santos, T.P., Lessa, D.O., Dias, B.B., Chiessi, C.M., Mulitza, S., Kuhnert, H., Tiedemann, R., Vahlenkamp, M., Bickert, T., Belem, A.L., Sampaio, G., Albuquerque, A.L.S., Nobre, C., 2020a. Ocean-atmosphere interactions over the western South Atlantic during Heinrich stadials. Global and Planetary Change 195, 103352. https://doi.org/10.1016/j.gloplacha.2020.103352

Venancio, I.M., Shimizu, M.H., Santos, T.P., Lessa, D.O., Portilho-Ramos, R.C., Chiessi, C.M., Crivellari, S., Mulitza, S., Kuhnert, H., Tiedemann, R., Vahlenkamp, M., Bickert, T., Sampaio, G., Albuquerque, A.L.S., Veiga, S., Nobre, P., Nobre, C., 2020b. Changes in surface hydrography at the western tropical Atlantic during the Younger Dryas. Global and Planetary Change 184, 103047. https://doi.org/10.1016/j.gloplacha.2019.103047

Vuille, M., Burns, S.J., Taylor, B.L., Cruz, F.W., Bird, B.W., Abbott, M.B., Kanner, L.C., Cheng, H., Novello, V.F., 2012. A review of the South American monsoon history as recorded in stable isotopic proxies over the past two millennia. Climate of the Past 8, 1309–1321. https://doi.org/10.5194/cp-8-1309-2012

WAIS Divide Project Members, 2013. Onset of deglacial warming in West Antarctica driven by local orbital forcing. Nature 500, 440–444. https://doi.org/10.1038/nature12376

Wang, X., Auler, A.S., Edwards, R.L., Cheng, H., Ito, E., Solheid, M., 2006. Interhemispheric anti-phasing of rainfall during the last glacial period. Quaternary Science Reviews, Critical Quaternary Stratigraphy 25, 3391–3403. https://doi.org/10.1016/j.quascirev.2006.02.009

Wong, M.L., Battisti, D.S., Liu, X., Ding, Q., Wang, X., 2023. A North–South Dipole Response of the South Atlantic Convergence Zone During the Mid-Holocene. Geophysical Research Letters 50, e2023GL105130. https://doi.org/10.1029/2023GL105130

Zhao, B., Russell, J.M., Blaus, A., Nascimento, M.D.N., Freeman, A., Bush, M.B., 2024. Tropical Andean climate variations since the last deglaciation. Proc. Natl. Acad. Sci. U.S.A. 121, e2320143121. https://doi.org/10.1073/pnas.2320143121

Zilli, M.T., Carvalho, L.M.V., Lintner, B.R., 2019. The poleward shift of South Atlantic Convergence Zone in recent decades. Climate Dynamics 52, 2545–2563. https://doi.org/10.1007/s00382-018-4277-1

5.8 Supplementary Material III

Tropical South American temperature responses to rapid high-latitude climate shifts since the last deglaciation

5.8.1 Supplementary text 1

Each pulverized calcite sample was weighed in a 60 mL cylindrical glass vial, being subsequently dissolved in 20 mL of 6 N HCl and digested on a heating plate at 100 °C for 2 h. After cooling, the digested sample was extracted three times using 20 mL dichloromethane (DCM) in each extraction. The DCM fraction was collected in a 60 mL vial using a 50 mL separation funnel. After the third extraction, 40 µL of C46-GDGT internal standard was added to the extract for GDGT quantification purposes (Auderset *et al.*, 2020). The solvent was evaporated to complete dryness in a Genevac Rocket evaporator for ~30 minutes. To remove potential traces of acid and other impurities, the extract was re-dissolved in a mixture of DCM–methanol and passed through a 5% deactivated silica column. The eluate was collected in 4 mL vials, dried under nitrogen gas on a heating plate at 30 °C, and filtered into a 1 mL vial through a 0.2 µm polytetrafluoroethylene membrane filter using a 1.8% mixture of isopropanol in n-hexane.

5.8.2 Supplementary Figure 1

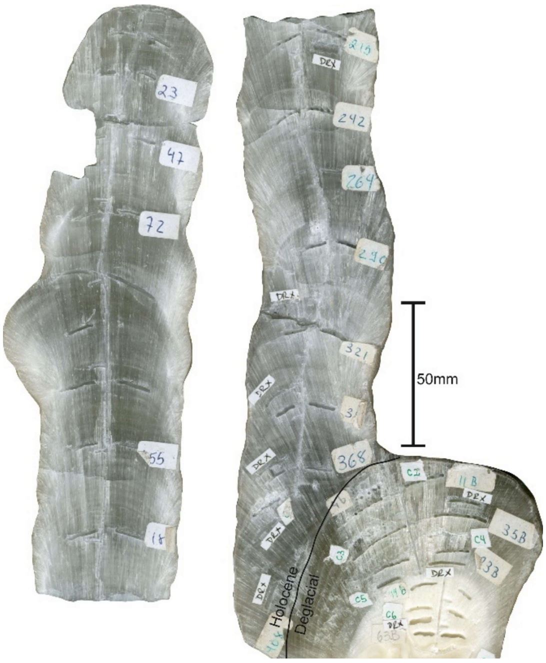

Supplementary Figure 5.1 – Scan of SMT16

Chapter 6 – Conclusions & Outlook

The main goal of this thesis is to improve our understanding on the climatic and environmental development of central-east Brazil since the deglacial period until the present. For that, a stalagmite sample from São Mateus cave located in this region was used as the subject of this study. The use of the traditional stable isotopes ($\delta^{18}O$ and $\delta^{13}C$) proxies initially used for this study soon revealed to be insufficient for a proper interpretation of the climatic and environmental conditions of this area. A linear relationship is usually observed for records within the monsoon domain in South America between $\delta^{18}O$ and $\delta^{13}C$ records, indicating that the amount of rainfall and vegetation are behaving somewhat concomitantly, since vegetation is strongly dependent on rainfall amounts in the Cerrado biome in central-east Brazil. Nonetheless, such a linear relationship was not observed for the studied stalagmite in the orbital-scale (Holocene period), presenting contradictory interpretations of between the $\delta^{18}O$ and $\delta^{13}C$ records; while the oxygen indicated progressively drier conditions to the present, the carbon indicated a development toward a wetter climate. Therefore, a more thorough investigation using a multi-proxy approach was necessary.

This region presents a complex interaction of different moisture sources that therefore hampered the classical interpretation of the $\delta^{18}O$ for regions within the South American summer monsoon as amount effect or overall monsoon strength. Moreover, the $\delta^{13}C$ is also subjected to several processes during the pathway between the soil until it is precipitated onto a stalagmite that can alter its signal, which adds a layer of complexity to the interpretations. Therefore, the application of the Sr isotope analysis was introduced as a way to gain deeper insights into the environment, cave and karst processes. The $^{87}Sr/^{86}Sr$ ratios are an independent proxy used to improve existing proxy records and exclude potential cave effects as major driver for stable isotope variations. Overall, it revealed a striking similarity with the $\delta^{13}C$ record for the Holocene period, corroborating the drier-to-wetter development initially assumed based solely on the $\delta^{13}C$ record. This coherence appears because the Sr isotope record revealed an external sandstone source of Sr isotope outside the soil-limestone system that contribute to high $^{87}Sr/^{86}Sr$ ratios during dry phases in this region.

These findings highlight the importance further developing multi-proxy approaches. Accordingly, this thesis also presents a temperatures reconstruction based on organic biomarkers

(GDGTs) analysis using the São Mateus stalagmite. This study is the first to present a temperature record of the last 15,000-year in South America based on organic biomarkers in stalagmites. The temperature changes in central-east Brazil reveal a strong modulation of the SSTs at the Brazilian margin on the continental temperatures, showing a broad coherence with both major abrupt ocean circulation changes during the deglacial period and with the long-term increase in temperatures over the Holocene. Finally, it shows how temperature has a strong coupling with changes in atmospheric circulation and local hydrology.

Overall, this study evidences the significance of expanding the range of proxies in speleothem studies to have a more complete understanding of the development of the climate and environmental systems. The use a multi-proxy approach is recommended when interpreting paleoclimate conditions in a region, whereas the use of a single proxy should be interpreted with caution. This is exemplified on the first paper, where the interpretation of single proxies results in divergent interpretations, and on the second paper where multiple proxies converge to a coherent climate scenario. Ultimately, this thesis demonstrates that only through the integration of multiple, complementary proxies we can disclose the complex interplay of processes that shape past and present climate dynamics in tropical South America.